Locality and Many-Body Quantum Spectra

Samuel Joshua Garratt

St. John's College

University of Oxford

A thesis submitted for the degree of

Doctor of Philosophy

Trinity 2021

Abstract

This thesis is concerned with many-body quantum dynamics in lattice models. Our focus is on the spectral properties of Floquet operators that describe local interactions in one dimension. Physical properties are expressed as multiple sums over paths in the many-body Fock space, and this leads naturally to interpretations in terms of interference effects, or of paired paths. By averaging properties over ensembles of random systems we wash out non-universal interference effects, and study the structures which survive.

In Chapter 2 we address the ergodic phase of quantum dynamics. In this setting random matrix theory (RMT) and the eigenstate thermalisation hypothesis (ETH) are expected to describe spectral properties. This can be understood through the diagonal approximation to sums over paired paths. We show how the diagonal approximation must be extended in systems with local interactions, and that as a result there are deviations from RMT and the ETH which, at finite times, diverge with system size. Our focus is primarily on the spectral form factor (SFF) and related quantities, and our approach is to express averaged sums over pairs of paths in terms of a transfer matrix that acts in the space direction.

In Chapter 3 we show how, within this framework, the transition from a many-body localised (MBL) phase to an ergodic one can be viewed as symmetry breaking. This transition in dynamics has sharp signatures in spectral statistics, so it is natural to consider the SFF. The transfer matrix generating the SFF has symmetries associated with translations in time: in the ergodic phase one of these symmetries is broken, whereas in the MBL phase it is not. For the Floquet models we consider the relevant symmetry group is that of a clock model. We introduce an order parameter for the broken symmetry, and show how the applicability of the diagonal approximation can be understood as a form of long-range order.

Chapters 2 and 3 are based on the respective following articles [1, 2]

S. J. Garratt and J. T. Chalker
"Local pairing of Feynman histories in many-body Floquet models"
Physical Review X, vol. 11, p. 021051, 2021.

S. J. Garratt and J. T. Chalker
"Many-body delocalization as symmetry breaking"
Physical Review Letters, vol. 127, p. 026802, 2021.

Acknowledgements

Naught would have materialised were it not for the patience and creativity of my advisor, John Chalker. Our work on these problems has proved to be much more entertaining than I could have expected; the word 'grateful' is an understatement.

The picture we set out to develop followed a few surprises. One quantity was larger than another, and a few curves collapsed. Those initial calculations were carried out a few months before the end of the world, after a summer in Les Houches. Thanks are owed to Max McGinley, Aaron Friedman, Vir Bulchandani, and the two from Toulouse, for time in the clouds and lessons in getting out of them.

These lessons could admittedly have been learnt from Glenn Wagner and Aleksandra Ziolkowska, who I have had the pleasure of sharing an office with, or from Saeed Mahdisoltani and Tunrayo Adeleke-Larodo, who have endured almost as much. In Oxford I am grateful also to Sthitadhi Roy, for the animated calls, to Adam Nahum, Sid Parameswaran, and the rest of the faculty, for guidance and for intimidation, and to the many others who made the department such a vibrant place. From Cambridge I thank Chris Haniff, for encouragement and sober words against scientific realism, Christoph Eigen, Nir Navon, and Zoran Hadzibabic, whose enthusiasm drew me in, and Austen Lamacraft, who saved their machine.

I also acknowledge support from the taxpayer. Without the EPSRC none of this would have been possible. It would have been much harder without Hydra, and much less eventful without the financial support of my college.

Along the way there have been those who provided refuge from my hard-boiled wonderland [3]. For this I thank Sophia Buck, Thomas Carswell, Alice Alcaras, Zack Grant, Rachel Coombes, and Eilidh Guthrie. Thanks are also owed to the long-suffering and the very-long-suffering, who know who they are.

This thesis is dedicated to my family. I would not be hunched over the present computer if not for their support. How many miles to London? And kilometres? And how long will it take to get there?

Contents

List of Abbreviations

CUE . . . . . Circular unitary ensemble

COE . . . . . Circular orthogonal ensemble

ED . . . . . Exact diagonalisation

ETH . . . . . Eigenstate thermalisation hypothesis

GUE . . . . . Gaussian unitary ensemble

GOE . . . . . Gaussian orthogonal ensemble

LIOM . . . . . Local integrals of motion

MBL . . . . . Many-body localised

RFF . . . . . Reduced form factor

RMT . . . . . Random matrix theory

RFC . . . . . Random Floquet circuit

RPM . . . . . Random phase model

RUC . . . . . Random unitary circuit

SFF . . . . . Spectral form factor

TRS . . . . . Time-reversal symmetry

1 Introduction

The behaviour of quantum matter at high energies is familiar. A drop of ink in a glass of water will diffuse. Because our glass and its contents are quantum-mechanical, if we isolate it from the environment any dynamics must be described by a unitary operator [4]. However, no information is lost under unitary dynamics. Faced with the phenomenon of diffusion, we must ask: where did the information go?

Similar questions arise in a classical setting [5]. Modelling our ink and water molecules using Newton's laws, and armed with exact information on the initial state of the system, we can trace out the path of the system in phase space. Or, given exact information on the state at a later time, we can work backward and recover the ink drop. But, computational resources aside, the classical dynamics of the molecules is chaotic. A small degree of uncertainty in the initial state of the system is enough for the different possible phase-space paths to diverge from one another [6]. Although diffusion is reversible in principle, it is not in practice.

The language used to describe the emergence of irreversibility in quantum mechanics is quite different [7–11]. This is necessary because the uncertainty principle forbids the identification of a system's time evolution with a phase-space path. Modern discussions of equilibration in quantum many-body systems are often based instead on the idea of operator spreading [12, 13]. Although the many-body wavefunction provides complete information on a system, our measuring devices

only probe observables that are local. Under unitary dynamics, the corresponding Heisenberg operators spread into non-local objects, so the information is no longer accessible: it is 'scrambled' [14–16]. This is a mechanism by which quite different initial states can approach essentially the same local equilibrium.

From another perspective, for the resulting equilibrium state to appear thermal to a local probe, the reduced density matrices of subregions must become thermal. The total entanglement entropy of a subsystem then scales as its volume. This is the so-called 'volume law', a feature shared with unstructured random states [17]. Then, preparing a system in a weakly-entangled state, its approach to thermal equilibrium is associated with the growth of entanglement between subsystems and their surroundings [18–20]. This behaviour, and the scrambling of local information, are signatures of many-body quantum chaos. The corresponding physical systems make up the ergodic phase [10]. As in the classical case, chaos is typical when there are more than a few particles.

Non-ergodic behaviour is expected in a many-body system if its dynamics is integrable [9, 10]. That is, if it has an extensive number of conservation laws. These represent a strong constraint on the dynamics, and prevent equilibration to an ordinary thermal ensemble [see for example Ref. [21]]. Moreover, there is now compelling evidence that a stable kind of integrability can emerge in the presence of sufficiently strong disorder [22–28]. The resulting many-body localised (MBL) phase is characterised by an extensive number of locally conserved quantities, or local integrals of motion (LIOM) [29–32]. These LIOM have signatures at all energies in the spectrum. For example, the eigenstates in the MBL phase have area-law entanglement [26, 33]. Whereas eigenstates in chaotic systems resemble unstructured random vectors, those in the MBL phase resemble matrix product states [33].

Many-body quantum chaos and many-body localisation are the two dynamical regimes with which this thesis is concerned. Neither requires additional symmetries or conservation laws, although their inclusion may make the dynamics far richer. A simplification available to us is to consider models for unitary time evolution, as opposed to model Hamiltonians [12, 13, 20]. To study the scrambling of local

information, while preserving notions of locality and the existence of a well-defined spectrum, one can consider periodically acting on nearby degrees of freedom with random unitary matrices [34–36]. Without a Hamiltonian there is no notion of energy conservation, nor is a there a notion of temperature. For this reason, the dynamics can be thought of as occurring at infinite temperature. It is therefore reasonable to expect that these models describe certain features of the high-energy dynamics generated by physical Hamiltonians.

This paradigm is clearly distinct from traditional descriptions of quantum matter [37]. For example, in the canonical Bose and Fermi liquids, a conspiracy of interactions and exchange statistics gives rise to a gas of quasiparticles which, at low temperatures, is dilute. Theories can then be developed in terms of these weakly-interacting degrees of freedom. Moving up through the many-body spectrum, however, the quasiparticle density increases, a perturbative treatment of their interactions becomes inappropriate, and the entire picture breaks down. We find ourselves in the high-energy regime which is of interest here, without any quasiparticle description. The theories we will develop instead have their historical roots in semiclassical and mesoscopic physics, as well as in random matrix theory (RMT).

1.1 Random matrix theory

The statistical theory of random matrices was developed largely in parallel with experimental studies of complex nuclei [38]. The first steps toward understanding properties of the highly-excited states are due to Wigner, who recognised that although global features in the spectrum depend on details of the system, such as the fact that the repulsion between protons is long-ranged, this ‘does not influence the law of the statistical distribution of level spacing and level width’ [39]. In Sec. 1.1.1 we motivate the use of random matrices as models for physical systems. In Sec. 1.1.2 we then discuss ensembles of random unitary matrices, and in this setting introduce the spectral form factor (SFF) in Sec. 1.1.3.

1.1.1 Wigner's surmise

Experimental work on the spectra of complex nuclei centred on inelastic neutron scattering. A key signature observed in these experiments was the low probability to find pairs of levels, having the same symmetries, nearby in the spectrum. This repulsion between energy levels is characteristic of random matrices, a point best illustrated by diagonalising a 2×2 random Hermitian matrix $H = (1/2)\vec{r}\cdot\vec{\sigma}$. Here $\vec{r}$ is a real three-component vector, $\vec{\sigma} = (\sigma^x, \sigma^y, \sigma^z)$ is a vector of standard Pauli matrices, and the level spacing $\omega = |\vec{r}|$. Taking the components of $\vec{r}$ to be independent unit-normally distributed random variables, one finds the probability distribution

$$p(\omega) = (2/\pi)^{1/2}\omega^2 e^{-\omega^2/2}. \tag{1.1}$$

Here the form of $p(\omega)$ at large ω is inherited from the distributions we have chosen for the matrix elements of H, but the quadratic level repulsion $p(\omega) \sim \omega^2$ at small ω is generic. This property depends on the symmetry class of the system. An ensemble of H with time-reversal symmetry (TRS) is realised by setting $r_y = 0$ so that H is real, and in that case we find $p(\omega) \sim \omega$, i.e. linear level repulsion.

The Hamiltonian of a complex nucleus is obviously of dimension greater than two. However, as noted above, certain local features in the spectra of random matrices are independent of global ones. The power governing level repulsion is such a (local) feature, and provides our first example of random-matrix universality. Motivated by the apparent decoupling of (universal) local statistics and (non-universal) global ones, the pioneers of RMT resolved to treat the nucleus as a black box, modelling its Hamiltonian as a random matrix [38].

In choosing a random matrix ensemble to describe a complex physical system, it is clear that care is required when it comes to the symmetry class. For an isolated nucleus the energy scale associated with the breaking of TRS[1] is much smaller than the mean level spacing. Experimentally, one finds that the spectral statistics match the those of the Gaussian orthogonal ensemble (GOE) [40]. This is the ensemble of real Hermitian matrices with independent Gaussian-random entries

[1] In this setting TRS is broken by the weak interaction.

whose statistical properties are invariant under orthogonal transforms. On the other hand, if anti-unitary symmetries such as time reversal are broken, we must allow for complex entries [41]. Provided the breaking of these symmetries is strong enough, we expect spectral statistics to match those of the Gaussian unitary ensemble (GUE), named for its invariance under unitary transforms. For nuclei, and even atoms, such an orthogonal-unitary crossover has not been reported[2]. Experimental observations of level statistics characteristic of the GUE, in a quantum-mechanical setting, followed relatively recently [42, 43]. For example, Ref. [43] investigated the spectra of excitons in a lattice system. There, the combined effect of an external magnetic field and exciton-phonon coupling breaks all anti-unitary symmetries.

1.1.2 Random unitary matrices

Because local and global features in the spectra of large random matrices are essentially decoupled, it is convenient to study ensembles whose average level density is uniform. This leads us to the study of random unitary matrices, and so to Dyson's circular ensembles [44]. While matrices drawn from the Gaussian ensembles may serve as proxies for Hamiltonians, those drawn from the circular ensembles serve as proxies for unitary evolution operators. The statistical properties of the circular orthogonal ensemble (COE) and circular unitary ensemble (CUE), in analogy with the GOE and GUE, are respectively invariant under orthogonal and unitary transforms. For a unitary matrix W, we write the eigenvalues as $e^{i\theta_n}$ and the corresponding eigenstates as $|n\rangle$. We will often refer to θ_n as quasienergies.

In the interest of simplicity, in this work our focus is on systems without TRS. Frequent comparisons will therefore be made with the CUE, which coincides with the invariant Haar distribution over the unitary group, so we will refer to matrices drawn from it as Haar-random. The defining property of this distribution is invariance under left- and right-multiplication, as we discuss in A.1.1.

[2] A homogeneous magnetic field breaks conventional TRS, but another anti-unitary symmetry survives due to reflection symmetry. Introducing an electric field along another axis restricts the symmetry plane to be that defined by the electric and magnetic fields, and an anti-unitary symmetry survives [41].

For orientation, consider first the case of 2×2 unitary matrices. The Haar distribution then has the following properties. First, note that any 2×2 unitary can be parametrised by $W = e^{i\varphi} e^{i\omega \vec{n}\cdot\vec{\sigma}/2}$, where $\vec{n}$ is a unit vector, $\omega = |\theta_1 - \theta_2|$ is the separation between the quasienergies of W, with $0 \leq \omega \leq \pi$, and φ is a phase. For Haar-random W, φ is uniformly distributed on the unit circle, $\vec{n}$ on the unit sphere, and the probability distribution $p(\omega) = (2/\pi)\sin^2(\omega/2)$. Note that $p(\omega) \sim \omega^2$ for small ω, as in Eq. (1.1). More generally, the eigenvectors of $N \times N$ Haar-random matrices are isotropically distributed and mutually orthogonal complex vectors. The joint-probability distribution of the quasienergies, on the other hand, has a great deal of structure. We calculate it in in A.1.2.

Given the Haar distribution over the group of $N \times N$ unitary matrices, we can compute its moments [45, 46]. For example, the first moment $\langle W_{ab} \rangle = 0$, and the only nonzero second moment is $\langle W_{ab} W^*_{a^* b^*} \rangle = (1/N)\delta_{aa^*}\delta_{bb^*}$; in fact, only the even moments involving the same number of copies of W and W^* are nonzero. For the nonzero $(2M)^{\text{th}}$ moment we have the sum over index contractions

$$\begin{aligned} &\left\langle W_{a_0 b_0} \dots W_{a_{M-1} b_{M-1}} W^*_{a_0^* b_0^*} \dots W^*_{a_{M-1}^* b_{M-1}^*} \right\rangle \\ &\qquad = \sum_{\sigma\tau} \mathrm{Wg}(\sigma\tau^{-1}) \prod_{r=0}^{M-1} \delta_{a_r a^*_{\sigma(r)}} \delta_{b_r b^*_{\tau(r)}}. \end{aligned} \tag{1.2}$$

Here a_r, b_r are indices of the M copies of W, and a_r^*, b_r^* those of the M copies of W^*, with $a_r, b_r, a_r^*, b_r^* = 0 \dots (N-1)$. The sum in Eq. (1.3) is over elements σ, τ of the permutation group on M elements, and $\mathrm{Wg}(\sigma\tau^{-1})$ are values of Weingarten functions Wg, which depend on N, M, and the conjugacy class of $\sigma\tau^{-1}$. For example, for $M = 1$ the only possibility is $\sigma = \tau = \mathbb{1}$, the identity permutation, and $\mathrm{Wg}(\mathbb{1}) = 1/N$. In A.1.4 we present a self-contained derivation of the Weingarten functions for $M = 2$, following Ref. [12].

1.1.3 Spectral form factor

A sensitive probe of the spectral statistics is the spectral form factor (SFF), which is the central quantity considered in this work. For a unitary matrix W we write

$W(t) \equiv W^t$ for integer t, and define the SFF as

$$K(t) \equiv |\mathrm{Tr}W(t)|^2 = \sum_{nm} e^{i(\theta_n - \theta_m)t}. \tag{1.3}$$

The SFF is the Fourier transform of the two-point correlator of the level density. It has an interesting interpretation in terms of paired paths, which we discuss below. The average SFF for Haar-random W has the characteristic form [41]

$$\langle K(t)\rangle = \begin{cases} N^2, & t = 0 \\ t, & 1 \leq t \leq N \\ N, & N \leq t \end{cases}, \tag{1.4}$$

as we show in A.1.3. In this setting the Heisenberg time t_{H}, defined from the mean level-spacing $2\pi/N$, is $t_{\mathrm{H}} = N$. The behaviour in Eq. (1.4) is often referred to as the ramp ($1 \leq t \leq N$) and plateau ($t \geq N$).

The plateau in Eq. (1.4) can be understood as follows. The mean spacing of the quasienergies of W around the unit circle is $2\pi/N$, and for $t \geq N$ the quantity $\mathrm{Tr}W(t) = \sum_n e^{i\theta_n t}$ behaves as a random walk of N steps of unit length in the complex plane. The result $\langle K(t)\rangle = N$ follows immediately. The ramp, on the other hand, reflects the rigidity of the spectrum on quasienergy scales above the mean level spacing, and this rigidity is a consequence of level repulsion. For comparison with Eq. (1.4) the average SFF for the COE, describing systems with TRS, has a concise form for $N \gg 1$. One finds $\langle K(t)\rangle = 2t - t\ln(1 + 2t/N)$ for $1 \leq t \leq N$, and $\langle K(t)\rangle = 2N - t\ln[(2t + N)/(2t - N)]$ for $t \geq N$ [41].

The result $\langle K(t)\rangle = t$ for $1 \leq t \leq N$ in Eq. (1.4) can be obtained straightforwardly from Eq. (1.3) in the limit $t \ll N$. For Haar-random W all corrections to the leading-order result cancel for $t < N$, but the details of this cancellation are not of concern here. It is useful to write

$$\mathrm{Tr}W(t) = \sum_{a_0 \ldots a_{t-1}} W_{a_0 a_{t-1}} \ldots W_{a_1 a_0} \tag{1.5}$$

which is a sum over all closed paths of t steps. We refer to these paths as orbits. The amplitude of each orbit is a product of t matrix elements of W. The SFF is then

a sum over all pairs of forward and backward orbits, appearing respectively in $\mathrm{Tr}W(t)$ and $\mathrm{Tr}W^*(t)$,

$$K(t) = \sum_{a_0 \dots a_{t-1}} W_{a_0 a_{t-1}} \dots W_{a_1 a_0} \times \sum_{a_0^* \dots a_{t-1}^*} W^*_{a_0^* a_{t-1}^*} \dots W^*_{a_1^* a_0^*}. \tag{1.6}$$

We now outline the process of averaging Eq. (1.6) over W in the limit of large N, using Eq. (1.3) for $M = t$. First, the Weingarten function $\mathrm{Wg}(\sigma\tau^{-1})$ is maximised for $\sigma = \tau$, taking the value $\mathrm{Wg}(\mathbb{1}) = 1/N^t$ up to subleading corrections [46]. It is then straightforward to show that the cyclic permutations $\sigma : r \to r + s$, where r and s are integers $0 \dots (t-1)$ defined modulo t, are dominant. We then find

$$\langle K(t) \rangle = \sum_{\substack{a_0 \dots a_{t-1} \\ a_0^* \dots a_{t-1}^*}} \frac{1}{N^t} \sum_{s=0}^{t-1} \prod_{r=0}^{t-1} \delta_{a_r a^*_{r+s}} = t, \tag{1.7}$$

and the second equality follows for nonzero integer[3] $t \ll N$. The sum over $s = 0 \dots (t-1)$ can be interpreted as follows. $K(t)$ is a sum over N^{2t} pairs of orbits, and those with $a_r = a^*_{r+s}$ give real non-negative contributions to Eq. (1.6). We refer to these as diagonal orbit pairs. The freedom in s comes from the fact that the complex amplitude of an orbit does not depend on where it starts, from the cyclic property of the trace $\mathrm{Tr}W^t$. We refer to this as a freedom in the orbit pairing.

1.2 Few degrees of freedom

The black-box perspective on a nuclear Hamiltonian does not tell us anything about the nature of the dynamics associated with RMT spectral statistics. This is unsurprising, as the dynamics is in that case extremely complicated. A controlled setting to look for a connection between spectra and dynamics is, instead, in systems with few degrees of freedom. In Sec. 1.2.1 we discuss the semiclassical limit, and following this in Sec. 1.2.2 we give an overview of relevant topics in the theory of mesoscopics.

[3]For $t \ll N$ typical forward orbits have $a_r \neq a_{r'}$ for $r \neq r'$, so the t backward orbits with $a^*_{r+s} = a_r$ are distinct. By contrast, for a forward orbit with $a_r = a_{r'}$ for all r, r', there is just one backward orbit with $a^*_{r+s} = a_r$.

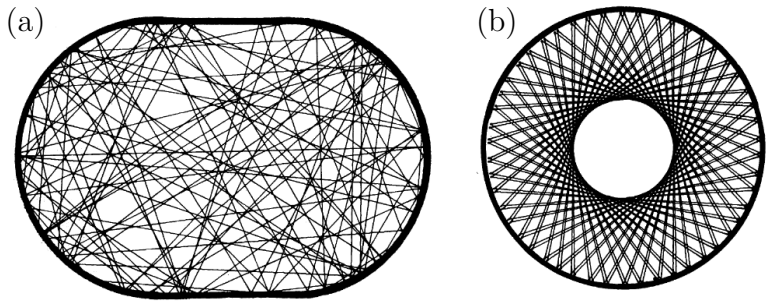

Figure 1.1: Classical paths of particles confined to finite regions of two-dimensional space, from Ref. [47]. (a) Chaotic dynamics in the Bunimovich stadium, and (b) integrable dynamics in a circle.

1.2.1 Semiclassics

In the semiclassical limit $\hbar \to 0$ the physics of a quantum system is controlled by the classically-allowed paths. This follows from stationary-phase evaluation of path integrals. Sec. 1.2.1.1 describes the different kinds of classical dynamics, and indicates the relation to quantum-mechanical spectra. In Sec. 1.2.1.2 we discuss the connection in more detail, making reference to Gutzwiller's periodic orbit theory [6].

1.2.1.1 Chaos and integrability

Classical dynamics may be either integrable or chaotic [6]. In the integrable case there are as many conservation laws as there are conjugate pairs of degrees of freedom, so the dynamics is highly constrained. With more than a few degrees of freedom, such systems are rare. In the chaotic case the dynamics is not so constrained, and two systems with similar initial states will typically find their phase-space paths diverge.

As a concrete example, consider a single particle confined to a finite region of two-dimensional space. For each of the two position coordinates there is an associated momentum, so we have just two conjugate pairs of degrees of freedom. If there is a conservation law in addition to the energy, for example angular momentum as occurs for a confining region with rotational symmetry, the motion is integrable. Without this additional symmetry, the motion is chaotic. Real-space paths of particles in these two classes of systems are illustrated in Fig. 1.1.

As noted above, in chaotic classical systems nearby points in phase space sit on diverging paths. This property points to arbitrarily fine structures in phase

space. Such structures cannot carry over to quantum-mechanical wavefunctions, as they would be associated with divergent kinetic energies through the uncertainty principle. Because the concept of a point or path in phase space does not survive with nonzero $\hbar$, notions of chaos in classical and in quantum mechanics must be quite different. Interestingly, one finds that the spectrum of a quantum system is sensitive to the nature of the dynamics of its classical analogue [48–50].

This was first discussed by Berry and Tabor in the integrable case [48]. The spectral statistics of a system of decoupled harmonic oscillators, having incommensurate frequencies, were shown to have levels distributed according to a Poisson process, i.e. as uncorrelated random numbers, on fine scales. Based on this, they conjectured that Poisson statistics are a universal feature of systems whose classical analogues are integrable. The chaotic partner of the Berry-Tabor conjecture was later formulated by Bohigas, Giannoni and Schmit (BGS) [50] [see also Ref. [49]]. A detailed numerical investigation of the spectrum of a single particle confined to a two-dimensional region, without rotational symmetry, revealed statistical properties which at high energies matched the GOE. This result is striking for a number of reasons. First, their model contained no randomness. Second, it implied that systems so distinct as chaotic billiards and complex nuclei should have essentially the same level statistics. The BGS conjecture was that, with TRS, GOE (or COE) level statistics are universal in quantum systems whose classical analogues are chaotic. Berry and Robnik [51, 52] soon considered the spectrum of a billiards setup in the presence of an Aharonov-Bohm flux, thereby breaking TRS, and found excellent agreement with the statistical properties of the GUE (or CUE).

From this we arrive at the spectral definition of quantum chaos, which is now routinely applied even in the absence of the semiclassical limit where it was first understood. Quantum chaotic systems have level statistics which, locally, coincide with those of random matrices. We now turn to an explanation for this phenomenon in the semiclassical limit.

1.2.1.2 Diagonal approximation

An explicit connection between the spectrum of a quantum system in its semiclassical limit, and the dynamics of its classical analogue, comes through Gutzwiller's periodic orbit theory [6]. This provides a relation between the level density and sums over classical phase-space orbits, and so between spectral correlations and sums over pairs of such orbits. If the classical dynamics is chaotic, the diagonal approximation to this sum reveals RMT spectral statistics [53].

We focus here on a Hamiltonian H with energy levels E_n. The density of states $\rho(E) = \sum_n \delta(E - E_n)$ is related to the trace over the time evolution operator $e^{-iHt/\hbar}$ by Fourier transformation. This trace can be expressed as path integral, where all paths (orbits) are closed, and evaluated in the semiclassical limit $\hbar \to 0$ by the method of stationary phase. In this way one finds an expression for the density of states in terms of closed classical orbits

$$\rho(E) = \langle \rho(E) \rangle + \frac{1}{\hbar} \sum_j a_j(E) e^{iS_j(E)/\hbar}. \tag{1.8}$$

Here $\langle \rho(E) \rangle$ is a smooth function of E, and the oscillatory term involves a sum over families j of orbits. Each family is a continuous set of orbits differing only in their start point, and so having the same action $S_j(E)$ and period $T_j(E) = \partial S_j(E)/\partial E$. To each family we associate a real weight $a_j(E)$, obtained from Gaussian integration around the classical path (we include any phase factors in $S_j(E)$). Note that a sum over j appears, as opposed to an integral, because in chaotic systems different families of orbits are isolated and unstable [6]. The sum also features negative traversals, having the same amplitudes $a_j(E)$ but opposite actions $-S_j(E)$ and periods $-T_j(E)$, so that $\rho(E)$ is real.

In this setting it is convenient to define the SFF, around a central energy E, by

$$K(E,t) = \int_\infty^\infty d\varepsilon \rho(E + \varepsilon/2)\rho(E - \varepsilon/2) e^{i\varepsilon t/\hbar}, \tag{1.9}$$

Inserting Eq. (1.8) into Eq. (1.9) and writing $S_j(E \pm \varepsilon/2) \simeq S_j(E) \pm T_j(E)\varepsilon/2$ we find, for $t > 0$,

$$K(E,t) = \frac{2\pi}{\hbar} \sum_{jk}{}' a_j(E) a_k(E) e^{i[S_j(E) - S_k(E)]/\hbar} \delta\Big(t - \frac{1}{2}[T_j + T_k]\Big), \tag{1.10}$$

where the primed sum only runs over the positive traversals[4]. Eq. (1.10) is the desired relation between the spectral statistics and pairs of closed classical orbits. In practice the integration should be limited to an energy window over which second derivatives of $S_j(E)$ can be neglected, but which contains many levels in the limit $\hbar \to 0$ [53].

How spectral statistics characteristic of RMT emerge from Eq. (1.10) was shown by Berry through the diagonal approximation [53], which involves neglecting correlations between the actions of symmetry-unrelated pairs of orbits. In this way for $\hbar \to 0$ and $t > 0$ one finds

$$K(E,t) = \frac{2\pi}{\hbar} \sum_j{}' a_j^2(E)\delta(t - T_j). \tag{1.11}$$

This is determined by the sum rule of Hannay and Ozorio De Almeida [54], which originates from the principle of ergodicity: in chaotic classical systems there is a sense in which phase-space paths cover the energy shell[5] at large t. One then finds that the sum in Eq. (1.11) is independent of system details. The result, for large $t \ll \hbar\langle\rho\rangle$, is

$$K(E,t) = \frac{t}{2\pi\hbar}, \tag{1.12}$$

in systems without TRS. This coincides with the RMT result in Eq. (1.4). As before, the factor t can be understood as coming from the freedom to pair each orbit with a conjugate which differs only in its start point. The 'number' of such conjugates is proportional to t. One also finds a plateau $K(E,t) = \langle\rho(E)\rangle$ for $t \gg \hbar\langle\rho\rangle$. This comes from a relation between the smooth and oscillatory contributions to Eq. (1.8) [53].

1.2.2 Mesoscopics

Many of the ideas from RMT and semiclassics arise also in the theory of mesoscopics [55–57]. In that setting transitions between metallic and insulating phases can be induced by disorder [58–60]. In Sec. 1.2.2.1 we show how a picture of paired paths

[4] In Eq. (1.10) we neglect contributions with phase factors $e^{i[S_j(E)+S_k(E)]/\hbar}$. These vanish in the limit $\hbar \to 0$

[5] Of course, paths are one-dimensional objects. In practice an average over a narrow window in E or t is necessary to recover a uniform density in phase space.

arises from disorder-averaged products of single-particle Green's functions; RMT behaviour appears at large times and small energy scales [61], and in Sec. 1.2.2.2 we discuss the nature of the deviations from it [62, 63]. In Sec. 1.2.2.3 we outline aspects of Anderson localisation.

1.2.2.1 Paired paths

To frame our discussion we consider the model $H = H_0 + V$, where H_0 is the Hamiltonian for electrons hopping on a lattice, and V is a disorder potential which we choose to be diagonal in the position basis $|x\rangle$,

$$H_0 = -\sum_{x,x'}{}' \Big(|x\rangle \langle x'| + |x'\rangle \langle x| \Big), \quad V = \sum_x V(x) |x\rangle \langle x| , \tag{1.13}$$

where the primed sum in H_0 is over nearby pairs of sites, and $V(x)$ are random with averages $\langle V(x)\rangle = 0$ and $\langle V(x)V(x')\rangle = v^2\delta_{xx'}$. The standard treatment of this model is in the energy domain using Green's functions $G^{\pm}(E) \equiv (E - H \pm i0)^{-1}$ [55]. For weak disorder it is useful to expand

$$G^{\pm}(E) = G_0^{\pm}(E) + G_0^{\pm}(E)VG_0^{\pm}(E) + G_0^{\pm}(E)VG_0^{\pm}(E)VG_0^{\pm}(E) + \ldots, \tag{1.14}$$

where $G_0^{\pm}(E) = (E - H_0 \pm i0)^{-1}$. In the time domain we would instead study the propagator. For $t > 0$, setting $\hbar = 1$ from here on, this is $e^{-iHt} = \int dE G^+(E) e^{-iEt}$. The term in Eq. (1.14) at n^{th} order in V corresponds to the amplitude for an electron to scatter n times from the disorder potential.

From expressions of the form Eq. (1.14) we can calculate, for example, the electron return probability. This involves a product of matrix elements of $G^+(E)$ and $G^-(E')$. The probability for the electron to return to x_0 at time t is

$$|\langle x_0|e^{-iHt}|x_0\rangle|^2 = \int dE dE' \langle x_0|G^+(E)|x_0\rangle \langle x_0|G^-(E')|x_0\rangle e^{-i(E-E')t}, \tag{1.15}$$

which is the product of the 'forward' amplitude $\langle x_0|e^{-iHt}|x_0\rangle$ and its complex conjugate, the 'backward' amplitude. Using Eq. (1.14) each of these amplitudes can be expressed as a sum over all sequences of scattering events. We refer to these as forward and backward paths, respectively. Averaging $\langle x_0|G^+(E)|x_0\rangle \langle x_0|G^-(E')|x_0\rangle$

over disorder, the contributions first order in V vanish. One of the contributions at second order[6] is

$$\sum_{x_1} \langle x_0|G_0^+(E)|x_1\rangle\, V(x_1)\, \langle x_1|G_0^+(E)|x_0\rangle \\ \times \sum_{x_1'} \langle x_0|G_0^-(E')|x_1'\rangle\, V(x_1')\, \langle x_1'|G_0^-(E')|x_0\rangle\,, \tag{1.16}$$

which corresponds to scattering at x_1 in the forward path, and at x_1' in the backward path. Now, because $V(x_1)$ and $V(x_1')$ are uncorrelated for $x_1 \neq x_1'$, averaging Eq. (1.16) over disorder forces the scattering events occurring in the forward and backward paths to take place at the same position. Such paths have conjugate amplitudes, so make a positive contribution to the probability. This generalises to higher orders, and at order v^{2n} one finds that the transition probability has contributions from pairs of forward and backward paths undergoing coherent scattering at the same sequences of n sites, $x_1, x_2, \ldots, x_n$. This is the sense in which the paths are 'paired'[7].

Another kind of pairing, between paths and their time-reversed partners, is behind the phenomenon of weak localisation [64, 65]. For example, with TRS the probability for an electron to return to where it started is doubled by constructive interference between time-reversed pairs of paths. Both equal-time and time-reversed pairings of electron paths are illustrated in Fig. 1.2. In diagrammatic perturbation theory they are known as diffusons and Cooperons, respectively [55].

This discussion indicates that, when the motion of the electrons in a disordered conductor is coherent, the introduction of a magnetic field has profound consequences for transport. This is because a magnetic field induces a phase difference between pairs of paths related by time-reversal. Passing a current around the circumference of a conducting cylinder, and varying an axial flux, one finds oscillations in the electric resistance with period equal to half of the standard flux quantum $2\pi\hbar/e$ [66, 67].

[6]The other contributions at this order modify the self energy appearing in the single-electron Green's function.

[7]Note that there are additional contributions, corresponding to 'crossed diagrams', where scattering events in the forward and backward paths occur in different orders.

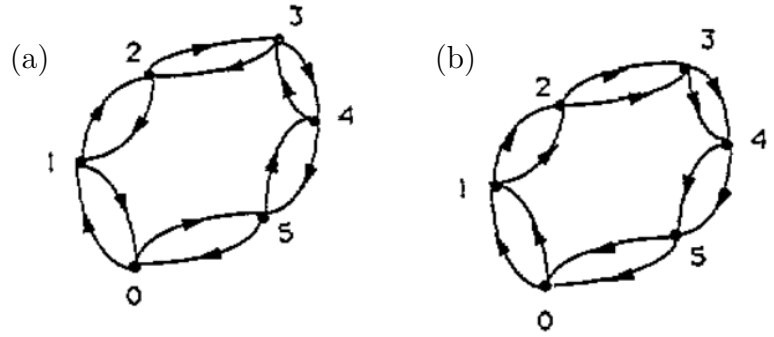

Figure 1.2: (a) Diffusons and (b) Cooperons, from Ref. [59]. In both cases the forward (outer) and backward (inner) real-space paths of electrons scatter from impurities (points) at the same sites. On the forward path the arrow indicates the direction of the electron, and on the backward the direction of the hole (opposite to the electron). In (a) the forward and backward paths scatter from impurities in the same order, in (b) the order in time is reversed.

1.2.2.2 Beyond RMT

The picture of paired electron paths, or disorder-averaged products of Green's functions, was developed into a field theory by Wegner [68]. Using this, and working in the limit of small Fermi wavelengths relative to the mean free path, Efetov demonstrated the emergence of RMT spectral statistics[8] [61].

Of course, this cannot be the whole story. The dynamics of the electrons is qualitatively different on different time scales. The characteristic velocity in the problem, v_F, is that of electrons at the Fermi surface, and the relevant length scales are the mean free path ℓ, and sample dimension L. For times $t < \ell/v_F$, the motion of the electrons is ballistic. Beyond ℓ/v_F the motion is diffusive, and with a diffusion constant D it will take a time $t_{\rm Th} \sim L^2/D$ for a wavepacket to spread over the sample, where $t_{\rm Th}$ is the Thouless time [70]. Only on timescales $t > t_{\rm Th}$ do we have cause to expect behaviour that is independent of sample details, and so behaviour characteristic of RMT.

However, as shown by Altshuler and Shklovskii, the deviations from RMT over energy intervals $E > E_{\rm Th} \equiv D/L^2$ exhibit a different kind of universality [62]. Here we outline their argument. The key observation is that over an energy interval E the spectrum of a block of linear dimension $L_E = (D/E)^{1/2}$ behaves as it would for

[8]Note, however, that the applicability of RMT in this setting was conjectured much earlier [69].

a random matrix. In a system of linear dimension $L \gg L_E$ the spectral statistics on scale E then behave as they would for $(L/L_E)^d$ blocks whose own systems of levels are, to a first approximation, independent.

First consider the number of levels $N(E, L_E)$ in an energy window of width E for a block of volume L_E^d. The scale of the fluctuations $\delta N(E, L_E)$ can be quantified by $\langle \delta N^2(E, L_E) \rangle$, which depends only on level correlations on energy scales E and smaller. We can therefore approximate it by the RMT result [71],

$$\langle \delta N^2(E, L_E) \rangle = \frac{2}{\pi^2 \beta} \ln \langle N(E, L_E) \rangle, \tag{1.17}$$

where β is the level-repulsion exponent for the symmetry class, for example $\beta = 2$ without TRS. By contrast, for Poisson-distributed energy levels the fluctuations are much more extreme, $\langle \delta N^2(E, L_E) \rangle = \langle N(E, L_E) \rangle$ with $\langle N(E, L_E) \rangle \propto L_E^d$.

Focusing on the same energy scale E, but in the full system with $L \gg L_E$, we now determine the scale of the fluctuations $\delta N(E) \equiv \delta N(E, L)$. If level fluctuations $\delta N(E, L_E)$ in the different blocks L_E^d are independent, we simply combine them in quadrature, and this gives $\langle \delta N^2(E) \rangle \simeq (L/L_E)^d \langle \delta N^2(E, L_E) \rangle$. Then, for $E > E_{\rm Th}$,

$$\langle \delta N^2(E) \rangle \simeq \frac{2}{\pi^2 \beta} (E/E_{\rm Th})^{d/2} \ln \Big[(E_{\rm Th}/E)^{d/2} \langle N(E) \rangle \Big], \tag{1.18}$$

where we have used $\langle N(E) \rangle = (L/L_E)^d \langle N(E, L_E) \rangle$. The spectrum is less 'rigid' on energy scales above $E_{\rm Th}$, but more so than for entirely uncorrelated levels. Note that this argument must break down at very high energies $E \sim v_F/\ell$, corresponding to timescales on which the electron motion is ballistic. Neglecting logarithmic corrections, Eq. (1.18) describes fluctuations with scale controlled only by a diffusion constant D, whose approximate value may be shared by systems that are very different microscopically.

Here crossovers in spectral statistics and in dynamics set in on the same scale $E_{\rm Th}$. Another route to this result was given by Argaman, Imry, and Smilansky, in a synthesis of ideas from mesoscopics and semiclassics [63]. The SFF can be expressed as a sum over pairs of orbits of the electrons, and as is clear from the above discussion of transport, the character of the orbits depends crucially on

their period. For period $t > t_{\mathrm{Th}}$ the orbits of electrons explore the sample, and RMT level statistics set in. For $t < t_{\mathrm{Th}}$ the electron wavepackets spread diffusively, and it is useful to think of the diagonal approximation to the SFF as the return probability multiplied by a factor t, corresponding to the orbit-pairing freedom. One then finds $\langle K(t)\rangle \sim t^{1-d/2}$ for $t < t_{\mathrm{Th}}$, and $\langle K(t)\rangle \sim t$ once the return probability reaches the inverse sample volume $1/L^d$.

1.2.2.3 Anderson localisation

This picture falls apart when the disorder is sufficiently strong, and the sample sufficiently large. It has been known since the early work of Anderson [58] that disorder may cause electron wavefunctions to localise. In the localised phase the electron motion is diffusive up to at most a finite localisation length ζ, which is a function of the energy [59].

To see why localisation can occur, it is helpful to again consider the model $H = H_0 + V$ for electrons hopping in a disordered medium, but now to treat the kinetic term H_0 as a perturbation. The eigenstates of V are localised on sites of the lattice, and we must ask which are hybridised in perturbation theory. Note then that nearby pairs of sites typically have very different energies, so the hybridisation between them is weak, and that pairs of sites which do have similar energies are typically far apart in space. Consequently, if the disorder is strong enough, one finds that wavefunctions $\psi(x)$ are exponentially localised, $\psi(x) \sim e^{-x/\zeta}$. Note also that, if H_0 can be treated perturbatively as suggested above, the spectrum of H will resemble that of V: for $L \gg \zeta$ typical pairs of localised wavefunctions do not overlap in space, so their energies do not repel from one another. We have chosen $V(x)$ to be uncorrelated random numbers, i.e. distributed according to a Poisson process, so the spectral statistics do not resemble those of a random matrix.

Of course, localisation has striking signatures in the dynamics of electrons. When the Fermi energy lies in a region of the spectrum where wavefunctions are localised, the low-temperature transport properties can be understood by considering hopping between these localised states [72, 73]. This picture successfully predicts various

transport properties of disordered semiconductors. For example, zero-frequency conduction requires a thermal bath of phonons, so one finds a rapid decrease of the conductivity at low temperatures[9] [74].

An understanding of when localisation should occur followed some years after Ref. [58], with the development of scaling theory [75]. At least two contributions in this direction are relevant here. First, there is the work of Thouless and coworkers on the sensitivity of the spectrum to changes in the boundary conditions [70, 76, 77], and the relation to transport properties. It is natural to expect that the energy of a wavefunction localised far from the boundaries of a sample will be insensitive to changes that occur there. The same cannot be said of an extended wavefunction. Second is the formulation of the localisation problem in the language of the renormalisation group by Wegner [78]. And, in particular, the subsequent work showing that the transition from localised to extended wavefunctions can be understood as a symmetry-breaking phase transition in a field theory [68].

1.3 More degrees of freedom

Leaving billiards and individual electrons behind, we now proceed to the many-body setting. How pictures of paired paths appear here, and how they must be modified, is the subject of this thesis. As a prelude, in the remainder of the introduction we discuss standard theories for the dynamics of many-body systems. In Secs. 1.3.1, 1.3.2, and 1.3.3 we will be concerned with the respective emergence and failure of statistical mechanics in ergodic [9, 10] and MBL systems [27, 28]. Throughout, we highlight connections to RMT. In Sec. 1.3.4 we introduce the class of minimal models for many-body dynamics, quantum circuits, which is used in this work.

1.3.1 Eigenstate thermalisation

How it is that thermodynamic equilibrium can emerge from the unitary dynamics of a closed quantum system is not at first obvious. Nor is the fact that thermal

[9] In three spatial dimensions this behaviour is known as Mott's $T^{-1/4}$ law. More generally, the conductivity $\sigma \sim \exp[-T^{-1/(d+1)}]$ in d spatial dimensions.

equilibrium is encoded in the properties of individual eigenstates. This section is concerned with the eigenstate thermalisation hypothesis (ETH).

The first step, due to Deutsch [7], is to see how quantum expectation values of observables can coincide with their microcanonical averages. For this to occur, fluctuations in the expectation values between nearby eigenstates must be small. There is a sense, then, in which nearby eigenstates are statistically similar. Consider a many-body system with local Hilbert space dimension q, L sites, and Hamiltonian

$$H = \sum_{x=0}^{L-1} h_x + \lambda V, \tag{1.19}$$

where h_x are Hermitian $q \times q$ matrices which act at the different sites x and have eigenvalues of order unity. The operator V represents coupling between the different sites, and also has eigenvalues of order unity.

First, for $\lambda = 0$, no information is exchanged between different regions, so the system cannot equilibrate. We denote the eigenstates of h_x by $|i_x\rangle$ so that $h_x |i_x\rangle = \varepsilon_{x,i_x} |i_x\rangle$. For $\lambda = 0$ the eigenstates of H are tensor products $|i_0\rangle \otimes |i_1\rangle \otimes \ldots$ with energies $\varepsilon_{0,i_0} + \ldots + \varepsilon_{L-1,i_{L-1}}$. If the different local Hamiltonians h_x have statistically independent levels ε_{x,i_x}, for large L nearby energy levels of H are uncorrelated. Additionally, the expectation values of local observables exhibit large fluctuations between neighbouring eigenstates.

Now switch on V. In the middle of the spectrum the separation between neighbouring eigenvalues $\Delta \sim L/q^L$, so we cannot treat λV as a perturbation for any finite λ when L is large. The eigenstates of H for $\lambda \neq 0$ are instead constructed from the hybridisation of sets of $\sim \lambda/\Delta$ levels that are within energy $\sim \lambda$ of one another. It is this hybridisation which causes the expectation values of observables, computed even in individual eigenstates, to reflect the average properties of the system at this energy scale.

A toy model for this effect is as follows: choose λ and a central energy E in the bulk of the spectrum, and restrict to the subspace spanned by the $N \sim \lambda/\Delta$ eigenstates of the $\lambda = 0$ system closest to E. We can always increase L so that

$N \gg 1$ while maintaining $\lambda \ll E$. An approximate description of the eigenstates in this window, for $\lambda \neq 0$, is

$$|n\rangle = \sum_{i_0 i_1 \ldots}{}' U_{n,i_0 i_1 \ldots} \, |i_0 i_1 \ldots\rangle \,, \tag{1.20}$$

where the sum only runs over those N states $|i_0 i_1 \ldots\rangle$ in the energy interval of interest, and U is a $N \times N$ unitary matrix. The expectation value of a local observable O is

$$\langle n|O|n\rangle = \sum_{\substack{i_0 i_1 \cdots \\ j_0 j_1 \cdots}}{}' U_{n,i_0 i_1 \ldots} U^*_{n,j_0 j_1 \ldots} \, \langle i_0 i_1 \ldots |O| j_0 j_1 \ldots\rangle \,. \tag{1.21}$$

For U Haar random, we have the average $\langle U_{n,i_0 i_1 \ldots} U^*_{n,j_0 j_1 \ldots}\rangle = (1/N)\delta_{i_0 j_0}\delta_{i_1 j_1} \ldots$. The average of Eq. (1.21) over U is then the average of $\langle i_0 i_1 \ldots |O| i_0 i_1 \ldots\rangle$ over the energy window. This effect suppresses the fluctuations. To see this, we compute the variance of $\langle n|O|n\rangle$ over U. The result, for large N, is

$$\mathrm{Var}\, \langle n|O|n\rangle = \frac{1}{N^2} \sum_{\substack{i_0 i_1 \cdots \\ j_0 j_1 \cdots}}{}' |\, \langle i_0 i_1 \ldots |O| j_0 j_1 \ldots\rangle \,|^2. \tag{1.22}$$

The sum on the right-hand side side is a trace of O^2 within the N-dimensional space. For local O, we find fluctuations in $\langle n|O|n\rangle$ that are exponentially small in L. The expectation value $\langle n|O|n\rangle$ for any one eigenstate $|n\rangle$ in the energy window therefore approximates the average over it[10].

The second step is due to Srednicki. It was shown in Ref. [8] that Berry's conjecture for the structure of many-body wavefunctions [79] leads to thermal distributions for local observables in individual eigenstates. No thermal ensemble need be put in 'by hand' as the information is encoded in any one eigenstate. This is to be contrasted with the classical situation, where an average over time, or over initial states, is used to justify the application of equilibrium statistical mechanics.

The ETH now has extensive numerical support [see for example Ref. [80]]. Its standard formulation is an ansatz for the matrix elements of local observables, written in the basis of eigenstates of a many-body Hamiltonian. For a Hamiltonian

[10] To estimate the scale of the fluctuations it is helpful to consider the case $N = q^L$. The sum in Eq. (1.22) is then the trace $\mathrm{Tr}O^2$ over the entire Fock space. For each site where O acts as the identity, this trace acquires a factor q, so that $\mathrm{Tr}O^2 \sim q^L$ for local O. The variance in Eq. (1.22) is then of order q^{-L}.

H with energy levels E_n and corresponding eigenstates $|n\rangle$, the ETH states that the matrix elements of the local observable O take the form [81]

$$\langle n|O|m\rangle = \overline{O}(E)\delta_{nm} + e^{-S(E)/2} f(E,\omega) R_{nm}. \tag{1.23}$$

Here the mean energy $E = (E_n + E_m)/2$, and the separation $\omega = E_n - E_m$. The function $\overline{O}(E)$ is chosen to give the microcanonical average. This is because, from the form of Eq. (1.23), it gives the time-independent contribution to quantum expectation values. $S(E)$ is the thermodynamic entropy, $f(E,\omega)$ is a smooth function of its arguments, and R_{nm} are random numbers with zero mean and unit variance. The structure of Eq. (1.23) is clearly motivated by RMT, and from it one recovers familiar thermodynamic behaviour. Those quantum systems for which the ETH is appropriate make up the ergodic phase.

1.3.2 Many-body quantum chaos

For an ergodic quantum system to act as its own bath, and so for the ETH to hold, different regions must be able to exchange information. In this way, states which at first appear very different to local measurements can approach the same states of local equilibrium. There are two sides to this: thermalisation as viewed by operators, and as viewed by states.

First we must discuss the notion of locality in many-body systems with local interactions. This was addressed some time ago by Lieb and Robinson [82]. A Heisenberg operator O_0 which at time $t = 0$ is local to a site $x = 0$ will commute with operators local to different sites. However, as t increases the support of $O_0(t) = e^{iHt} O_0 e^{-iHt}$ will generally grow. By looking at the scale of the commutator between $O_0(t)$ and operators O_x local to $x \neq 0$, we can quantify the speed at which information propagates. For H with finite-range interactions the result is that for $x > v_L t$, where v_L is a velocity, a suitable norm of the commutator $[O_0(t), O_x]$ is bounded by a function that decays exponentially with $|x - v_L t|$. There is therefore a kind of lightcone, but it is not strict. This discussion does not, however, give

us any information on the form of the evolving operator. For example $O_0(t)$ may evolve ballistically, acting non-trivially only near the lightcone edges.

In chaotic many-body quantum systems, local operators evolve into highly complex objects, linear combinations of tensor products of many well-separated local operators; information that is initially local is scrambled [14–16]. A natural way to characterise this phenomenon is to probe the support of the spreading operator, i.e. the size of the region on which it acts non-trivially. In models with local interactions, one can then arrive at a picture of a growing 'droplet' [12, 13]. Following Ref. [83], consider the unitary evolution operator $W(t)$, and single-site observables O_x that square to the identity. A probe of whether $O_0(t) = W^\dagger(t)O_0W(t)$ and O_x commute is

$$C(x,t) = 1 - \frac{1}{2}\mathrm{Tr}O_0(t)O_xO_0(t)O_x, \tag{1.24}$$

where the trace is over the many-body Fock space. The second term is the out-of-time-order correlator (OTOC). The quantity $C(x,t)$ directly probes the spatial extent of $O_0(t)$, and one finds that the 'front' of the droplet travels ballistically in chaotic quantum systems. Note that the OTOC is not a traditional observable as it involves multiple copies of the evolution operator and its conjugate. It has nevertheless been probed using modern experimental techniques [84, 85].

From the perspective of states, thermalisation is associated with entanglement. To see this, note that for expectation values of local observables to reproduce their microcanonical averages, reduced density matrices must become thermal. With local interactions it is helpful to partition the system into regions A and B, and to write $H = H_A + H_B + H_{AB}$, where H_A and H_B act only on degrees of freedom within the respective regions, and H_{AB} describes coupling at their boundary. The reduced density matrix of A is

$$\rho_A = \frac{1}{Z}\mathrm{Tr}_B e^{-\beta H} \simeq \frac{1}{Z_A}e^{-\beta H_A}, \tag{1.25}$$

where we have neglected the contribution H_{AB} relative to H_A, and have defined $Z_A = \mathrm{Tr}_A e^{-\beta H_A}$. This amounts to the assumption that the temperature of A

can be estimated from a local energy density. The von Neumann entanglement entropy of A is then

$$S_A \equiv -\mathrm{Tr}\rho_A \ln \rho_A \simeq \ln Z_A + \beta \langle H_A \rangle , \tag{1.26}$$

where $\langle H_A \rangle$ is the thermal expectation value of H_A. We see that S_A coincides with the thermal entropy, so is extensive. Starting from a weakly-entangled quantum state, thermalisation requires that the entanglement entropy of a subregion grow until it reaches an extensive thermal value. In fact, in chaotic quantum systems the von Neumann entropy grows linearly [18]. Measuring the von Neumann entropy is inherently difficult because the logarithm of a density matrix appears. The second Renyi entropy $S_A^{(2)} = -\ln \mathrm{Tr}\rho_A^2$ has, however, been measured in ultracold gas [86, 87] and trapped ion experiments [88]. In particular, the relation between entanglement growth and thermalisation was studied in Ref. [87].

Alongside dynamical signatures such as operator spreading and entanglement, a third signature of many-body quantum chaos is the appearance of random-matrix spectral statistics [34, 89, 90]. This is the subject of Chapter 2.

1.3.3 Many-body localisation

In quantum many-body systems there is a generic alternative to thermalisation, at least in one dimension [27, 28]. This can occur if information is localised. As discussed in Sec. 1.2.2, this certainly occurs for electrons in the presence of disorder provided they do not interact. An interesting question is whether localisation can survive when they do.

The problem was first approached some time ago [91], but its recent history can be traced to the diagrammatic treatments of Refs. [22] and [23]. Both indicated an exact vanishing of the conductivity below a finite critical temperature[11]. Oganesyan and Huse took a different route [24]. Relying instead on exact diagonalisation (ED) of small systems, they demonstrated a transition in the high-energy region of the many-body spectrum. For systems with a finite local Hilbert space dimension,

[11] The existence of a many-body mobility edge has since been cast into some doubt [92].

and in the presence of sufficiently strong disorder, this result suggests insulating behaviour at arbitrarily high energies.

The resulting many-body localised (MBL) phase is characterised by its failure to thermalise under unitary dynamics [27, 28]. It is, however, unstable against coupling to a thermalising environment[12]. Experimental observations of MBL behaviour have therefore only been possible in well-isolated systems such as cold atoms [93] and trapped ions [94]. Theoretically, the phase is understood in terms of the emergence of an extensive number of locally conserved operators, or local integrals of motion (LIOM) [29–32], whose existence prohibits conventional equilibration. These are operators $\tilde{\tau}_x$ whose support decays exponentially with distance from site x. In terms of the LIOM the phenomenological model of the MBL phase takes the form

$$H = \sum_x \mathcal{K}_x^{(1)} \tilde{\tau}_x + \sum_{x \neq x'} \mathcal{K}_{xx'}^{(2)} \tilde{\tau}_x \tilde{\tau}_{x'} + \dots \tag{1.27}$$

All of the $\tilde{\tau}_x$ commute with one another, and therefore with H, so they have no dynamics. The coefficients $\mathcal{K}^{(n)}$ describe n-body couplings that also decay exponentially, for example $\mathcal{K}_{xx'}^{(2)} \sim e^{-|x-x'|/\zeta}$ where ζ is a decay length.

An interesting consequence of the LIOM, which further emphasises the highly non-thermal behaviour of the MBL phase, is that eigenstates have area-law entanglement [26, 33]. This means that the various reduced density matrices cannot correspond to fixed-temperature Gibbs distributions. Also predicted by this picture is a novel logarithmic growth of the entanglement entropy between subsystems [25, 95–97] [see also Ref. [98] for an experimental observation], to be contrasted with the linear growth expected in thermalising systems.

Finally, it is clear from the results of Ref. [24] that the emergent integrability of the MBL phase has dramatic consequences for the spectral statistics. Typical pairs of neighbouring levels do not repel from one another in the thermodynamic limit. As a result their distribution is, to a first approximation, a Poisson process. The transition from MBL to ergodic behaviour is therefore associated with the emergence of RMT level statistics. This is the subject of Chapter 3.

[12] In particular, it is unstable against the thermally-activated hopping processes discussed toward the end of Sec. 1.2.2

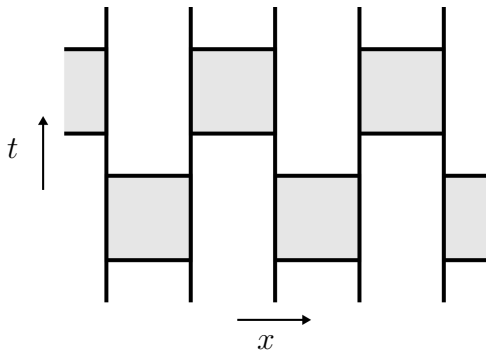

Figure 1.3: Diagram of the evolution operator for a unit time step in a brickwork quantum circuit. Time runs vertically and space horizontally, with vertical lines marking positions of the sites. Grey boxes represent unitary matrices acting on pairs of sites.

1.3.4 Quantum circuits

Many-body quantum chaos, and many-body localisation, are the two phases of unitary dynamics of interest here. In the first, local information is scrambled. In the second, it is not. In the Hamiltonian setting this is the reason for these phases' respective success and failure in bringing observables to local thermodynamic equilibrium. However, scrambling can be studied outside of the Hamiltonian setting: a minimal model need only describe local unitary dynamics.

Unitary quantum circuits describe discrete time evolution in lattice models [12, 13, 20, 99–103]. For example, in a lattice whose sites carry 'spin' degrees of freedom with local Hilbert space dimension q, pairs of sites may be coupled by $q^2 \times q^2$ unitary gates. This is illustrated in Fig. 1.3 for a one-dimensional system and an evolution operator with the standard brickwork structure. Following the spirit of RMT, many useful insights have been obtained by considering quantum circuits in which gates are drawn from a random distribution. Physical properties can then be averaged over an ensemble to reveal behaviour generic to entire classes of systems [12, 13, 20, 104, 105]. In random unitary circuits (RUCs) the unitary matrices coupling pairs of sites are drawn independently at each time step. Because of this, some averaged properties of the time evolution can be computed analytically for all values of q. This simplicity has allowed for the development and investigation of the droplet model of operator spreading [12, 13], as well as the membrane picture of entanglement growth [20, 106–108].

Although RUCs have shed light on the dynamical aspect of many-body quantum chaos, because they have no fixed evolution operator they shed no light its connection

to spectral statistics. Additionally, without a fixed evolution operator, it is not clear how LIOM could be constructed; RUCs cannot host a standard MBL phase. To study spectra it is necessary to generalise RUCs, and in this way we arrive at random Floquet circuits (RFCs) [34–36, 109]. The RFCs we study also have the structure shown in Fig. 1.3, but the $q^2 \times q^2$ unitary matrices are the same for successive time steps. Note that RFCs may equally be viewed as examples of kicked spin chains, which have been studied extensively in their own right [89, 90, 110–113].

The generalisation to RFCs poses a severe increase in analytic complexity, although the large-q limit remains amenable to an exact analysis [34, 109]. There is nevertheless a strong interest in understanding their properties because time evolution in a RFC provides information on the spectral and eigenstate correlations of the evolution operator for a simple form of local many-body dynamics. In Chapters 2 and 3 we study generic aspects of this dynamics, and in order to do so develop a variety of theoretical techniques. Our results are summarised in Chapter 4, where we also indicate promising future directions.

2
Local pairing

RMT and the ETH provide a baseline description of spectral properties in the ergodic phase [6–11, 38, 41, 50, 80]. In this chapter we identify when these approximations are accurate, and characterise the behaviour when they break down, focusing on the regime of large time and length scales for which one can expect a degree of universal behaviour. To do this, working with RFCs, we start from expressions for physical properties in terms of multiple sums over paths in the many-body Fock space. The applicability of RMT and the ETH can be understood through the diagonal approximation, and our main result is to show how it must be extended in Floquet models with local interactions.

For the physical properties we focus on, the SFF and a class of matrix-element correlators, the relevant Fock-space paths are closed, so we often refer to them as orbits. We show that properties are dominated at late times by contributions to orbit sums in which each orbit is paired locally with a conjugate, as in the diagonal approximation, but that in large systems these contributions consist of many spatial domains, with distinct local pairings in neighbouring domains. The existence of these domains is reflected in deviations of the SFF from RMT predictions, and of matrix element correlations from ETH predictions; deviations of both kinds diverge with system size.

In RFCs this physical picture of pairing domains has a precise correspondence in the spectral properties of a transfer matrix that acts in the space direction to generate the ensemble-averaged SFF. Questions about the pairings of paths that contribute to the ensemble-averaged SFF, and a class of matrix element correlators, can be rephrased as questions about the eigenvectors associated with the leading eigenvalues of this transfer matrix. Similarly, deviations in behaviour from RMT and ETH predictions are controlled by the behaviour of these eigenvalues as a function of time, t.

This work builds on and complements other recent research in a number of ways. Most directly, the possibility that domains arise in the pairing of the orbits contributing to the SFF was shown for a model solvable in the large-q limit in Ref. [109]. Here we show how to formulate and test this idea in a generic setting, and demonstrate that it has consequences beyond the behaviour of the SFF. The idea of using a transfer matrix to generate the SFF and related quantities has been applied previously [35, 112–115]. This approach arose from discussions of periodic orbits in many-body systems [116], was developed as a method for treating kicked spin chains [112], and has been elaborated further as a way of accessing the semiclassical limit and making connections with periodic orbit theory [113, 114]. Such a transfer matrix also forms the basis for the analysis of self-dual kicked spin chains [35, 117], which display exact RMT behaviour of the SFF. Away from the self-dual point, recent work has investigated the evolution of this transfer matrix from ergodic to many-body localised behaviour [115]. The important distinction between those works and ours is that we are concerned with generic behaviour unrelated to self-duality, and at late times. We note also that another connection between the spectral properties of a transfer matrix and the pairing of Fock-space paths has recently arisen in studies of thermalisation [118–121].

The remainder of this chapter is organised as follows. In Sec. 2.1 we introduce the models considered, in particular RFCs constructed from unitary matrices drawn from the Haar distribution (Haar-RFCs). Sec. 2.2 then describes how sums over Fock-space paths appear in our calculations. In Sec. 2.3 we will see that the diagonal

approximation to the average SFF breaks down, and in Sec. 2.4 we set up the transfer matrix framework to describe how. In Sec. 2.5 we develop techniques to study this transfer matrix at late times in order to determine its asymptotic behaviour, and numerically probe the pairing domains. Sec. 2.6 shows how to take advantage of its analytic structure in order to access the subleading eigenvalues. Before moving away from the average SFF, we extend our discussion to a more general class of models in Sec. 2.7. Then, in Sec. 2.8, we discuss statistical fluctuations of the SFF. By writing the higher moments of the SFF in terms of multiple sums over paths, we show that a distinct freedom in their local pairing gives rise to non-Gaussian statistics. We also highlight a connection with the entanglement membrane, known to characterise the scrambling of quantum information [20, 106–108]. In Sec. 2.9 we show that the existence of pairing domains implies strong correlations between the diagonal matrix elements of local observables. We summarise our results in Sec. 2.10.

2.1 Models and definitions

Our focus is on one-dimensional Floquet circuits with brickwork structure [34], illustrated in Fig. 1.3. The unitary evolution operator for integer time t is $W(t) \equiv W^t$, where $W = W_2 W_1$ is the Floquet operator. With local Hilbert space dimension q, and with L sites, these operators can be represented as $q^L \times q^L$ matrices. We denote by $N = q^L$ the Fock space dimension. In brickwork models W_1 and W_2 are tensor products of two-site ($q^2 \times q^2$) unitary matrices $U_{x,x+1}$ coupling alternate pairs of neighbouring sites $(x, x+1)$. We label sites $x = 0, 1 \ldots (L-1)$. For periodic boundary conditions, which necessitates L even, we have

$$\begin{aligned} W_1 &= U_{0,1} \otimes U_{2,3} \otimes \ldots \otimes U_{L-2,L-1} \\ W_2 &= U_{1,2} \otimes U_{3,4} \otimes \ldots \otimes U_{L-1,0}. \end{aligned} \tag{2.1}$$

With open boundary conditions and L even we replace $U_{L-1,0}$ with the $q^2 \times q^2$ identity matrix. With open boundary conditions and L odd we instead have

$$\begin{aligned} W_1 &= U_{0,1} \otimes U_{2,3} \otimes \ldots U_{L-3,L-2} \otimes \mathbb{1} \\ W_2 &= \mathbb{1} \otimes U_{1,2} \otimes U_{3,4} \otimes \ldots U_{L-2,L-1}, \end{aligned} \tag{2.2}$$

where now $q \times q$ identity matrices act on site $x = (L-1)$ in W_1, and on $x = 0$ in W_2. In this chapter $U_{x,x+1}$ are Haar-random, so W is the Floquet operator for a Haar-RFC. Our numerical investigations focus on a local Hilbert space dimension $q = 2$, when the model is a form of kicked spin-1/2 chain.

We are motivated in part by properties of the random phase model (RPM), another RFC. This model was introduced in Ref. [109], and its Floquet operator

$$W = \exp\left[i \sum_{x=0}^{L-1} \varphi_{x,x+1}\right] \bigotimes_{x=0}^{L-1} u_x. \tag{2.3}$$

Here u_x are independent single-site $(q \times q)$ Haar-random unitary matrices, and $\varphi_{x,x+1}$ are diagonal $q^2 \times q^2$ matrices acting on neighbouring pairs of sites $(x, x+1)$, whose elements are Gaussian-random real numbers with zero mean and variance ε. With open boundary conditions we set $\varphi_{L-1,0} = 0$.

Haar-RFCs and RPMs, as defined above, do not have TRS. At late times and in the ergodic phase we therefore expect the ensemble average of the SFF $\langle K(t)\rangle \simeq t$ for $t_{\mathrm{Th}} < t < t_{\mathrm{H}}$ [c.f. Eq. (1.4)]. We refer to the timescale t_{Th} beyond which RMT behaviour of the SFF sets in as the Thouless time [109, 122–125] [see also Ref. [36]]. We note however that there are a number of alternative definitions, based on the behaviour of local observables [126], the sensitivity to boundary conditions [127], and on many-body return probabilities [128].

2.2 Sums over paths

In systems with local interactions the amplitudes of different Fock-space paths are correlated. To see this consider the amplitude for evolution, in time t, from many-body state $|a_0\rangle$ to $|a_t\rangle$,

$$\langle a_t|W(t)|a_0\rangle = \sum_{a_1 \ldots a_{t-1}} W_{a_t a_{t-1}} \ldots W_{a_1 a_0}. \tag{2.4}$$

This is a discrete sum over paths $(a_0 a_1 \ldots a_t)$, with $a_r = 0 \ldots (N-1)$. The amplitude for each of these paths is simply a product of t matrix elements of W. Although W has q^{2L} entries, for a brickwork model of the form in Eq. (2.1) it has only Lq^4 real degrees of freedom. For large L it is therefore natural to expect strong correlations

between the different transition amplitudes. In Sec. 2.2.1 we outline the form of the diagonal approximation in this setting, and in Sec. 2.2.2 indicate how we will extend it. Sec. 2.2.3 discusses the role of averaging.

2.2.1 Diagonal approximation

The diagonal approximation takes its simplest form for transition probabilities. The probability for evolution from $|a_0\rangle$ to $|a_t\rangle$ in time t is simply the modulus square of the amplitude Eq. (2.4),

$$|\langle a_t|W(t)|a_0\rangle|^2 = \sum_{a_1\ldots a_{t-1}} W_{a_t a_{t-1}}\ldots W_{a_1 a_0} \times \sum_{a_1^*\ldots a_{t-1}^*} W^*_{a_t a_{t-1}^*}\ldots W^*_{a_1^* a_0}, \qquad (2.5)$$

which is a discrete sum over pairs of paths in Fock space. The forward paths are $(a_0 a_1 \ldots a_{t-1} a_t)$, and the backward paths are $(a_0 a_1^* \ldots a_{t-1}^* a_t)$, with $a_r, a_r^* = 0 \ldots (N-1)$. The weights of the N^{t-1} diagonal pairs of paths, with $a_r = a_r^*$ for all r, give real non-negative contributions to Eq. (2.5). If the weights of the $N^{t-1}(N^{t-1}-1)$ off-diagonal pairs behave like a set of independent random variables, their sum gives a real contribution of the same order as the sum of the diagonal pairs. The off-diagonal contributions may, however, vanish after a suitable average. Neglecting them, we arrive at the diagonal approximation.

The dynamics within the diagonal approximation is described by the diagonal propagator $\mathcal{P}$, which could also be thought of as the analogue of a diffuson in Fock space,

$$\mathcal{P}_{a_{r+1}a_r} = W_{a_{r+1}a_r} W^*_{a_{r+1}a_r}. \qquad (2.6)$$

From this we would find a transition probability $|\langle a_t|W(t)|a_0\rangle|^2 = \langle a_t|\mathcal{P}^t|a_0\rangle$. To make analytic progress within the diagonal approximation, it is useful to approximate the average $\langle \mathcal{P}^t\rangle \simeq \langle \mathcal{P}\rangle^t$. This amounts to the assumption that the average can be performed independently for each step. In this way the dynamics is controlled only by the eigenvalues of the average diagonal propagator $\langle \mathcal{P}\rangle$. For definiteness in the following we use the term diagonal approximation to refer to calculations based on $\langle \mathcal{P}\rangle$. We discuss this further below in connection with Fig. 2.5. Unitarity

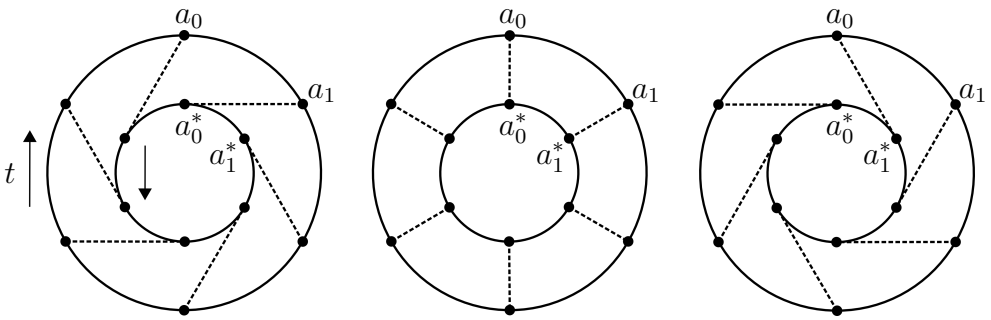

Figure 2.1: Three of the diagonal many-body orbit pairings that contribute to the spectral form factor $K(t) = \mathrm{Tr}W(t)\mathrm{Tr}W^*(t)$. Outer circles represent the forward orbit, and inner the backward, corresponding to terms in the sum-over-paths representations of $\mathrm{Tr}W(t)$ and $\mathrm{Tr}W^*(t)$, respectively. Dashed lines indicate the diagonal pairing of forward and backward orbits, with $a_r = a^*_{r+s}$. From left to right we show $s = -1, 0$ and 1.

constrains $\langle\mathcal{P}\rangle$ to be a doubly stochastic matrix (the sum of entries along any row or column is unity), so it has a leading eigenvalue of unity.

To construct the SFF in the diagonal approximation we write $\mathrm{Tr}W(t)$ as a sum over all closed paths or orbits of t steps, $(a_0 a_1 \dots a_{t-1})$, where a_0 follows a_{t-1} as in Eq. (1.5). From Eq. (1.6) the SFF is a sum over all pairs of forward $(a_0 a_1 \dots a_{t-1})$ and backward $(a_0^* a_1^* \dots a_{t-1}^*)$ orbits. With a fixed evolution operator W the amplitude of an orbit does not depend on where it starts. Consequently, in a system without time-reversal symmetry, for a typical forward orbit there are t backward orbits with the complex conjugate amplitude, having $a^*_{r+s} = a_r$ for any $s = 0 \dots (t-1)$. In Fig. 2.1 we illustrate three of these diagonal orbit pairings. The diagonal approximation to the average SFF is

$$\langle K(t)\rangle = t\mathrm{Tr}\langle\mathcal{P}\rangle^t. \tag{2.7}$$

For an average propagator with just one unit-modulus eigenvalue, $\mathrm{Tr}\langle\mathcal{P}\rangle^t \to 1$ at late times. The diagonal approximation to the SFF therefore approaches the RMT result in Eq. (1.4) for $t < t_H$. As discussed above, however, for a large system with local interactions the dimension of W far exceeds the number of real degrees of freedom. The amplitudes of the different paths are certainly not independent random variables.

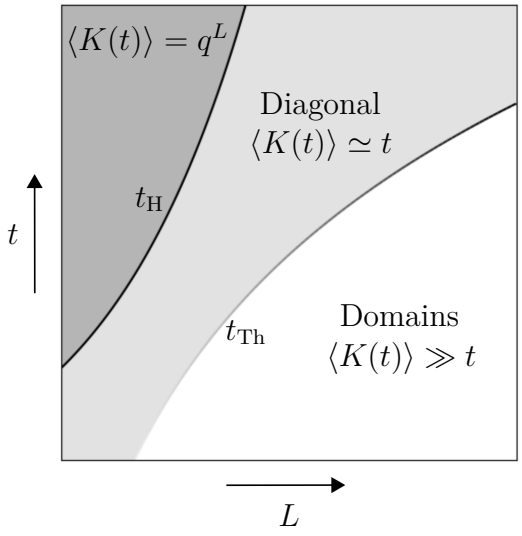

Figure 2.2: Behaviour of the average SFF $\langle K(t)\rangle$ for different t and L. For $t < t_{\rm H} = q^L$ the average $\langle K(t)\rangle$ is controlled by no more than t eigenvalues of $\langle \mathcal{T}(t)\rangle$. For $t_{\rm Th} < t < t_{\rm H}$, where $t_{\rm Th} = t_{\rm Th}(L)$ is the Thouless time, $\langle K(t)\rangle \simeq t$, corresponding to a orbits paired in a single domain. For $t < t_{\rm Th}$ and large L, $\langle K(t)\rangle \gg t$, corresponding to multiple domains.

2.2.2 Transfer matrices

To emphasise the local structure of $\mathrm{Tr}W(t) = \sum_{a_0 \ldots a_{t-1}} W_{a_0 a_{t-1}} \ldots W_{a_1 a_0}$ it is useful to express it as follows. In a local basis the sum over each $a_r = 0 \ldots (q^L - 1)$ can be recast as a sum over each of the q different states $0 \ldots (q-1)$ at each of the L sites[1]. In this way $\mathrm{Tr}W(t)$ becomes a sum over all site-local orbits. With nearest-neighbour interactions this sum can be generated by spatial transfer matrices, which can be thought of as acting on the site-local orbits. The SFF $K(t) = |\mathrm{Tr}W(t)|^2$ is then a product of transfer matrices which act on pairs of local orbits. We discuss this in detail in Sec. 2.4, and here outline the construction.

The transfer matrix for bond $(x, x+1)$ is associated with the gate $U_{x,x+1}$, and we denote it by $\mathcal{T}_{x,x+1}(t)$. With open boundary conditions we find, for example,

$$K(t) = \langle \mathcal{B}_L | \, \mathcal{T}_{0,1} \mathcal{T}_{2,3} \ldots \mathcal{T}_{L-2,L-1} \, | \mathcal{B}_R \rangle \, . \tag{2.8}$$

Here $\langle \mathcal{B}_L|$ and $|\mathcal{B}_R\rangle$ are vectors encoding the boundary conditions at the left and right ends of the system, respectively [see above Eq. (2.28)]. For independently and identically distributed gates the average SFF is determined by powers of the average transfer matrix $\langle \mathcal{T}(t)\rangle$,

$$\langle K(t)\rangle = \langle \mathcal{B}_L | \, \langle \mathcal{T}(t)\rangle^{L-1} \, | \mathcal{B}_R \rangle \, . \tag{2.9}$$

[1]Note that, for the Haar-RFCs we study, all choices of site basis are statistically equivalent.

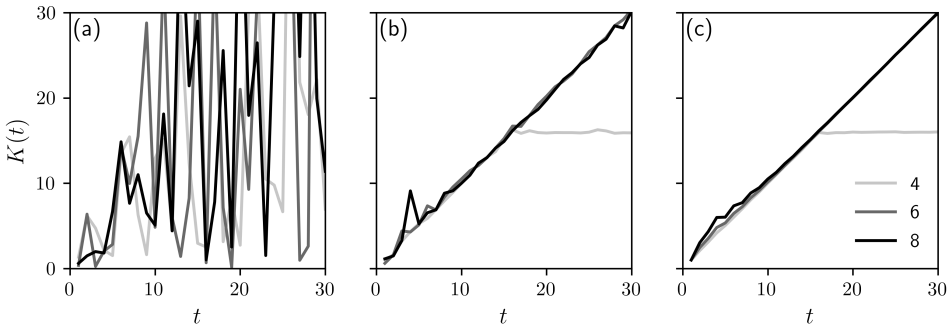

Figure 2.3: SFF $K(t)$ of the Haar-RFC with different degrees of averaging. All data is for periodic boundary conditions with the number of sites L shown on the legend. (a) No averaging: for each L this is the SFF for an individual realisation of the gates. (b) Average over only a single gate, with all others fixed. (c) Average over all of the gates.

Fixing t, for large L we will show that in the regimes of interest $\langle K(t)\rangle$ is dominated by contributions from just t leading eigenvalues of $\langle \mathcal{T}(t)\rangle$. The behaviour of $\langle K(t)\rangle$ for various t and L, which we establish in Sec. 2.5, is illustrated in Fig. 2.2.

2.2.3 Averaging

With few exceptions, our focus is on ensemble-averaged quantities. Some form of averaging is necessary to study correlations between the amplitudes of different many-body orbits, and also to identify behaviour which has some hope of being generic. Moreover, the SFF is not self-averaging [129], and typically exhibits large system-dependent fluctuations around the RMT result [130].

Averaging can in principle be approached in a number of ways. For a specific model or a specific realisation drawn from an ensemble, one can average the SFF over a time window. This window should be narrow on the scale set by its mid-point, to avoid distortion, but wide enough to contain many Floquet periods, to ensure efficient averaging [129]. Alternatively, one can average over a small region in the space of possible models. In this case the average may be representative of all systems in this region, but system-dependent fluctuations will be washed out only at late times. Although our transfer-matrix approach relies on averaging each independent gate, in practice quite limited averaging is sufficient: in Fig. 2.3 we

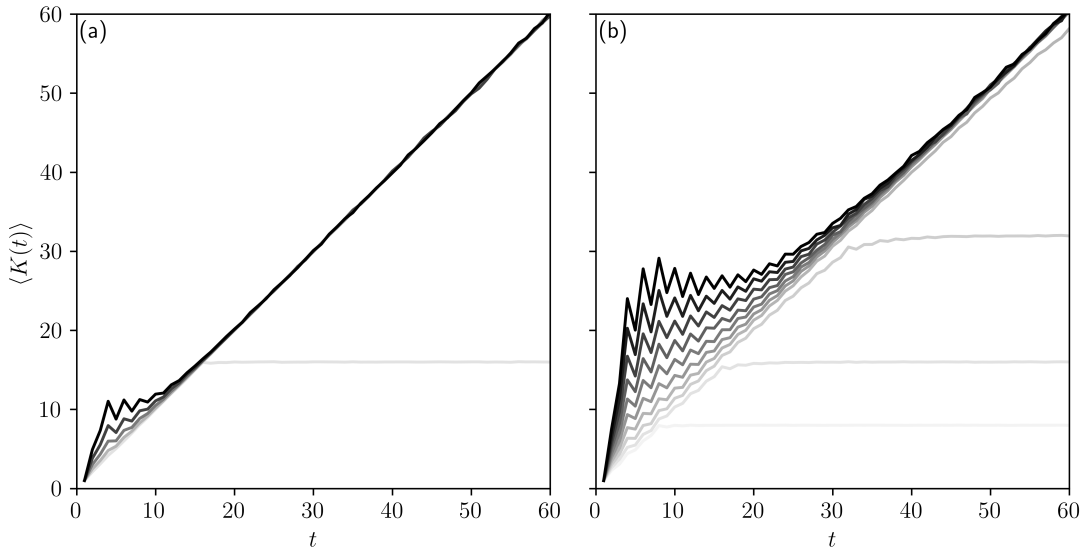

Figure 2.4: Average SFF $\langle K(t)\rangle$ in the $q = 2$ brickwork model with (a) periodic and (b) open boundary conditions. For fixed t, $\langle K(t)\rangle$ increases with L. Here $3 \leq L \leq 12$, and L is necessarily even with periodic boundary conditions. In the diagonal regime $\langle K(t)\rangle \simeq t$, and beyond the Heisenberg time $t_{\mathrm{H}} = q^L$ we have $\langle K(t)\rangle \simeq q^L$.

show that an average over just one of L gates $U_{x,x+1}$ is enough to dramatically suppress fluctuations of the SFF.

2.3 Breakdown of the diagonal approximation

In Fig. 2.4 we show $\langle K(t)\rangle$ for Haar-RFCs with $q = 2$, various L, and both periodic and open boundary conditions. In this section we show that the observed deviations from RMT are not captured by the diagonal approximation. The diagonal propagator for brickwork models takes the form

$$\mathcal{P}_{ab} = \sum_{cc^*} (W_2)_{ac}(W_1)_{cb}(W_2^*)_{ac^*}(W_1^*)_{c^*b}, \tag{2.10}$$

where all subscripts are many-body indices (taking q^L values). Each independent gate $U_{x,x+1}$ appears once in $\mathcal{P}$, as does its conjugate. $\langle\mathcal{P}\rangle$ is given by averaging over the gates. For example, the average over the gate $U_{0,1}$ acting on sites 0 and 1 in the first half-step W_1 is

$$\langle [U_{0,1}]_{c_0c_1,b_0b_1}[U_{0,1}^*]_{c_0^*c_1^*,b_0b_1}\rangle = \frac{1}{q^2}\delta_{c_0c_0^*}\delta_{c_1c_1^*}, \tag{2.11}$$

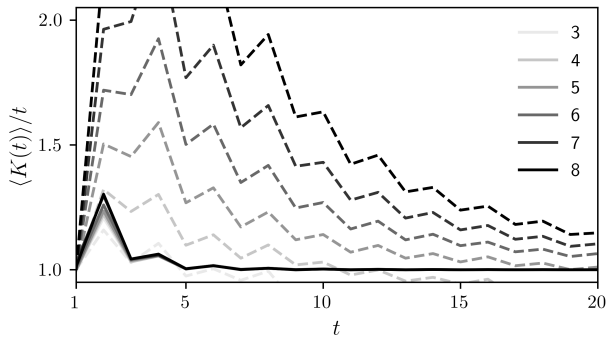

Figure 2.5: Comparison of the deviations of $\mathrm{Tr}\langle\mathcal{P}^t\rangle$ (solid) and $\langle K(t)\rangle/t$ (dashed) from unity in Haar-RFCs with open boundary conditions. The legend shows L.

where we have made single-site indices explicit. The result is the same for gates acting in the second half-step. Multiplying the expressions Eq. (2.11) for each independent gate, and summing over the internal c, c^* indices, we find the average propagator

$$\langle\mathcal{P}_{a_0\ldots a_{L-1},b_0\ldots b_{L-1}}\rangle = \frac{1}{q^L}, \tag{2.12}$$

a matrix with constant entries. The leading eigenvalue of $\langle\mathcal{P}\rangle$ is unity and all others are zero, so the diagonal approximation to the SFF is $\langle K(t)\rangle = t$ as in RMT. This is also the result at large q [34]. By contrast, in Fig. 2.4 there are obvious deviations of the SFF from RMT. These deviations grow with increasing system size, and furthermore are significantly larger with open boundary conditions than with periodic.

As indicated below Eq. (2.6) a full exploration of the diagonal approximation requires a discussion not only of $\langle\mathcal{P}\rangle^t$ but also of $\langle\mathcal{P}^t\rangle$. We now discuss this aspect in the context of Haar-RFCs. In this case, as we have shown following Eq. (2.12), the average $\langle\mathcal{P}\rangle$ has a single eigenvalue of unity, with all subleading eigenvalues zero. Individual realisations, however, typically have non-zero subleading eigenvalues which contribute to $\langle\mathcal{P}^t\rangle$. We probe the consequences of this by numerically evaluating the SFF using the approximation $\langle K(t)\rangle \approx t\mathrm{Tr}\langle\mathcal{P}^t\rangle$. In Fig. 2.5 we compare $\mathrm{Tr}\langle\mathcal{P}^t\rangle$ with $\langle K(t)\rangle/t$, and our results demonstrate that corrections to RMT arising from the subleading eigenvalues of $\mathcal{P}$ cannot account for the behaviour of Haar-RFCs.

2.4 Construction of the transfer matrix

The diagonal approximation to sums over pairs of orbits is blind to locality. In this section and the next we demonstrate how the picture of paired orbits must be extended in one-dimensional Floquet models with local interactions. In Sec. 2.4.1 we discuss the RPM, where at large q an exact treatment is possible. This reveals the picture of local orbit pairing. Motivated by this picture, in Sec. 2.4.2 we express the SFF of a brickwork model (with arbitrary q) in terms of spatial transfer matrices that act on pairs of local orbits. Through the average transfer matrix, which we discuss in Sec. 2.4.3, the picture of local orbit pairing emerges in a generic setting.

2.4.1 Random phase model

Consider first the model Eq. (2.3) in the case where the L sites are decoupled ($\varepsilon = 0$). Each site then evolves under an independent $q \times q$ Haar-random unitary matrix u_x, and the SFF is the product of those for the individual sites. From Eq. (1.4) its average $\langle K(t)\rangle = t^L$ for $1 \leq t \leq q$ and $\langle K(t)\rangle = q^L$ for $t \geq q$. On the other hand, for $\varepsilon \neq 0$ and in the ergodic phase, at late times $t \leq q^L$ we expect $\langle K(t)\rangle \simeq t$. Because the interactions are local, it is natural to expect that at early times the system will behave as if it were constructed from a number of independent subregions, so that $\langle K(t)\rangle \gg t$.

An analytic treatment of the model for $\varepsilon \neq 0$ is straightforward in the limit of large q. In calculating $\langle K(t)\rangle$ we must average each of the $q \times q$ gates u_x. Each appears t times in $\mathrm{Tr}W(t)$, and its conjugate appears t times in $\mathrm{Tr}W^*(t)$. Averaging u_x at finite q one finds a sum over $(t!)^2$ terms from Eq. (1.3), but at large q only t contribute to $\langle K(t)\rangle$, and these correspond to the t diagonal pairings of local orbits [c.f. Eq. (1.7)]. We denote these pairings by $s_x = 0 \ldots (t-1)$ at the site x; the average promotes the orbit pairing to a local degree of freedom.

The average SFF $\langle K(t)\rangle$ is then a sum over the orbit pairings s_x at each site $x = 0 \ldots (L-1)$, and takes the form of a classical partition function [109],

$$\langle K(t)\rangle = \sum_{s_0 \ldots s_{L-1}=0}^{t-1} \prod_{x=0}^{L-1} \left[\delta_{s_x s_{x+1}} + (1 - \delta_{s_x s_{x+1}}) e^{-\varepsilon t}\right]. \tag{2.13}$$

The right-hand side of Eq. (2.13) is a product of $t \times t$ transfer matrices, which are the same for each bond. We will refer to a configuration $s_x \neq s_{x+1}$ as a domain wall. The statistical weights of these domain walls are suppressed by factors $e^{-\varepsilon t}$, so the coupling strength ε appears here as the domain-wall line tension. At late times the domain walls are suppressed and we recover the RMT result $\langle K(t)\rangle = t$, corresponding to a sum over t global diagonal orbit pairings.

An interesting feature of Eq. (2.13) is the effect of the boundary conditions. The first corrections to RMT with open boundary conditions come from configurations with one domain wall,

$$\langle K(t)\rangle = t + t(t-1)(L-1)e^{-\varepsilon t} + \dots, \tag{2.14}$$

whereas with periodic boundary conditions they come from configurations with two domain walls,

$$\langle K(t)\rangle = t + \frac{1}{2}t(t-1)L(L-1)e^{-2\varepsilon t} + \dots \tag{2.15}$$

Here the factors $t(t-1)$ come from the orbit-pairing freedom in each of the two domains. With open boundary conditions $(L-1)$ is the translational entropy of one domain wall, and with periodic $\frac{1}{2}L(L-1)$ is the translational entropy of two domain walls. It is clear that with open boundary conditions, where it is possible to have just one domain wall with weight $e^{-\varepsilon t}$, rather than $e^{-2\varepsilon t}$ for two domain walls, the deviations of $\langle K(t)\rangle$ from RMT are larger.

Although Eq. (2.13) was derived in the limit of large q, in Sec. 2.5 we show that the picture of local orbit pairing is more general. For example, it describes the spectral statistics of Haar-RFCs at small q. Indeed, the deviations from RMT displayed in Fig. 2.4, including their dependence on both the system size and on the boundary conditions, illustrate the phenomenology of domain walls in the orbit pairing. Specifically, for fixed t the deviations from RMT behaviour grow with L and are larger with open than with periodic conditions. In Secs. 2.4.2 and 2.4.3 we show how to construct the transfer matrices generating the average SFF of a brickwork model.

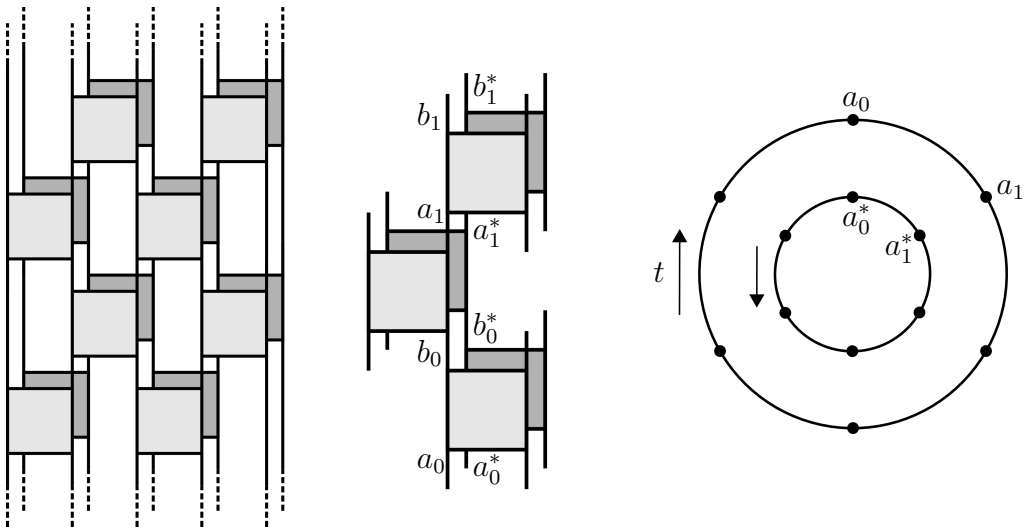

Figure 2.6: Circuit diagram for the SFF of a brickwork model, with time t running vertically and space horizontally. Left: $K(t)$ with $t = 2$, and for $L = 5$ sites with open boundary conditions. The foreground (light) shows $\mathrm{Tr}W(t)$ and the background (dark) its complex conjugate. Dashed lines exiting at the top of the figure are connected to those entering from below, giving independent traces $\mathrm{Tr}W(t)$ and $\mathrm{Tr}W^*(t)$. Centre: segment of the doubled time evolution, highlighting notation for forward $(a_0 b_0 \ldots)$ and backward $(a_0^* b_0^* \ldots)$ single-site orbits. Right: illustration of a pair of single-site orbits [c.f. many-body orbits in Fig. 2.1].

2.4.2 Brickwork models

Throughout this section we work with single-site orbits, and so here introduce some notation. Two unitary gates act on each site during a time step, so at time t each single-site orbit is a string of $2t$ integers, each taking a value $0 \ldots (q-1)$. In contrast with Sec. 2.2.1, here we denote the single-site (as opposed to many-body) forward orbits appearing in $\mathrm{Tr}W(t)$ by $(a_0 b_0 \ldots a_{t-1} b_{t-1})$. For integer r, a_r represents the state of the site at time r, and b_r represents the state of the site at time $(r + 1/2)$, in the middle of the step. We denote the backward orbits appearing in $\mathrm{Tr}W^*(t)$ by strings $(a_0^* b_0^* \ldots a_{t-1}^* b_{t-1}^*)$. In Fig. 2.6 we illustrate the SFF of a brickwork model, as well as a pair of forward and backward single-site orbits.

Consider now a unitary gate $U_{x,x+1}$ acting on sites $(x, x+1)$ in the first half of the Floquet step, so with x even. This matrix evolves the state of the two sites from a time r to $(r + \frac{1}{2})$, with r integer. We can also think of $U_{x,x+1}$ as a non-unitary matrix acting on the orbit of site $(x+1)$ at the times $(r, r + \frac{1}{2})$, and we refer to this matrix as $\tilde{U}_{x,x+1}$. Writing the components of $U_{x,x+1}$ as $[U_{x,x+1}]_{b_r b'_r, a_r a'_r}$, where

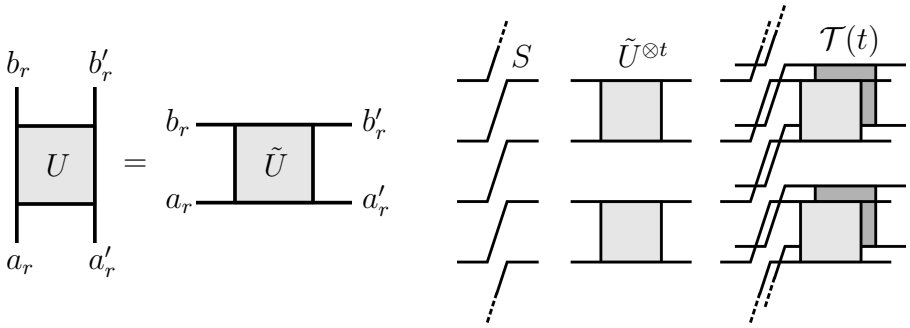

Figure 2.7: Left: components $U_{b_r b'_r, a_r a'_r}$ of the $q^2 \times q^2$ unitary matrix U, and components $\tilde{U}_{a_r b_r, a'_r b'_r}$ of the $q^2 \times q^2$ non-unitary matrix $\tilde{U}$. Time runs vertically and space horizontally. Here U acts in the first half-step of the Floquet operator, so it describes the evolution of a pair of sites $(x, x+1)$ from time step r to $(r + \frac{1}{2})$, with r integer. $\tilde{U}$ acts on the state of site $(x+1)$ at times $(r, r+\frac{1}{2})$. Right: construction of the transfer matrix generating $K(t) = |\mathrm{Tr}W(t)|^2$, here for $t = 2$. Dashed lines exiting above and entering below are connected. We show the orthogonal matrix S, the tensor product of identical $\tilde{U}$ matrices, $\tilde{U}^{\otimes t}$, and the transfer matrix $\mathcal{T}(t) = [S\tilde{U}^{\otimes t}] \otimes [S\tilde{U}^{\otimes t}]^*$, with $S\tilde{U}^{\otimes t}$ light and $[S\tilde{U}^{\otimes t}]^*$ dark.

unprimed indices a_r, b_r correspond to site x and primed a'_r, b'_r to site $(x+1)$, the components of $\tilde{U}_{x,x+1}$ are $[\tilde{U}_{x,x+1}]_{a_r b_r, a'_r b'_r} = [U_{x,x+1}]_{b_r b'_r, a_r a'_r}$, as illustrated in Fig. 2.7.

In $\mathrm{Tr}W(t)$ each gate $U_{x,x+1}$ appears t times. By taking a tensor product of the t copies of $\tilde{U}_{x,x+1}$ we create a $q^{2t} \times q^{2t}$ matrix $\tilde{U}^{\otimes t}_{x,x+1}$ acting on the entire forward orbit of site $(x+1)$. These orbits can be represented by vectors $|a_0 b_0 \dots a_{t-1} b_{t-1}\rangle$. To construct $\mathrm{Tr}W(t)$ from the standard matrix multiplication of operators with this structure, we introduce an orthogonal matrix S that acts on orbits as a translation of one half-step in time,

$$S\,|a_0 b_0 \dots a_{t-1} b_{t-1}\rangle = |b_0 a_1 \dots b_{t-1} a_0\rangle\,. \tag{2.16}$$

The matrices S and $\tilde{U}^{\otimes t}$ are illustrated in Fig. 2.7. With periodic boundary conditions

$$\mathrm{Tr}W(t) = \mathrm{tr}\Big[\tilde{U}^{\otimes t}_{0,1} S \tilde{U}^{\otimes t}_{1,2} S^{-1} \dots S U^{\otimes t}_{L-1,0} S^{-1}\Big], \tag{2.17}$$

where $S^{-1} = S^{\mathrm{T}}$, and L is the number of sites, which is necessarily even with these boundary conditions. Here tr is a trace over single-site orbits, to be distinguished from Tr, a trace over many-body states. Since the evolution operator is periodic we have $[S^2, \tilde{U}^{\otimes t}] = 0$, where S^2 translates an orbit by one full step in time. Clearly

$S^{2t} = \mathbb{1}$, where $\mathbb{1}$ is the $q^{2t} \times q^{2t}$ identity acting in the space of single-site orbits. Using these properties we can write $\mathrm{Tr}W(t)$ in terms of one type of transfer matrix, $S\tilde{U}^{\otimes t}_{x,x+1}$,

$$\mathrm{Tr}W(t) = \mathrm{tr}[S\tilde{U}^{\otimes t}_{0,1} \dots S\tilde{U}^{\otimes t}_{L-1,0} S^{-L}]. \tag{2.18}$$

We can write down a similar expression with open boundary conditions,

$$\mathrm{Tr}W(t) = \langle B| \, S^{-1} S\tilde{U}^{\otimes t}_{0,1} \dots S\tilde{U}^{\otimes t}_{L-2,L-1} \, |B\rangle \,, \tag{2.19}$$

where the boundary state $|B\rangle$ has components

$$\langle a_0 b_0 \dots a_{t-1} b_{t-1} | B \rangle = \prod_{r=0}^{t-1} \delta_{b_r a_{r+1}}, \tag{2.20}$$

and is invariant under time translation by a full step, $S^2 \, |B\rangle = |B\rangle$.

The transfer matrices that generate the SFF $K(t) = |\mathrm{Tr}W(t)|^2$ are straightforwardly expressed as tensor products of the transfer matrices that generate $\mathrm{Tr}W(t)$ and $\mathrm{Tr}W^*(t)$. It is convenient to define

$$\mathcal{S} \equiv S \otimes S, \quad \mathcal{R}_{x,x+1}(t) \equiv \tilde{U}^{\otimes t}_{x,x+1} \otimes [\tilde{U}^{\otimes t}_{x,x+1}]^*, \tag{2.21}$$

so that the transfer matrices generating the SFF have the form

$$\mathcal{T}_{x,x+1}(t) = \mathcal{S}\mathcal{R}_{x,x+1}(t). \tag{2.22}$$

These objects act on the product space of forward and backward orbits at site $(x+1)$, which has dimension q^{4t}. They are illustrated in Fig. 2.7.

The matrices $\mathcal{T}_{x,x+1}(t)$ have symmetries associated with translation in the time direction [see Ref. [115] for a related treatment in the context of the kicked Ising model]. In particular, they commute with the full-step time-translation operators for both forward and backward orbits

$$[S^2 \otimes \mathbb{1}, \mathcal{T}_{x,x+1}(t)] = [\mathbb{1} \otimes S^2, \mathcal{T}_{x,x+1}(t)] = 0. \tag{2.23}$$

Since $(S^2)^t = \mathbb{1}$, $\mathcal{T}_{x,x+1}$ can be block-diagonalised into t^2 sectors, having eigenvalues $e^{2\pi i \nu_+/t}$ under $S^2 \otimes \mathbb{1}$ and $e^{2\pi i \nu_-/t}$ under $\mathbb{1} \otimes S^2$, where $\nu_+, \nu_- = 0, 1, \dots, (t-1)$ are defined modulo t. The transfer matrices for each bond $(x, x+1)$ are different. Our focus, however, is on the full ensemble average. Following such an average all the transfer matrices are the same.

2.4.3 Disorder average

The notion of orbit pairing takes on a concrete meaning in the ensemble average of the SFF. For identically and independently distributed gates, $\langle K(t)\rangle$ is determined by powers of the averaged transfer matrix $\langle \mathcal{T}(t)\rangle$, which from here on will be at the centre of our discussion.

To calculate $\langle \mathcal{T}(t)\rangle$ we must Haar-average the tensor product $\mathcal{R}(t) = \tilde{U}^{\otimes t} \otimes [\tilde{U}^{\otimes t}]^*$. Writing the first indices of $\tilde{U}^{\otimes t}$ and $[\tilde{U}^{\otimes t}]^*$ as orbits $(a_0 b_0 \ldots)$ and $(a_0^* b_0^* \ldots)$, respectively, the only non-vanishing matrix elements of their average tensor product have $a_r = a^*_{\sigma(r)}$ and $b_r = b^*_{\tau(r)}$, for $r = 0 \ldots (t-1)$, where σ and τ denote permutations of t objects [see Eq. (1.3)]. The same is true of the second indices. To arrive at a succinct expression for the average transfer matrix it is convenient to introduce vectors $|\sigma, \tau\rangle$, in the product space of forward and backward orbits, which have nonzero entries only where indices are paired in this way:

$$\langle a_0 b_0 \ldots; a_0^* b_0^* \ldots | \sigma, \tau \rangle = \prod_{r=0}^{t-1} \delta_{a_r a^*_{\sigma(r)}} \delta_{b_r b^*_{\tau(r)}}. \tag{2.24}$$

Note that the vectors $|\sigma, \tau\rangle$ are neither normalised nor orthogonal. The average of $\tilde{U}^{\otimes t} \otimes [\tilde{U}^{\otimes t}]^*$ can be expressed in terms of the vectors $|\sigma, \tau\rangle$ and the (q^2-dependent) Weingarten functions $\mathrm{Wg}(\sigma\tau^{-1})$ using Eq. (1.3),

$$\langle \mathcal{R}(t)\rangle = \sum_{\sigma\tau} \mathrm{Wg}(\sigma\tau^{-1}) \, |\sigma, \tau\rangle \langle \sigma, \tau| \,, \quad \langle \mathcal{T}(t)\rangle = \mathcal{S}\langle \mathcal{R}(t)\rangle. \tag{2.25}$$

Here the sum is over all pairs of permutations of t objects. Only t terms in the sum in Eq. (2.25) contribute to $\langle K(t)\rangle$ in the large-q limit, and these correspond to local diagonal orbit pairings as in Sec. 2.4.1. We elaborate on this in A.4.

As discussed above, the transfer matrices have a block structure associated with symmetry under time translation. Focusing on the average $\langle \mathcal{T}(t)\rangle$, we write the left and right eigenvectors in the block ν_+, ν_- as $\langle \nu_+ \nu_- \alpha_L; t|$ and $|\nu_+ \nu_- \alpha_R; t\rangle$, respectively, and the corresponding eigenvalues as $\lambda(\nu_+ \nu_- \alpha; t)$. Here $\alpha_{L,R} = 0, 1, \ldots$ label eigenstates in descending order of magnitude, so $\lambda(\nu_+ \nu_-, 0; t)$ is the leading

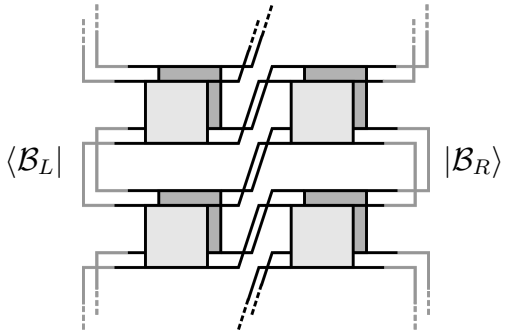

Figure 2.8: SFF with open boundary conditions in terms of the transfer matrices $\mathcal{T}_{x,x+1}(t)$. Here $t = 2$ and $L = 3$ so $K(t) = \langle \mathcal{B}_L | \mathcal{T}_{0,1}\mathcal{T}_{1,2} | \mathcal{B}_R \rangle$. The vectors $|\mathcal{B}_{L,R}\rangle$, encoding the boundary conditions, are shown as grey lines.

eigenvalue in the block ν_+, ν_-. The spectral decomposition of the average transfer matrix $\langle \mathcal{T}(t) \rangle$ is then

$$\langle \mathcal{T}(t) \rangle = \sum_{\nu_+,\nu_-=0}^{t-1} \sum_{\alpha} \lambda(\nu_+\nu_-\alpha; t) \, |\nu_+\nu_-\alpha_R; t\rangle \, \langle \nu_+\nu_-\alpha_L; t| \,, \tag{2.26}$$

where the eigenvectors are biorthogonal $\langle \nu_+\nu_-\alpha_L; t | \nu'_+\nu'_-\alpha'_R; t \rangle = \delta_{\nu_+\nu'_+} \delta_{\nu_-\nu'_-} \delta_{\alpha_L\alpha'_R}$.

We are now in a position to write down expressions for the average SFF in terms of the spectral properties of the average transfer matrix. With periodic boundary conditions, where L is necessarily even,

$$\langle K(t) \rangle = \mathrm{tr}[\langle \mathcal{T}(t) \rangle^L \mathcal{S}^{-L}] = \sum_{\nu_+\nu_-\alpha} [\lambda(\nu_+\nu_-\alpha; t)]^L e^{-2\pi i (L/2)(\nu_+ + \nu_-)/t}. \tag{2.27}$$

For the case of open boundary conditions we define the doubled boundary vectors $|\mathcal{B}_R\rangle \equiv |B\rangle \otimes |B\rangle$ and $\langle \mathcal{B}_L| \equiv \langle \mathcal{B}_R| \, \mathcal{S}$, for the right and left ends of the chain, respectively. These vectors are in the $\nu_+ = \nu_- = 0$ sector. From Eq. (2.19) we then have

$$\begin{aligned} \langle K(t) \rangle &= \langle \mathcal{B}_L | \, \langle \mathcal{T}(t) \rangle^{L-1} \, | \mathcal{B}_R \rangle \,, \\ &= \sum_{\alpha} [\lambda(0, 0, \alpha; t)]^{L-1} \, \langle \mathcal{B}_L | 0, 0, \alpha_R; t \rangle \, \langle 0, 0, \alpha_L; t | \mathcal{B}_R \rangle \,, \end{aligned} \tag{2.28}$$

and this is illustrated in Fig. 2.8.

An immediate question is how, for general L, RMT level statistics emerge from the average transfer matrix $\langle \mathcal{T}(t) \rangle$ at late times. We anticipate that in the diagonal regime the result $\langle K(t) \rangle = t$ is expressible as a sum over the t global diagonal orbit pairings, each contributing unity. In the language of the average transfer matrix $\langle \mathcal{T}(t) \rangle$ this corresponds to having t leading eigenvalues which at late times approach unity. Different behaviour sets in beyond $t_{\mathrm{H}} = q^L$, where the average SFF plateaus at $\langle K(t) \rangle = q^L$. To see how this behaviour could arise, note that the number of

nonzero subleading eigenvalues of $\langle \mathcal{T}(t) \rangle$ grows very rapidly with t, but that the contributions of these eigenvalues to the SFF are suppressed for large L. In Sec. 2.6 we show, based on exact diagonalisation of $\langle \mathcal{T}(t) \rangle$ for $t \leq 5$, that the proliferation of subleading eigenvalues with increasing t is responsible for the plateau.

Our analysis is focused on the regime $1 \ll t \ll t_{\mathrm{H}}$ for large L, and therefore on the late-time behaviour of the t leading eigenvalues of $\langle \mathcal{T}(t) \rangle$. General features then emerge because the only microscopic timescale in $\langle \mathcal{T}(t) \rangle$ is q^2, the Heisenberg time for a single gate. We will see that each of the sectors $\nu = \nu_+ = -\nu_-$ contains one of the t leading eigenvalues. Since our attention is effectively limited to these and the corresponding eigenvectors, it is convenient to introduce the shorthand notation

$$\begin{aligned} \lambda(\nu, t) &\equiv \lambda(\nu, -\nu, 0; t) \\ |\nu, t; R\rangle &\equiv |\nu, -\nu, 0_R; t\rangle \\ \langle \nu, t; L| &\equiv \langle \nu, -\nu, 0_L; t| \,. \end{aligned} \tag{2.29}$$

Then, for example, when we refer to the $\nu = 1$ sector this means $\nu_+ = 1$, $\nu_- = -1$. Note that there is a simple relation between the left and right eigenvectors in these sectors, which follows from the fact that they are invariant under $\mathcal{S}^2$. From their definition,

$$\mathcal{S}\langle \mathcal{R}(t) \rangle \, |\nu, t; R\rangle = \lambda(\nu, t) \, |\nu, t; R\rangle \,, \quad \langle \nu, t; L| \, \mathcal{S}\langle \mathcal{R}(t) \rangle = \lambda(\nu, t) \, \langle \nu, t; L| \,, \tag{2.30}$$

where $\langle \mathcal{R}(t) \rangle$ is real and symmetric. Taking the Hermitian conjugate of the second equation, and then multiplying on the left by $\mathcal{S}$, we find

$$\mathcal{S}\langle \mathcal{R}(t) \rangle \mathcal{S} |\nu, t; L\rangle = \lambda^*(\nu, t) \mathcal{S} |\nu, t; L\rangle, \tag{2.31}$$

where we have used $\mathcal{S}^{-1}|\nu, t; L\rangle = \mathcal{S}|\nu, t; L\rangle$. Within each of the sectors ν we will see that the leading eigenvalue $\lambda(\nu, t)$ is real and non-degenerate, and consequently we must have $\mathcal{S} \, |\nu, t; L\rangle = |\nu, t; R\rangle$.

In the regime of interest the transfer matrix is too large to compute directly, so in Sec. 2.5 we study the length-scaling of the average SFF and related objects with a variety of boundary conditions. Through this we will determine $\lambda(\nu, t)$ as well as certain properties of the corresponding eigenvectors.

2.5 Spectrum of the transfer matrix

Here we develop a set of techniques that allow for the numerical investigation of the transfer matrix at late times. In Sec. 2.5.1 we show that the length-scaling of $\langle K(t)\rangle$ with open boundary conditions gives access to the leading eigenvalue in the $\nu = 0$ sector, which dominates the spectral statistics at fixed t and large L. Following this, in Sec. 2.5.2, we impose a novel kind of twisted boundary condition on the pairing of many-body orbits. By introducing domain walls in this way, we access all t leading eigenvalues. From these we will see how the result $\langle K(t)\rangle \simeq t$ emerges from the spectral properties of the transfer matrix. Then, in Sec. 2.5.3, we probe the pairing within domains and across domain walls. Sec. 2.5.4 discusses a connection between the spectral statistics and the behaviour of the system when coupled to a bath.

2.5.1 Open boundary conditions

Based on the discussion in Sec. 2.4.1 we anticipate that the leading correction to the SFF relative to RMT, in the case of open boundary conditions, can be understood in terms of a single domain wall. From this we will infer an effective domain wall tension.

If the leading eigenvalue in the $\nu = 0$ sector dominates the SFF in Eq. (2.28), we have

$$\langle K(t)\rangle = \lambda^{L-1}(0,t)\,\langle \mathcal{B}_L|0,t;R\rangle\,\langle 0,t;L|\mathcal{B}_R\rangle + \ldots, \tag{2.32}$$

where the ellipses indicate contributions from sub-leading eigenvalues. By following the L-dependence of $\langle K(t)\rangle$ for each time t we extract the leading eigenvalue $\lambda(0,t)$ and the overlap of the corresponding eigenvector with the boundary states, $\langle \mathcal{B}_L|0,t;R\rangle\,\langle 0,t;L|\mathcal{B}_R\rangle$, as illustrated in Fig. 2.9(b). In Fig. 2.9(a) we show that $\lambda(0,t)$ approaches unity from above at large t. We find also that the overlap, shown in the inset, approaches t at late times. This is exactly the value expected if the leading eigenvector of $\langle \mathcal{T}(t)\rangle$ represents a locally diagonal orbit pairing, as we discuss in Sec. 2.5.3.

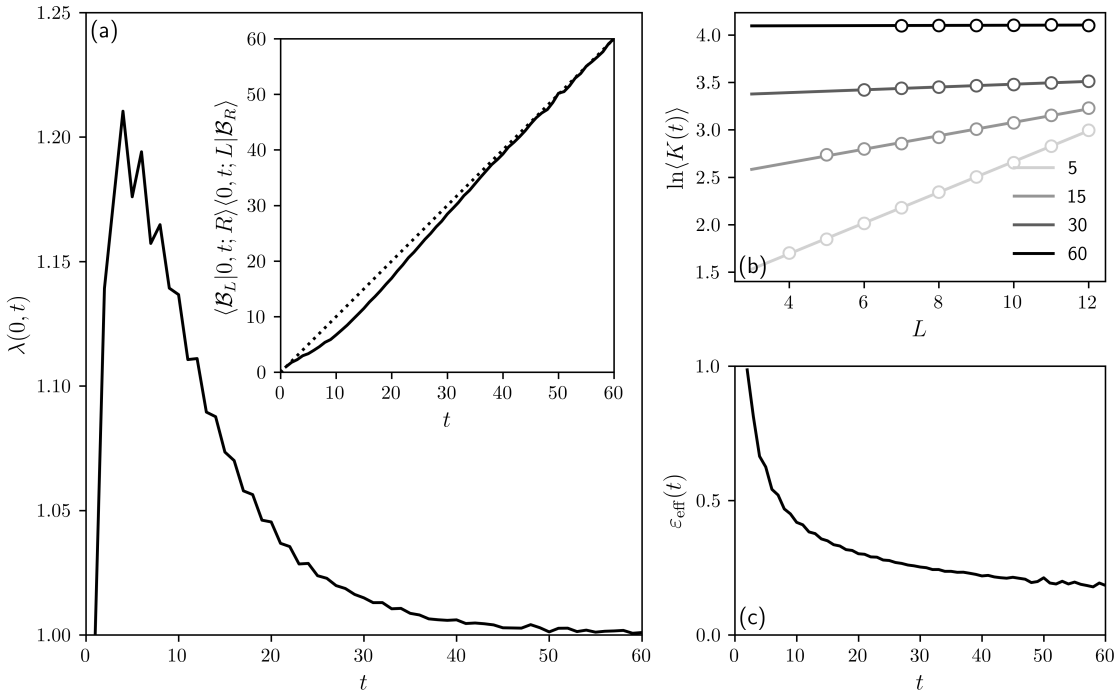

Figure 2.9: (a) Leading eigenvalue $\lambda(0,t)$ of $\langle \mathcal{T}(t)\rangle$. Inset: overlap (solid) of the corresponding eigenvectors with the boundary states $|\mathcal{B}_{L,R}\rangle$, which approaches t (dotted) at late times. (b) $\ln\langle K(t)\rangle$ versus L for various t (legend), used to extract data in (a). (c) Effective tension $\varepsilon_{\rm eff}(t)$ [Eq. (2.34)] calculated from $\lambda(0,t)$ in (a).

Expanding the average SFF around the RMT result, at large t we then have

$$\langle K(t)\rangle = t + t(L-1)\delta\lambda(0,t) + \ldots, \tag{2.33}$$

where $\delta\lambda(0,t) \equiv \lambda(0,t) - 1$. We can interpret the deviation from RMT as a domain wall contribution in analogy with Eq. (2.14). Here $(L-1)$ is the translational entropy, and $\delta\lambda(0,t)$ in Eq. (2.33) plays the role of $(t-1)e^{-\varepsilon t}$, the sum of statistical weights of the $(t-1)$ different domain walls. This motivates the definition of an effective domain wall tension $\varepsilon_{\rm eff} = \varepsilon_{\rm eff}(t)$ via

$$e^{-\varepsilon_{\rm eff}(t)t} = \frac{\delta\lambda(0,t)}{t-1}. \tag{2.34}$$

In the model of Ref. [109] all domain walls have the same tension ε, so there $\varepsilon_{\rm eff} = \varepsilon$, which is also time-independent. This is not the case in general. We show in Fig. 2.9(c) that the effective domain wall tension in the $q = 2$ Haar-RFC decreases with time. To understand this, suppose that a domain wall can be located on a particular bond with corresponding gate U, and that we can associate a tension

$\varepsilon(U)$ with this gate. The average of the statistical weight $e^{-\varepsilon(U)t}$ over U is at late times increasingly dominated by those gates with small $\varepsilon(U)$, and consequently it is natural for the effective tension derived from this average to decrease with time.

We can relate this behaviour to the Thouless time $t_{\rm Th}$ as follows. From Eqs. (2.33) and (2.34) we see that the crossover to RMT occurs when the decreasing statistical weight $e^{-\varepsilon_{\rm eff}(t)t}$ associated with a domain wall overwhelms the translational entropy $(L-1)$. If the effective domain wall tension approaches a nonzero constant $\varepsilon_{\rm eff}(\infty)$ at late times, the timescale for the crossover of the SFF to RMT behaviour is $t_{\rm Th} = \ln L/\varepsilon_{\rm eff}(\infty)$.

In this section we have determined one of the t leading eigenvalues of the average transfer matrix. Next we will determine the other $(t-1)$ and provide further evidence for domain walls in the orbit pairing.

2.5.2 Twisted boundary conditions

In order to access t different symmetry sectors of $\langle \mathcal{T}(t)\rangle$ we impose local diagonal orbit pairings at the two ends of the system. This forces a domain wall into the many-body orbit pairing, and gives us information on $\lambda(\nu,t)$, $\langle \nu,t;L|$, and $|\nu,t;R\rangle$ for all ν. By determining all of these leading eigenvalues, we will show that they alone are sufficient to reconstruct the SFF with periodic boundary conditions to a remarkable degree of accuracy.

2.5.2.1 Domain walls

The local diagonal orbit pairings are represented by vectors $|s\rangle$ in the product space of forward and backward orbits. The pairing $|s\rangle$ is a normalised member of the set of vectors $|\sigma,\tau\rangle$ introduced in Eq. (2.24), with $\sigma=\tau$ the permutation mapping $r \to (r+s)$ modulo t, for $s = 0, 1 \ldots (t-1)$. The components are

$$\langle a_0 b_0 \ldots; a_0^* b_0^* \ldots | s\rangle = \frac{1}{q^t} \prod_{r=0}^{t-1} \delta_{a_r a_{r+s}^*} \delta_{b_r b_{r+s}^*}. \tag{2.35}$$

Imposing the orbit pairing s_L on the left and s_R on the right of an L-site system we find

$$Z(s_R - s_L, t) = \langle s_L | \mathcal{T}_{0,1}(t) \ldots \mathcal{T}_{L-2,L-1}(t) | s_R\rangle\,, \tag{2.36}$$

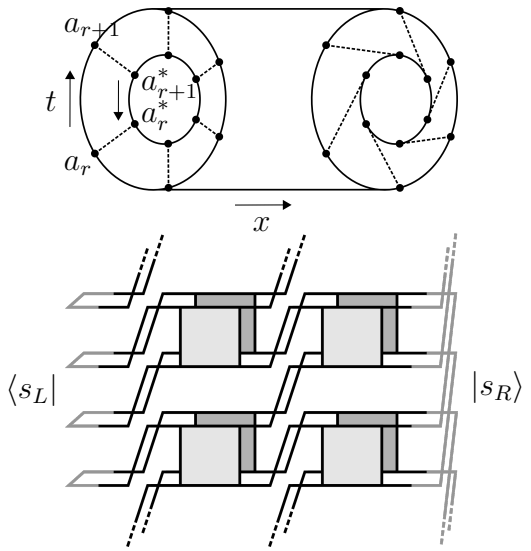

Figure 2.10: Twisted boundary conditions on a pair of forward and backward orbits, $Z(s,t)$ [Eq. (2.36)]. Here $s_L = 0$ and $s_R = 1$ so $s = s_R - s_L = 1$. Above: schematic orbit illustration as in Fig. 2.1. Below: circuit diagram, for $t = 2$ and $L = 3$, showing transfer matrices $\mathcal{T}_{x,x+1}(t)$. Here $Z(1,2) = \langle s_L = 0|\,\mathcal{T}_{0,1}(2)\mathcal{T}_{1,2}(2)\,|s_R = 1\rangle$. Vectors $\langle s_L|$ and $|s_R\rangle$ are represented by grey lines.

which is illustrated in Fig. 2.10. For $s_L = s_R$ we force equal-time pairings, and for $s_L \neq s_R$ we force a domain wall into the orbit pairing.

In practice we impose these boundary conditions using a Monte-Carlo method. This involves punctuating the forward and backward orbits contributing to $\mathrm{Tr}W(t)$ and its conjugate, respectively, with additional single-site Haar-random unitary matrices at the boundary. These are arranged in such a way that averaging over them forces particular local pairings of the forward and backward orbits. Importantly, they are independent for different time steps. We illustrate this construction in Fig. 2.11. To avoid storing multiple copies of the evolution operator, which is memory intensive, for a given set of boundary matrices we compute the traces depicted in the foreground and background of Fig. 2.11 independently. Each such trace is a complex scalar. Computing their product, and performing a Monte-Carlo average of this quantity over the boundary matrices, we find $Z(s,t)$.

Averaging $Z(s,t)$ over the ensemble of Floquet operators W, we find

$$\langle Z(s,t)\rangle = \langle 0|\langle \mathcal{T}(t)\rangle^{L-1}|s\rangle\,, \tag{2.37}$$

and through this we will probe the average transfer matrix $\langle \mathcal{T}(t)\rangle$. First, supposing that the RMT behaviour $\langle K(t)\rangle = t$ at late times arises from a sum over t global diagonal orbit pairings, we can ask what this implies for $\langle Z(s,t)\rangle$, and hence $\langle \mathcal{T}(t)\rangle$. The boundary conditions imposed for $Z(0,t)$ are compatible with one of these

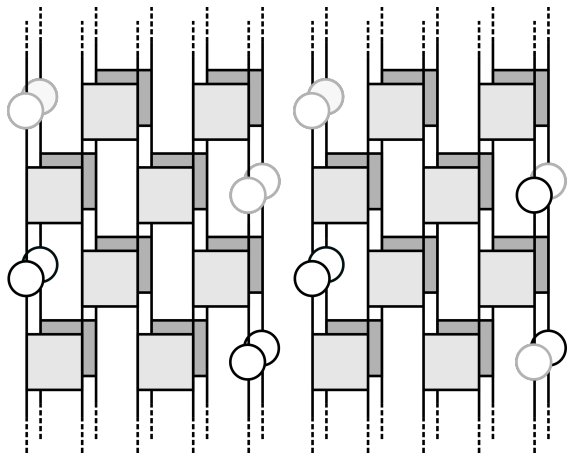

Figure 2.11: Single-site Haar-random matrices (open circles), whose average imposes pairings of forward and backward paths to give $Z(s,t)$ [Eq. (2.36)] with $t = 2$. Grey and black circles represent independent matrices, and matrices on the left- and the right-hand sites are independent. Other conventions as in Fig. 2.6. In the left-hand diagram the average fixes $s_L = 0$ and $s_R = 0$, giving $Z(0,2)$. In the right-hand diagram the average fixes $s_L = 0$ and $s_R = 1$, giving $Z(1,2)$ as in Fig. 2.10.

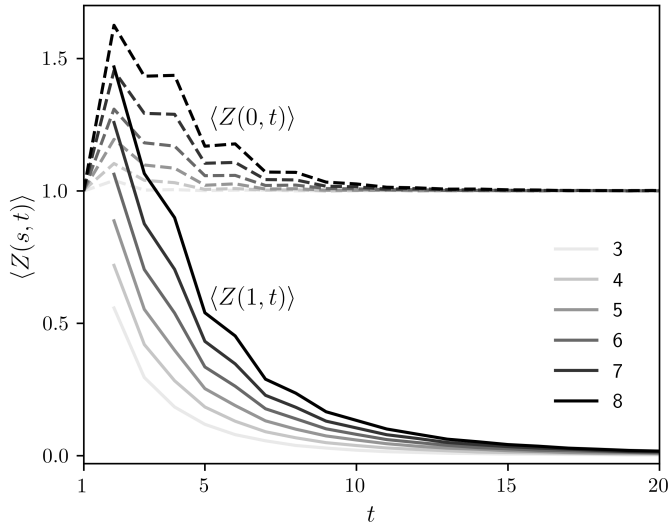

Figure 2.12: Twisted boundary conditions: $\langle Z(s,t)\rangle$ [Eq. (2.37)] with L on the legend. For $s = 1$ (solid) the boundary conditions force a domain wall into the pairing of local orbits, whereas for $s = 0$ (dashed) they do not.

pairings, whereas those for $Z(s \neq 0, t)$ are not compatible with any of them. We therefore expect that $\langle Z(0,t)\rangle \to 1$ and $\langle Z(s \neq 0, t)\rangle \to 0$ with increasing t, on the grounds that contributions from pairs of many-body orbits with domain walls should vanish at late times. We show that this is indeed the case in Fig. 2.12 for $s = 0$ and $s = 1$ for various L, and in Fig. 2.13(a) for $L = 8$ and various s [see also Sec. 2.5.4]. Making a connection with the RPM at large q, there we find $\langle Z(s \neq 0, t)\rangle \simeq (L-1)e^{-\varepsilon t}$ at late times, where $(L-1)$ is the translational entropy of the domain wall. The observed increase of $\langle Z(s,t)\rangle$ with L in Fig. 2.12 is then understood as a consequence of this entropy, and further demonstrates the failure of the diagonal approximation. In principle, and in contrast to Ref. [109], we expect the decay rate of $\langle Z(s \neq 0, t)\rangle$ to depend on s. Behaviour of this kind is evident in Fig. 2.13(a) [see also A.4].

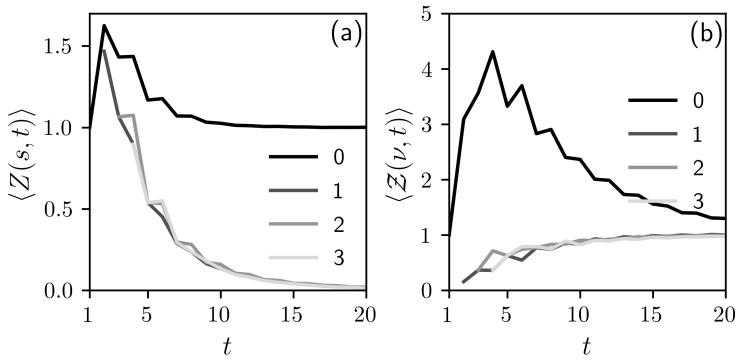

Figure 2.13: (a) $\langle Z(s,t)\rangle$, with s on the legend. $\langle Z(0,t)\rangle$ tends to unity and $\langle Z(s\neq 0,t)\rangle$ decays approximately exponentially. (b) $\langle \mathcal{Z}(\nu,t)\rangle$, with ν on the legend, defined as the Fourier components of $\langle Z(s,t)\rangle$ with respect to s in Eq. (2.39). Here $L=8$.

2.5.2.2 Leading eigenvalues

Using our numerics on $\langle Z(s,t)\rangle$ we can extract the leading eigenvalues $\lambda(\nu,t)$. The local diagonal pairings $|s\rangle$ defined in Eq. (2.35) are eigenvectors of $\mathcal{S}^2$ with unit eigenvalue, so they are linear combinations of vectors in sectors with $\nu_+ = -\nu_-$. We define their Fourier transform in sector $\nu=\nu_+=-\nu_-$ as

$$|\nu\rangle = \frac{1}{\sqrt{t}}\sum_{s=0}^{t-1} e^{-2\pi i\nu s/t}\,|s\rangle\,. \tag{2.38}$$

Using Eq. (2.38) and the spectral decomposition of $\langle \mathcal{T}(t)\rangle$ in Eq. (2.26), we have the Fourier transform of $\langle Z(s,t)\rangle$,

$$\begin{aligned}\langle \mathcal{Z}(\nu,t)\rangle &= \sum_{s=0}^{t-1} e^{-2\pi i\nu s/t}\langle Z(s,t)\rangle \\ &= \sum_{\alpha}[\lambda(\nu,-\nu,\alpha;t)]^{L-1}\,\langle\nu|\nu,-\nu,\alpha_R;t\rangle\,\langle\nu,-\nu,\alpha_L;t|\nu\rangle\,.\end{aligned} \tag{2.39}$$

For fixed t and large L,

$$\langle \mathcal{Z}(\nu,t)\rangle = \lambda^{L-1}(\nu,t)\,\langle\nu|\nu,t;R\rangle\,\langle\nu,t;L|\nu\rangle + \ldots, \tag{2.40}$$

where the ellipses represent contributions from sub-leading eigenvalues.

We show $\langle \mathcal{Z}(\nu,t)\rangle$ for $L=8$ and various ν as a function of t in Fig. 2.13(b). The qualitative behaviour of the leading eigenvalues and corresponding eigenvectors at large t can be deduced as follows. First note that $\langle Z(0,t)\rangle\to 1$ and $\langle Z(s\neq 0,t)\rangle\to 0$ at large t for all L. Substituting this behaviour into the first line of Eq. (2.39), we find $\langle \mathcal{Z}(\nu,t)\rangle\to 1$ for large t, for all L and ν. From Eq. (2.40), this implies that the leading eigenvalues $\lambda(\nu,t)\simeq 1$, and the overlaps $\langle\nu|\nu,t;R\rangle\,\langle\nu,t;L|\nu\rangle\simeq 1$.

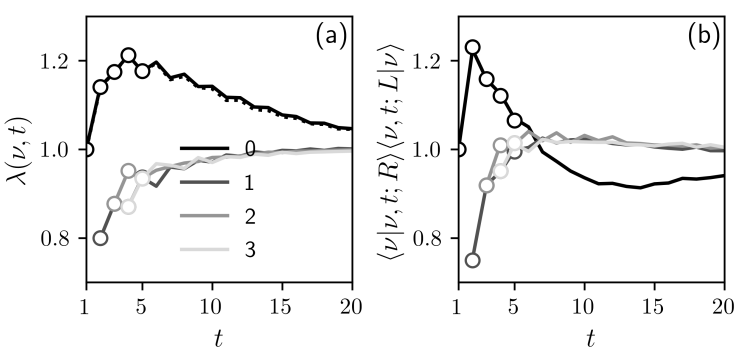

Figure 2.14: (a) $\lambda(\nu,t)$ for various ν (legend). Solid lines from length-scaling of $\langle\mathcal{Z}(\nu,t)\rangle$, dotted line $\lambda(0,t)$ from Fig. 2.9(a) for comparison, and white data points from ED of $\langle\mathcal{T}(t)\rangle$ [see Sec. 2.6]. (b) Overlaps of $\langle\mathcal{T}(t)\rangle$ eigenvectors with the paired states $|\nu\rangle$.

Moving beyond this qualitative analysis, the leading eigenvalues $\lambda(\nu,t)$ and the overlaps $\langle\nu|\nu,t;R\rangle\,\langle\nu,t;L|\nu\rangle$ can be extracted from the length-scaling of $\langle\mathcal{Z}(\nu,t)\rangle$. Aspects of this analysis are in A.3, and we show results in Fig. 2.14. For comparison we show (i) the exact results for $t\leq 5$, determined from ED of $\langle\mathcal{T}(t)\rangle$ [see Sec. 2.6], and (ii) the calculation of $\lambda(0,t)$ from Fig. 2.9, and we find excellent agreement between the different approaches. We see that $\lambda(0,t)\geq 1$ and $\lambda(\nu\neq 0,t)\leq 1$, with all t leading eigenvalues approaching unity at late times.

We can conduct a stringent test of the accuracy of the eigenvalues that we have extracted in Fig. 2.14(a), and of the adequacy of focusing on only the t leading eigenvalues. To do so we use our results to reconstruct the SFF with periodic boundary conditions. From Eq. (2.27),

$$\langle K(t)\rangle = \sum_{\nu=0}^{t-1}\lambda^L(\nu,t)+\ldots, \tag{2.41}$$

where the ellipses denote contributions from subleading eigenvalues. In Fig. 2.15 we compare the terms shown in Eq. (2.41) with $\langle K(t)\rangle$ calculated from ED of Floquet operators. Even for $L=4$ the reconstruction of $\langle K(t)\rangle$ is highly accurate for $t<q^L$. Furthermore, for fixed t, our restriction to only the leading eigenvalues of $\langle\mathcal{T}(t)\rangle$ is exact in the large-L limit. We can therefore extrapolate to arbitrarily large systems, where ED is not an option.

Within the transfer-matrix framework, the mechanisms giving rise to the RMT result $\langle K(t)\rangle = t$ in the diagonal regime are different with periodic and with open boundary conditions. In the periodic case the t leading eigenvalues each contribute

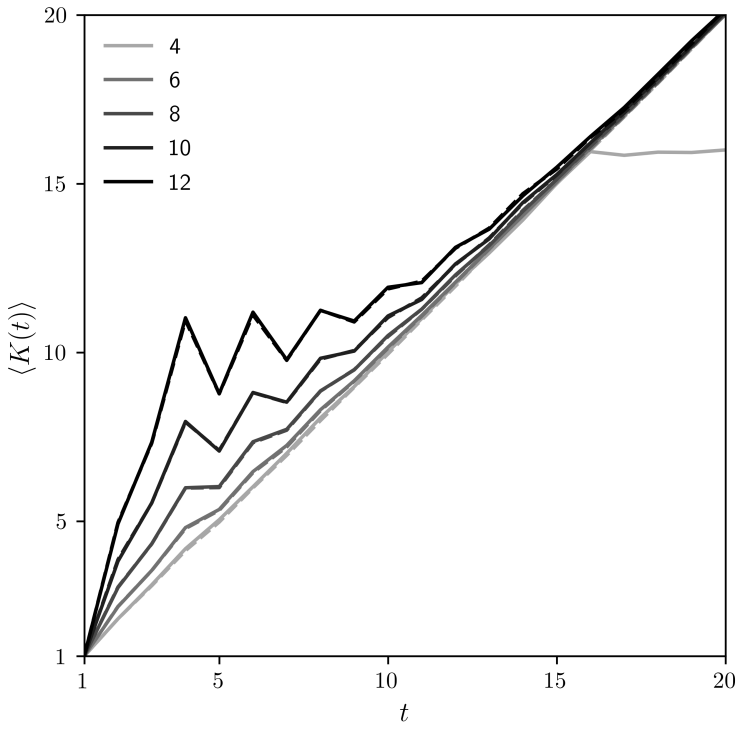

Figure 2.15: Average SFF $\langle K(t)\rangle$ with periodic boundary conditions for various L (legend), calculated using (dashed) the t leading eigenvalues $\lambda(\nu,t)$ of $\langle\mathcal{T}(t)\rangle$, from Fig. 2.14(a), and (solid) ED of Floquet operators, as in Fig. 2.4(a). The difference between the two approaches $|\sum_\nu \lambda^L(\nu,t) - \langle K(t)\rangle| < 0.1$ for all $t < t_{\mathrm{H}}$ shown.

unity. In the open case just one of these eigenvalues, in the $\nu = 0$ sector, contributes to $\langle K(t)\rangle$, but this contribution is enhanced by a factor $\langle\mathcal{B}_L|0,t;R\rangle\,\langle 0,t;L|\mathcal{B}_R\rangle \simeq t$.

2.5.2.3 Domain wall tensions

Having established the approximate equality $\langle K(t)\rangle \simeq \sum_{\nu=0}^{t-1}\lambda^L(\nu,t)$ in Fig. 2.15, we now relate the average SFF with periodic boundary conditions to properties of the domain walls studied in, for example, Fig. 2.12. At late times and for a nonzero twist s, the Fourier transform of Eq. (2.39) gives

$$\langle Z(s,t)\rangle \simeq (L-1)\times\frac{1}{t}\sum_{\nu=0}^{t-1}\delta\lambda(\nu,t)e^{2\pi i\nu s/t}+\ldots \tag{2.42}$$

Here we have written $\delta\lambda(\nu,t) = \lambda(\nu,t) - 1$ and used $\langle\nu|\nu,t;R\rangle\,\langle\nu,t;L|\nu\rangle \simeq 1$. The ellipses represent terms higher order in $\delta\lambda(\nu,t)$, as well as contributions from subleading eigenvalues. With no twist we instead have $\langle Z(0,t)\rangle \simeq 1$ from Fig. 2.12. Eq. (2.42) and the observed decay of $\langle Z(s,t)\rangle$ in Fig. 2.12 motivate the definition of the domain wall tensions $\varepsilon(s,t)$ through

$$e^{-\varepsilon(s,t)t} = \frac{1}{t}\sum_{\nu=0}^{t-1}\delta\lambda(\nu,t)e^{2\pi i\nu s/t}. \tag{2.43}$$

Since $\langle Z(s=0,t)\rangle = 1$ for large t, independently of L, we see that $\sum_{\nu=0}^{t-1} \delta\lambda(\nu,t) = 0$. The statistical weight $e^{-\varepsilon_{\rm eff}(t)t}$ defining the effective tension $\varepsilon_{\rm eff}(t)$ in Eq. (2.34) is then simply the average of the statistical weights $e^{-\varepsilon(s,t)t}$ with $s \neq 0$.

To express the SFF with periodic boundary conditions in terms of the domain wall tensions we invert Eq. (2.43) and use $\langle K(t)\rangle \simeq \sum_{\nu=0}^{t-1} \lambda^L(\nu,t)$. Expanding around the RMT result we find

$$\langle K(t)\rangle = t + \frac{1}{2}L(L-1)t\sum_{s=1}^{t-1} e^{-2\varepsilon(s,t)t} + \dots \tag{2.44}$$

to second order in $\delta\lambda(\nu,t)$. We see then that, as in the RPM [Eq. (2.15)], the first correction to RMT with periodic boundary conditions can be interpreted as arising from pairings of orbits with two domain walls, as opposed to pairings with just one domain wall as in the case of open boundary conditions [Eqs. (2.14) and (2.33)]. Note that this interpretation relies on the fact that $\sum_{\nu=0}^{t-1} \delta\lambda(\nu,t) = 0$, and so that $\langle Z(s=0,t)\rangle = 1$. We discuss this further in Sec. 2.5.4.

2.5.3 Pairing domains

Here we numerically investigate the character of the orbit-pairing domains, and of the domain walls between them. Our tools are the twisted boundary conditions from Sec. 2.5.2, and an operator in the space of orbit pairs, defined below.

Our results on the leading eigenvectors of $\langle \mathcal{T}(t)\rangle$ in Figs. 2.9(a) and 2.14(b) highlight a close connection with the vectors $|\nu\rangle$, and therefore with the local diagonal orbit pairings $|s\rangle$. In particular, at late times we find $\langle \mathcal{B}_L|0,t;R\rangle\,\langle 0,t;L|\mathcal{B}_R\rangle \simeq t$, to be compared with $\langle \mathcal{B}_L|\nu=0\rangle\,\langle \nu=0|\mathcal{B}_R\rangle = t$. Additionally, $\langle \nu|\nu,t;R\rangle\,\langle \nu,t;L|\nu\rangle \simeq 1$. Since $|\nu,t;R\rangle$ and $\langle \nu,t;L|$ are vectors in a space of very high dimension for large t, it is remarkable to find that they have such large overlap with $|\nu\rangle$, and even more striking that this overlap approaches unity at large t. However, because the left and right eigenvectors of $\langle \mathcal{T}(t)\rangle$ form a biorthogonal set, as opposed to being orthonormal, this does not necessarily imply equality of the leading eigenvectors and the $|\nu\rangle$ vectors.

We construct a space-time-local probe of the orbit pairing as follows; without loss of generality we choose to probe the $s = 0$ pairing at time step $r = 0$.

Writing the forward orbit of site x as $(a_0 b_0 \dots a_{t-1} b_{t-1})$ and the backward orbit as $(a_0^* b_0^* \dots a_{t-1}^* b_{t-1}^*)$, our probe for the step 0 should return 1 if $a_0 = a_0^*$ and $-1/q$ otherwise. In this way its average vanishes if a_0 and a_0^* are uncorrelated q-valued random numbers. A suitable operator, $\mathcal{D}$, acts on orbit pairs as

$$\mathcal{D}\,|a_0 b_0 \dots\rangle \otimes |a_0^* b_0^* \dots\rangle = \frac{\delta_{a_0 a_0^*} - 1/q}{1 - 1/q}\,|a_0 b_0 \dots\rangle \otimes |a_0^* b_0^* \dots\rangle\,. \tag{2.45}$$

Our protocol is then as follows: we impose orbit pairings s_L and s_R on the respective left- and right-hand sites, as in $Z(s_R - s_L, t)$, and insert $\mathcal{D}$ into the product of transfer matrices in Eq. (2.37). If we probe the orbit pairing of a site with x even we redefine $\mathcal{D} \to \mathcal{S}\mathcal{D}\mathcal{S}^{-1}$. For an individual realisation, and for site x, the quantity of interest is

$$D(s_L, s_R, t, x) = \frac{\langle s_L|\mathcal{T}_{0,1}(t) \dots \mathcal{D}\mathcal{T}_{x,x+1}(t) \dots |s_R\rangle}{\langle s_L|\mathcal{T}_{0,1}(t) \dots \mathcal{T}_{L-2,L-1}(t)|s_R\rangle}. \tag{2.46}$$

Here we have inserted $\mathcal{D}$ between the transfer matrices $\mathcal{T}_{x-1,x}(t)$ and $\mathcal{T}_{x,x+1}(t)$ in the numerator. The denominator is $Z(s_R - s_L, t)$. We are interested in average properties of the sum over many-body orbits generating the SFF, and therefore define the average $\langle D(s_L, s_R, t, x)\rangle$ as the ratio of the average numerator to the average denominator,

$$\langle D(s_L, s_R, t, x)\rangle = \frac{\langle s_L|\langle\mathcal{T}(t)\rangle^x \mathcal{D} \langle\mathcal{T}(t)\rangle^{L-1-x}|s_R\rangle}{\langle s_L|\langle\mathcal{T}(t)\rangle^{L-1}|s_R\rangle}. \tag{2.47}$$

Although both the numerator and denominator of Eq. (2.46) are nonzero and positive after averaging, this is not the case in all disorder realisations. Consequently it is not possible to average the right-hand side of Eq. (2.46) directly.

Consider imposing a particular pairing domain using the boundary conditions $s_L = s_R = s$, as in $Z(0, t)$. At late times, if the forward and backward many-body orbits are diagonally paired, we expect $\langle D(s, s, t, x)\rangle$ to be equal to unity if $s = 0$ and equal to zero if $s \neq 0$. At early times, based on the results of Fig. 2.12, we anticipate domain wall contributions. The corresponding multi-domain orbit pairing configurations suppress $\langle D(0, 0, t, x)\rangle$ and enhance $\langle D(s, s, t, x)\rangle$ for $s \neq 0$. In Fig. 2.16(a) we show $\langle D(s, s, t, x)\rangle$ for domains $s = 0$ and $s = 1$, and find exactly the behaviour expected.

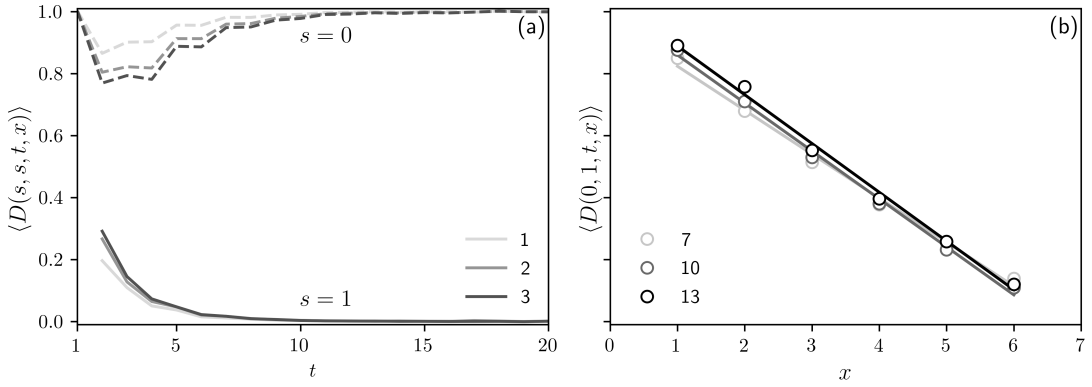

Figure 2.16: $\langle D(s_L, s_R, t, x)\rangle$ [Eq. (2.46)] with $L = 8$ sites. (a) Imposing a particular domain $s_L = s_R$, with (dashed) $s_L = s_R = 0$ and (solid) $s_L = s_R = 1$. The legend shows x. (b) Imposing a domain wall: $s_L = 0$ and $s_R = 1$, and sweeping across it. The legend shows t, and lines are linear fits.

To study the pairing across a domain wall, we impose $s_L = 0$ and $s_R = s \neq 0$ as in $Z(s, t)$. In this case, as we increase x and thereby sweep across the domain wall, we expect $\langle D(0, s, t, x)\rangle$ to decrease toward zero, and in Fig. 2.16(b) we confirm that this is indeed the case. The results of Fig. 2.16 demonstrate quite directly the existence of domains in the orbit pairing.

2.5.4 Bath interpretation

We have seen that the time dependence of the eigenvalues $\lambda(\nu, t)$ is implied by (i) the approach of $\langle Z(0, t)\rangle$ to unity and (ii) the decay of $\langle Z(s \neq 0, t)\rangle$ to zero at late times. Here we show that this occurs in individual disorder realisations, and highlight a connection between the behaviour of $Z(0, t)$ and the behaviour of a system coupled at its ends to Markovian baths.

Consider first evolution under only the Floquet operator W. The SFF can be written $K(t) = \mathrm{Tr}[W(t) \otimes W^*(t)]$, where $W \otimes W^*$ is the doubled Floquet operator, and the trace is over the q^{2L}-dimensional doubled Fock space. To couple the system to a bath we act on each of the sites $x = 0$ and $(L - 1)$ with independent $q \times q$ Haar-random unitary matrices at each time step. Writing the composite index for the end sites 0 and $(L - 1)$ using Greek letters α, β, and the composite index for the $(L - 2)$ central sites using Roman letters a, b, the components of the doubled

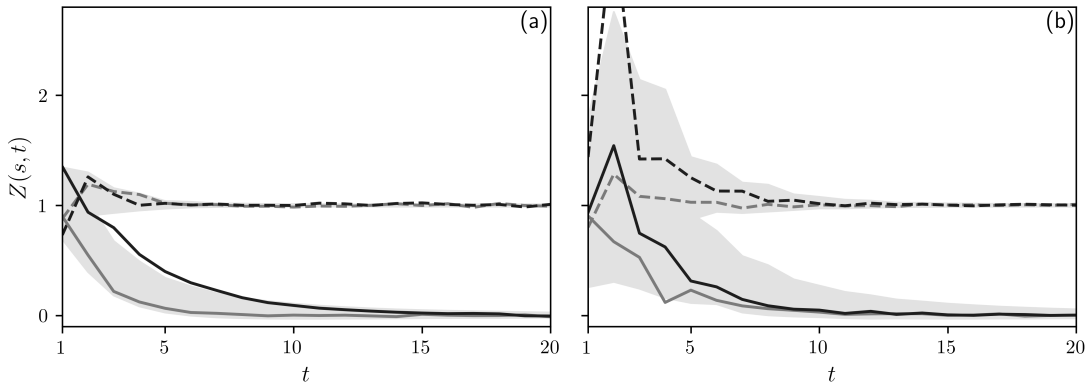

Figure 2.17: $Z(s,t)$ for (a) $L=4$, (b) $L=8$ and (dashed) $s=0$, (solid) $s=1$, for two randomly selected realisations (respective grey and black lines). Shaded areas are centred on $\langle Z(s,t)\rangle$ and have vertical width equal to twice the ensemble standard deviation.

Floquet operator $W\otimes W^*$ are $W_{a\alpha,b\beta}W^*_{a^*\alpha^*,b^*\beta^*}$. Averaging over the bath couplings we find that the only nonzero matrix elements have $\alpha=\alpha^*$ and $\beta=\beta^*$. This average therefore forces local diagonal pairings of the orbits of each of the sites $x=0$ and $(L-1)$, as discussed in connection with Fig. 2.11.

Defining the operators $Q^{\alpha\beta}$, with components $Q^{\alpha\beta}_{ab}=(1/q)W_{a\alpha,b\beta}$, the quantum channel describing the evolution of the central $(L-2)$ sites is represented by the operator

$$\mathcal{Q}=\sum_{\alpha\beta}Q^{\alpha\beta}\otimes(Q^{\alpha\beta})^*. \tag{2.48}$$

$\mathcal{Q}$ acts on the $q^{2(L-2)}$-dimensional doubled space of the central $(L-2)$ sites. This gives us the expression

$$Z(0,t)=\mathrm{Tr}\mathcal{Q}^t, \tag{2.49}$$

a sum over orbits with local diagonal pairing at the ends of the system. The matrix $\mathcal{Q}$ has leading eigenvalue unity, and the corresponding eigenvector describes a density matrix proportional to the identity. In generic circuit realisations the other eigenvalues of $\mathcal{Q}$ lie within the unit circle, so at late times $Z(0,t)$ approaches unity. We show this behaviour for individual circuit realisations in Fig. 2.17. We find also that, for s nonzero, $Z(s,t)$ decays to zero with increasing time. In the language of Sec. 2.5.2 this implies an approach toward a global orbit pairing in individual circuit realisations.

2.6 Subleading eigenvalues

So far all of the information we have on the average transfer matrix $\langle \mathcal{T}(t) \rangle$ has come from the scaling of certain of elements of $\langle \mathcal{T}(t) \rangle^L$ with L. For comparison it is useful to calculate the eigenvalues of $\langle \mathcal{T}(t) \rangle$ directly. With access to the subleading eigenvalues, we can also investigate the origin of the plateau in $\langle K(t) \rangle$.

To observe a plateau we require $t > t_{\mathrm{H}} = q^L$, and for Haar-RFCs $q \geq 2$ and $L \geq 2$; even at time $t = 5$ the dimension of the space of orbit pairs is $q^{4t} = 2^{20}$. This is already a computational challenge, especially when a disorder average is required. In this section we show how to use the analytic structure of $\langle \mathcal{T}(t) \rangle$, and its symmetries, to drastically reduce the computing power required to determine its spectrum. First, note that the $q^{4t} \times q^{4t}$ matrix $\langle \mathcal{T}(t) \rangle$ acts in the space spanned by the permutation states $|\sigma, \tau\rangle$ [Eqs. (2.24) and (2.25)]. There are $(t!)^2$ such states but, in general, they are not all linearly independent. Using the time-translation symmetries, our aim is to block-diagonalise $\langle \mathcal{T}(t) \rangle$ within the space of $|\sigma, \tau\rangle$ states.

Recall that the transfer matrix commutes with the full-step time-translation operators acting on each of the forward and backward orbits, $S^2 \otimes \mathbb{1}$ and $\mathbb{1} \otimes S^2$, respectively. These operators act on the permutation states $|\sigma, \tau\rangle$ as

$$\begin{aligned} S^2 \otimes \mathbb{1} \, |\sigma, \tau\rangle &= |\sigma c, \tau c\rangle \\ \mathbb{1} \otimes S^2 \, |\sigma, \tau\rangle &= |c^{-1}\sigma, c^{-1}\tau\rangle \, . \end{aligned} \tag{2.50}$$

Here c is the cyclic permutation mapping $r \to (r+1)$ modulo t. We also have $\mathcal{S} \, |\sigma, \tau\rangle \; = \; S \otimes S \, |\sigma, \tau\rangle \; = \; |\tau, c^{-1}\sigma c\rangle$.

Starting from $|\sigma, \tau\rangle$, the states $(S^{2r_+} \otimes S^{2r_-}) \; |\sigma, \tau\rangle$ for $r_+, r_- = 0 \ldots (t-1)$ define an equivalence class of maximum cardinality t^2: we write $|\sigma, \tau\rangle \sim |\sigma', \tau'\rangle$ if $|\sigma', \tau'\rangle \; = \; (S^{2r_+} \otimes S^{2r_-}) \; |\sigma, \tau\rangle$ for some r_+, r_-. This equivalence relation partitions the set of $(t!)^2$ permutation states. We label each equivalence class by one of the permutations belonging to it, which we refer to as the root. From here on the states within the class with root $|\sigma, \tau\rangle \equiv |\sigma, \tau; 0, 0\rangle$ will be written

$$|\sigma, \tau; r_+, r_-\rangle \equiv (S^{2r_+} \otimes S^{2r_-}) \, |\sigma, \tau; 0, 0\rangle \, . \tag{2.51}$$

This representation is not necessarily unique. As an example, for integer a we have $|\mathbb{1},\mathbb{1};r_+r_-\rangle = |\mathbb{1},\mathbb{1};r_+ + a, r_- + a\rangle$. Nevertheless, a simplification follows from the fact that if $|\sigma,\tau;r_+,r_-\rangle = |\sigma,\tau;r'_+,r'_-\rangle$ then $|\sigma,\tau;r_+ + a, r_- + b\rangle = |\sigma,\tau;r'_+ + a, r'_- + b\rangle$. This implies that, if we allow r_+, r_- to run from $0 \ldots (t-1)$, each state within the class appears the same number of times. We define this number as the multiplicity of the class, $m(\sigma,\tau)$. From the above we see that $m(\mathbb{1},\mathbb{1}) = t$.

With this structure in place we can separate the sum in Eq. (2.25) into separate sums over roots $|\sigma,\tau;0,0\rangle$ and over states within the corresponding classes. Note that the average transfer matrix in Eq. (2.25) involves the outer products $\mathcal{S}\,|\sigma,\tau\rangle\,\langle\sigma,\tau|$, and consequently its action connects the different equivalence classes. Having chosen roots it is convenient to define

$$|\mathcal{S}(\sigma,\tau);a_+(\sigma,\tau),a_-(\sigma,\tau)\rangle \equiv \mathcal{S}\,|\sigma,\tau;0,0\rangle \tag{2.52}$$

where the root $|\mathcal{S}(\sigma,\tau);0,0\rangle$ is defined relative to $|\sigma,\tau;0,0\rangle$. The integers $a_+(\sigma,\tau)$ and $a_-(\sigma,\tau)$ depend on our initial choice of roots. In terms of roots and classes, we then find

$$\langle\mathcal{T}(t)\rangle = {\sum_{\sigma\tau}}' \frac{\mathrm{Wg}(\sigma\tau^{-1})}{m(\sigma,\tau)} \sum_{r_+,r_-=0}^{t-1} |\mathcal{S}(\sigma,\tau);a_+(\sigma,\tau)+r_+,a_-(\sigma,\tau)+r_-\rangle\,\langle\sigma,\tau;r_+,r_-|\,,$$

where the primed sum ${\sum}'_{\sigma\tau}$ is only over roots. Note that we have used the fact that the Weingarten function depends only on the conjugacy class of its argument.

We now define the Fourier transforms, over the coordinates r_+ and r_-, for each class,

$$|\sigma,\tau;\nu_+,\nu_-\rangle = \frac{1}{t}\sum_{r_+,r_-=0}^{t-1} e^{-2\pi i(\nu_+ r_+ + \nu_- r_-)/t}\,|\sigma,\tau;r_+,r_-\rangle\,. \tag{2.53}$$

Inverting this expression we find, for the sector (ν_+,ν_-),

$$\begin{aligned}\langle\mathcal{T}(t;\nu_+,\nu_-)\rangle = {\sum_{\sigma\tau}}' &\frac{\mathrm{Wg}(\sigma\tau^{-1})}{m(\sigma\tau)} e^{-2\pi i(\nu_+ a_+(\sigma,\tau)+\nu_- a_-(\sigma,\tau))/t} \\ &\times |\mathcal{S}(\sigma,\tau);\nu_+,\nu_-\rangle\,\langle\sigma,\tau;\nu_+,\nu_-|\,.\end{aligned}$$

To find the eigenvalues of $\langle\mathcal{T}(t;\nu_+,\nu_-)\rangle$ we express it in an orthonormal basis and then diagonalise it numerically. Note that different sectors contain different classes.

For example, $|\mathbb{1},\mathbb{1};\nu_+,\nu_-\rangle$ vanishes unless $\nu_+ = -\nu_-$. The general procedure for constructing the basis is as follows. First we determine the class inner products

$$\langle\sigma,\tau;\nu_+,\nu_-|\sigma',\tau';\nu_+,\nu_-\rangle \tag{2.54}$$

which can be computed using Eq. (2.53) and $\langle\sigma',\tau'|\sigma,\tau\rangle = \langle\sigma'|\sigma\rangle\langle\tau'|\tau\rangle$, where $\langle\sigma'|\sigma\rangle = q^{N(\sigma^{-1}\sigma')}$ with $N(\sigma^{-1}\sigma')$ the number of cycles in the permutation $\sigma^{-1}\sigma'$. From this information we seek orthogonal (but not yet normalised) basis states

$$|\tilde{i}\rangle = {\sum_{\sigma\tau}}' U_{i;\sigma,\tau}\,|\sigma,\tau;\nu_+,\nu_-\rangle\,, \tag{2.55}$$

with $\langle\tilde{i}|\tilde{j}\rangle = 0$ for $i \neq j$. In each sector (ν_+,ν_-) we define a matrix $\mathcal{I}$ of class inner products via its components $\mathcal{I}_{\sigma,\tau;\sigma',\tau'} = \langle\sigma,\tau;\nu_+,\nu_-|\sigma',\tau';\nu_+,\nu_-\rangle$. Here σ,τ is a row index and σ',τ' a column index. Then

$$\langle\tilde{i}|\tilde{j}\rangle = {\sum_{\substack{\sigma\tau\\ \sigma'\tau'}}}' U^*_{i;\sigma,\tau}\mathcal{I}_{\sigma,\tau;\sigma',\tau'}U_{j;\sigma',\tau'}, \tag{2.56}$$

so choosing the rows of U to be eigenvectors of $\mathcal{I}$ we have $\langle\tilde{i}|\tilde{j}\rangle = \Lambda_i\delta_{ij}$, where Λ_i is the i^{th} eigenvalue of $\mathcal{I}$. Since $\langle\tilde{i}|\tilde{i}\rangle \geq 0$, we expect $\Lambda_i \geq 0$. The orthonormal basis is then defined by $|\tilde{i}\rangle = \sqrt{\Lambda_i}\,|i\rangle$. If the states $|\sigma,\tau;\nu_+,\nu_-\rangle$ are not all linearly independent, some of these eigenvalues will vanish: if $\Lambda_i = 0$ then $|\tilde{i}\rangle$ does not exist.

In terms of the orthonormal basis states $|i\rangle$ we have

$$|\sigma,\tau;\nu_+,\nu_-\rangle = \sum_i U^*_{i;\sigma,\tau}\sqrt{\Lambda_i}\,|i\rangle\,. \tag{2.57}$$

The transfer matrix block ν_+,ν_- has elements

$$\begin{aligned}\langle\mathcal{T}(\nu_+,\nu_-)\rangle_{ij} = {\sum_{\sigma\tau}}'\sum_{ij}\frac{\mathrm{Wg}(\sigma\tau^{-1})}{m(\sigma,\tau)}e^{-2\pi i(\nu_+a_+ + \nu_-a_-)/t}\\ \times\sqrt{\Lambda_i\Lambda_j}[U^*]_{i;\mathcal{S}(\sigma,\tau)}[U]_{j;\sigma,\tau},\end{aligned} \tag{2.58}$$

which is an expression for the matrix elements of the different symmetry blocks of $\langle\mathcal{T}(t)\rangle$ in an orthonormal basis. At this point we can use ED to obtain all of the eigenvalues and eigenvectors. The leading eigenvalues $\lambda(\nu,t)$ computed through this method, as well as the overlaps of the corresponding eigenvectors with the local

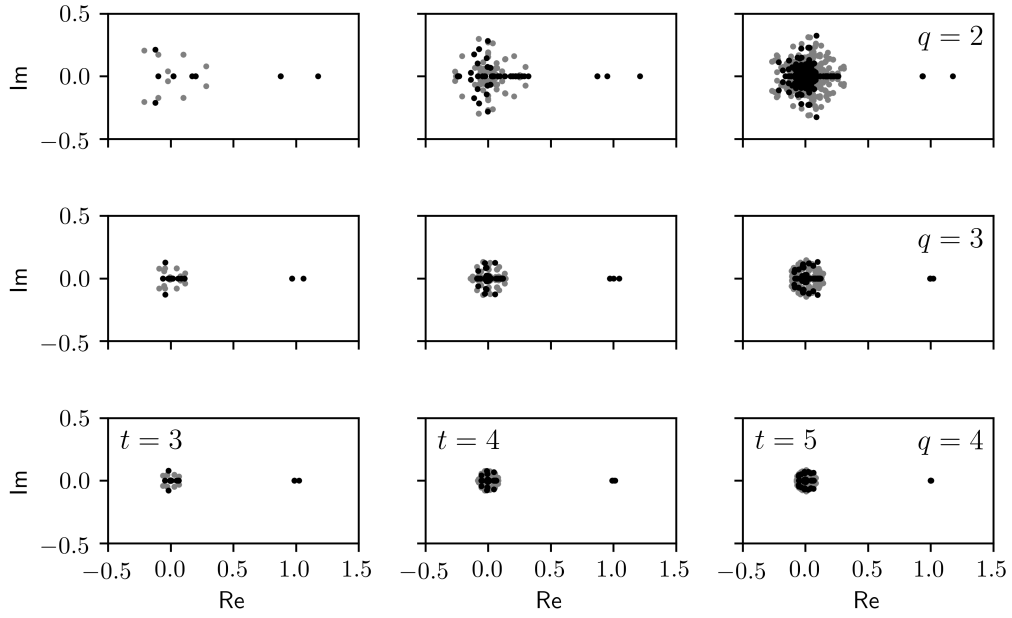

Figure 2.18: $\langle \mathcal{T}(t) \rangle$ eigenvalues for $t = 3, 4, 5$ (columns, from left) and $q = 2, 3, 4$ (rows, from top) in the complex plane, from ED of Eq. (2.58). Black points indicate eigenvalues in sectors with $\nu_+ = -\nu_-$, and grey points indicate all other sectors. The t leading eigenvalues, some degenerate, are distributed around unity.

diagonal states, are shown in Fig. 2.14 for $t \leq 5$, and we find excellent agreement with the L-scaling approaches in Sec. 2.5.

Because the leading eigenvalues $\lambda(\nu, t)$ all approach unity at large t [see Fig. 2.14] they cannot be responsible for the plateau beyond the Heisenberg time $t_{\mathrm{H}} = q^L$. For $t \leq q^L$ the subleading eigenvalues do very little, whereas for $t = q^L + \delta t$ their contribution to $\langle K(t) \rangle$ must be $-\delta t$. We have verified this using the procedure detailed above for $q = 2$ and $t = 5$. For $q = 3$ and $L = 2$, already $t_{\mathrm{H}} = 9$; the number of permutation states at $t = 10$ is $(10!)^2 \sim 10^{13}$, which is prohibitively large.

Another question concerns the effect of varying q. For Haar-RFCs in the limit of large q, $\langle K(t) \rangle = t$ for nonzero integer t [34]. As we have seen, new phenomena appear at small q: orbit pairing domains come from the deviations of the leading eigenvalues $\lambda(\nu, t)$ from unity, and the late-time plateau comes from the subleading eigenvalues. Based on these considerations it is natural to expect that increasing q at fixed t causes (i) $\lambda(\nu, t)$ to approach unity and (ii) all other eigenvalues to approach zero. Fig. 2.18 shows all of the eigenvalues of $\langle \mathcal{T}(t) \rangle$ for times $t = 3, 4, 5$

and $q = 2, 3, 4$, and confirms that this is the behaviour. Additionally, we see that there is a distinct gap between $\lambda(\nu, t)$ and all subleading eigenvalues.

2.7 Tuning away from Haar

In Sec. 2.5 we studied the average transfer matrix $\langle \mathcal{T}(t) \rangle$ for RFCs with Haar-random gates. In some ways this is an extreme case, because in these models there are no deviations from RMT within the diagonal approximation. Domain wall contributions are therefore dominant. In this section we consider the diagonal approximation to the average SFF for a more general ensemble of RFCs, in which the gates can be tuned away from Haar-randomness. However, we will see that in the vicinity of Haar-randomness, domain wall contributions remain dominant.

We parametrise the two-site gates U of the circuit via their spectral decompositions, $U = Ve^{i\phi}V^\dagger$. Here ϕ is a diagonal matrix, and we take the unitary matrix V to be Haar random. If we choose $e^{i\phi}$ to be distributed as the eigenvalues of a Haar-random unitary then U is Haar random. On the other hand if $e^{i\phi}$ is proportional to the identity, so is U. By tuning the distribution of ϕ we can interpolate between these two extremes.

In a brickwork model the diagonal propagator is of the form Eq. (2.10). The gate acting on sites 0 and 1 in the first half-step appears in $\mathcal{P}_{a_0 \dots a_{L-1}, b_0 \dots b_{L-1}}$ as $[U_{0,1}]_{c_0 c_1, b_0 b_1} [U^*_{0,1}]_{c_0^* c_1^*, b_0 b_1}$, where the indices c, c^* are to be summed over. The average over U now involves an average over V and an independent average over the ϕ-distribution. This gives

$$\langle [U_{0,1}]_{c_0 c_1, b_0 b_1} [U^*_{0,1}]_{c_0^* c_1^*, b_0 b_1} \rangle = \nu \delta_{c_0 b_0} \delta_{c_1 b_1} \delta_{c_0^* b_0} \delta_{c_1^* b_1} + \frac{1}{q^2}(1-\nu) \delta_{c_0 c_0^*} \delta_{c_1 c_1^*}, \tag{2.59}$$

where

$$\nu = \frac{\langle |\mathrm{Tr} U|^2 \rangle - 1}{q^4 - 1}. \tag{2.60}$$

Clearly for $\nu = 0$ we recover the Haar-random result Eq. (2.11). On the other hand for U proportional to the identity we have $\nu = 1$. The average propagator, with matrix elements $\langle \mathcal{P}_{a_0 \dots a_{L-1}, b_0 \dots b_{L-1}} \rangle$, is given by multiplying expressions of the form

Eq. (2.59) and summing over indices c, c^*. The result is a matrix-product operator (MPO), and with periodic boundary conditions this takes the form

$$\langle \mathcal{P}_{a_0 \ldots a_{L-1}, b_0 \ldots b_{L-1}} \rangle = \mathrm{Tr}[M_{a_0 b_0} \ldots M_{a_{L-1} b_{L-1}}], \tag{2.61}$$

where M_{ab} is a real-symmetric 2×2 matrix with components

$$M_{ab} = \begin{pmatrix} \nu \delta_{ab} & \frac{1}{q}\sqrt{\nu}\sqrt{1-\nu} \\ \frac{1}{q}\sqrt{\nu}\sqrt{1-\nu} & \frac{1}{q}(1-\nu) \end{pmatrix}. \tag{2.62}$$

The eigenvectors of the MPO in Eq. (2.61) are product states $v^{\sigma_0} \otimes \ldots v^{\sigma_{L-1}}$ that we label with $\sigma_x = 0 \ldots (q-1)$ for $x = 0 \ldots (L-1)$. The q-component vectors v^σ must satisfy

$$\sum_{b=0}^{q-1} M_{ab}^{ij} v_b^\sigma = \mu_\sigma^{ij} v_a^\sigma. \tag{2.63}$$

This is achieved by taking v^0 to have constant entries, and $v^{\sigma \neq 0}$ to make up the rest of an orthonormal set. The resulting 2×2 matrices μ_σ, with components μ_σ^{ij}, are outer products

$$\mu_\sigma = \begin{pmatrix} \sqrt{\nu} \\ \sqrt{1-\nu}\delta_{\sigma 0} \end{pmatrix} \begin{pmatrix} \sqrt{\nu} & \sqrt{1-\nu}\delta_{\sigma 0} \end{pmatrix}, \tag{2.64}$$

and the eigenvalues of $\langle \mathcal{P} \rangle$ are $\mathrm{Tr}[\mu_{\sigma_0} \ldots \mu_{\sigma_{L-1}}]$. The leading eigenvalue is unity as required by unitarity of W, and the next-to-leading eigenvalues are ν^2 with multiplicity $L(q-1)$. Within the diagonal approximation the average SFF $\langle K(t) \rangle = t \mathrm{Tr} \langle \mathcal{P} \rangle^t$ is

$$\begin{aligned} \langle K(t) \rangle &= t \sum_{\sigma_0 \ldots \sigma_{L-1}} \mathrm{Tr}[\mu_{\sigma_0} \ldots \mu_{\sigma_{L-1}}]^t \\ &= t[1 + L(q-1)\nu^{2t} + \ldots], \end{aligned} \tag{2.65}$$

where in the second line we have expanded around the late-time result. For $0 < \nu < 1$, $\langle K(t) \rangle / t$ decreases monotonically with t. Writing $\nu^{2t} = e^{-2\ln(1/\nu)t}$ we see that the Thouless time is $t_{\mathrm{Th}} = \ln L / [2 \ln(1/\nu)]$ within the diagonal approximation. This behaviour should be contrasted with that expected when domain wall contributions are dominant. In that case there is a competition between the 'energetic' cost of domain walls ($e^{-\varepsilon t}$ in the RPM) and the entropy associated with the t choices of

orbit pairing in each domain. In Fig. 2.4 we have seen that this leads to an initial increase of $\langle K(t)\rangle/t$ before it eventually decreases to the RMT result of unity.

In the general case the SFF has contributions both from subleading eigenvalues of the diagonal propagator and from domain walls. Determining which effect is dominant requires a comparison of the associated timescales. For Haar-RFCs, which have $\nu = 0$, we have seen that for finite q the domain wall tensions $\varepsilon(s,t)$ in Eq. (2.43) are finite. Since ν sets the proximity of the gates to the identity it is natural to expect these tensions to decrease with increasing ν. On the other hand, the subleading eigenvalues of the diagonal propagator vanish for $\nu = 0$. The behaviour we have studied in Haar-RFCs, in which domain walls control the SFF, must therefore extend to at least a finite range of ν, so is not restricted to the Haar case.

2.8 Spectral fluctuations

We now turn to a brief investigation of the sample-to-sample fluctuations of $K(t)$ within the ensemble of Haar-RFCs. In Fig. 2.3 we have already shown that a local average dramatically suppresses statistical fluctuations of the SFF, a global quantity. Here we set out to understand this and the distribution of spectra more generally.

Information on the distribution of spectra is buried in the moments of $K(t)$. The n^{th} moment $\langle K^n(t)\rangle$ is an average over the product of n copies, or replicas, of the forward orbits $\mathrm{Tr}W(t)$ and n copies of the backward $\mathrm{Tr}W^*(t)$. Focusing on only the second moment, in Sec. 2.8.1 we make some first steps toward adapting our theory of local orbit pairing to these higher order objects, and demonstrate non-Gaussian statistics of the SFF. In Sec. 2.8.3 we discuss a connection with the entanglement membrane.

2.8.1 Non-Gaussian statistics

To ground the discussion, consider first the case where W is a single Haar-random matrix. In the limit of large matrix dimension $\mathrm{Tr}W(t)$ is then normally distributed, with mean zero, in the complex plane [130]. In calculating the second moment of

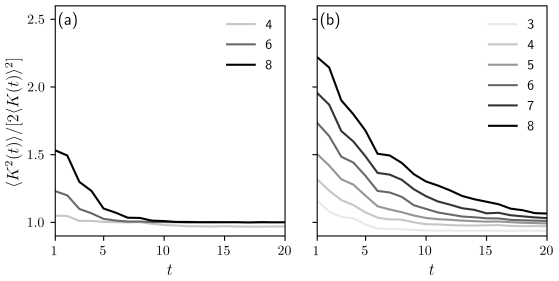

Figure 2.19: Statistical fluctuations: $\langle K^2(t)\rangle/[2\langle K(t)\rangle^2]$, equal to 1 within RMT, for (a) periodic boundary conditions and (b) open boundary conditions. The legend shows L.

the spectral form factor, $\langle K^2(t)\rangle = \langle|\mathrm{Tr}W(t)|^4\rangle$, Wick's theorem gives a sum over the two possible pairings of copies of $\mathrm{Tr}W(t)$ and its conjugate,

$$\begin{aligned}\langle K^2(t)\rangle = \mathrm{Tr}\overbrace{W(t)\mathrm{Tr}}W^*(t)\mathrm{Tr}\overbrace{W(t)\mathrm{Tr}}W^*(t)\Big\}+\\ +\mathrm{Tr}\overbrace{W(t)\mathrm{Tr}\overbrace{W^*(t)\mathrm{Tr}}W(t)\mathrm{Tr}}W^*(t)\Big\}-\end{aligned} \tag{2.66}$$

where we have denoted the two copy pairings '+' and '−'. Each of the '+' and '−' copy pairings contributes $\langle K(t)\rangle^2$, so $\langle K^2(t)\rangle = 2\langle K(t)\rangle^2$. Here the copy pairing is necessarily global since our evolution operator is just one Haar-random matrix.

The global pairing of copies in Eq. (2.66) is to be contrasted with the situation in a circuit model. We have seen already that the local freedom in the pairing of orbits gives rise to deviations of the average SFF from the RMT prediction, and now in $\langle K^2(t)\rangle$ there is an additional local freedom in the pairings of copies of these orbits. We show in Fig. 2.19 that this gives rise to non-Gaussian statistics of the spectral form factor at early times. Specifically we show that $\langle K^2(t)\rangle/[2\langle K(t)\rangle^2]$ is signficantly larger than unity even in small systems, and grows as L increases at fixed t.

As a point of comparison, we now sketch the calculation of $\langle K^2(t)\rangle$ for the RPM in the large-q limit [see also Ref. [131]]. In $K^2(t) = |\mathrm{Tr}W(t)|^4$ each single-site Haar-random gate u_x appears t times in each of the two copies of $\mathrm{Tr}W(t)$, and similarly its conjugate appears t times in each of the two copies of $\mathrm{Tr}W^*(t)$. Averaging each u_x at large q we find a sum over pairings of orbits analogous to Eq. (1.7), and additionally a sum over the two pairings of copies of these orbits, as in Eq. (2.66). $\langle K^2(t)\rangle$ is then a sum over all local orbit pairings, as in Eq. (2.13), and additionally a sum over all local copy pairings. Whereas a domain wall in the orbit pairing has

statistical weight $e^{-\varepsilon t}$, it can be shown that a domain wall in the copy pairing here has statistical weight $e^{-2\varepsilon t}$. With open boundary conditions we have

$$\langle K^2(t)\rangle = 2\langle K(t)\rangle^2 + 2(L-1)t^4 e^{-2\varepsilon t} + \dots . \tag{2.67}$$

The first term on the right-hand side of Eq. (2.67) involves contributions from domain walls in the orbit pairing, as in Eq. (2.14), whereas the second term arises from a domain wall in the pairing of copies of orbits. The factor $(L-1)$ is the translational entropy of this domain wall, and the factor t^4 arises from sums over the orbit pairing at each of the two ends of the two copies of the chain. By contrast, with periodic boundary conditions and at late times the leading term in $\langle K^2(t)\rangle - 2\langle K(t)\rangle^2$ comes from configurations with two domain walls in the copy pairing. We therefore expect smaller deviations from Gaussian statistics, and Fig. 2.19 shows exactly this type of behaviour.

2.8.2 Exchanged boundary conditions

A useful analogy with Sec. 2.5.2 is now evident. There a great deal was learnt about $\langle K(t)\rangle$ via calculations in which boundary conditions were imposed to force diagonal pairings of the local orbits. In this approach the emergence of RMT level statistics on small energy scales in Haar-RFCs can be understood as arising from a global pairing of orbits at late times. Looking at Eq. (2.66) we see that in order to recover RMT statistics of the SFF beyond only the first moment we also require a global pairing of copies of orbits.

Proceeding in a similar way then to Sec. 2.5.2, here we investigate how, in the calculation of the second moment of the spectral form factor, a local freedom in the pairing of copies of orbits gives way to a global pairing. To do this we again impose local diagonal pairings at opposite ends of the system, but now to force a domain wall into the pairing of copies. This setup is illustrated in Fig. 2.20. In principle we could also impose a relative twist on the orbit pairing, as in $Z(s \neq 0, t)$ [see Eq. (2.37) and Fig. 2.10], but we choose to restrict ourselves to equal-time pairing, as in $Z(0, t)$.

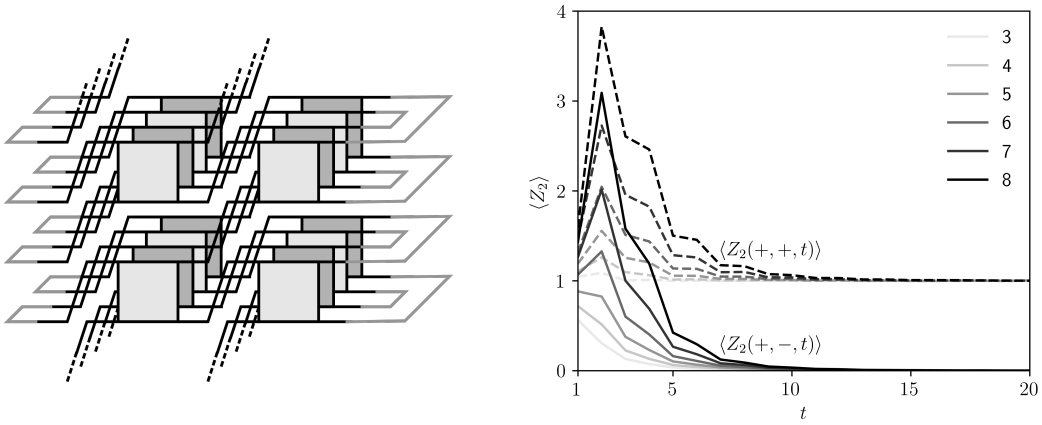

Figure 2.20: Left: diagram of $Z_2(+,-,t)$, where we force a domain wall into the pairing of copies of orbits. Different circuit layers correspond to forward (light) and backward (dark) orbits. Right: domain walls in the pairing of copies of orbits, relevant to the second moment of the SFF. Solid lines show $\langle Z_2(+,-,t)\rangle$, where the pairing of copies is different on the two ends of the system, and dashed lines show $\langle Z_2(+,+,t)\rangle$, where the pairing is the same.

In the notation of Eq. (2.66), Fig. 2.20 illustrates a '+' pairing on one end of the chain, and a '−' pairing on the other. The resulting object, which we denote $Z_2(+,-,t)$, is a multiple sum over two copies of the forward orbits and two copies of the backward orbits, with a domain wall in the pairing of copies running along the time direction. $Z_2(+,-,t)$ is to be contrasted with $Z_2(+,+,t) = Z^2(0,t)$, in which we impose equal-time pairings of the same copies of orbits at both ends of the system. In practice we impose these pairings using a variant of the Monte-Carlo method discussed in connection with Fig. 2.11; this is illustrated in Fig. 2.21.

We show the averaged quantities $\langle Z_2(+,-,t)\rangle$ and $\langle Z_2(+,+,t)\rangle$ in Fig. 2.20. We see that $\langle Z_2(+,-,t)\rangle$ grows with L at fixed t, and therefore so do the deviations from RMT. At late times, $t \gtrsim 10$ for $L \leq 8$, $\langle Z_2(+,-,t)\rangle$ goes to zero. In other words the contributions from those sets of many-body orbits with domain walls in the copy-pairing vanish. As expected, $\langle Z_2(+,+,t)\rangle$ approaches unity in this regime. The appearance of domain walls in the pairing of copies implies non-Gaussian statistics of the SFF at times $t \lesssim 10$ for these system sizes, and this behaviour is clear in Fig. 2.19.

We now return to the effect of the single-gate average observed in Fig. 2.3. To understand why an average of the spectral form factor over only one gate of

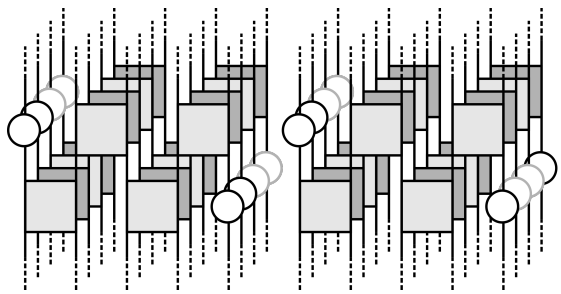

Figure 2.21: $Z_2(+,+,t)$ (left) and $Z_2(+,-,t)$ (right) from Monte Carlo. Here $t = 1$. The two copies of the forward evolution operator are shown light, and the two copies of the backward evolution operator are shown dark. Averaging over the single-site Haar-random matrices (open circles) fixes local '+' and '−' pairings between the copies of the many-body orbits.

the circuit is enough to suppress statistical fluctuations, consider performing this average and subsequently calculating the variance of the spectral form factor over the ensemble of the remaining gates. The tendency toward global copy pairing observed in Fig. 2.20 implies that the second moment can be approximated by a sum over the two global pairings ('+' and '−') at late times, as in Eq. (2.66). However, in performing the single-gate average beforehand, we have locally selected for just one of these pairings. As a result the second moment is approximately halved, so the variance is suppressed to near zero.

2.8.3 Entanglement membrane

Domain walls in the pairing of copies of orbits are related to the entanglement membrane. To see this consider the growth of the purity under unitary dynamics. The purity of a subregion A is defined as $e^{-S_A^{(2)}(t)} = \mathrm{Tr}\rho_A^2(t)$, where $\rho_A(t)$ is the reduced density matrix, and $S_A^{(2)}(t)$ is the second Renyi entropy. Writing the initial density matrix of the full system as ρ, we have

$$e^{-S_A^{(2)}(t)} = \mathrm{Tr}_A\Big[\mathrm{Tr}_B[W(t)\rho W^\dagger(t)]\mathrm{Tr}_B[W(t)\rho W^\dagger(t)]\Big]. \tag{2.68}$$

Here the boundary condition at time 0 is set by ρ, and the boundary condition at time t is determined by the trace structure in Eq. (2.68); this is illustrated in Fig. 2.22. The boundary condition at time t imposes a domain wall, the entanglement membrane, in the pairing of the copies of the evolution operator. A similar domain wall in the pairing of copies appears in $Z_2(+,-,t)$. In that case, as shown in Fig. 2.20, it is imposed by boundary conditions at the left and right ends of the chain, while the boundary conditions in time are periodic.

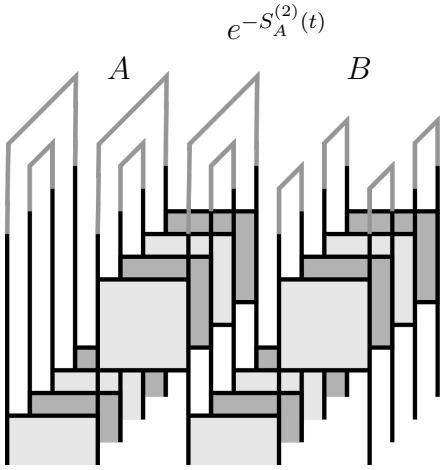

Figure 2.22: Boundary conditions defining the entanglement membrane which appears in the calculation of the purity $e^{-S_A^{(2)}(t)}$ of subregion A. In A (left) copies of the evolution operator are contracted as in the '$-$' pairing of Eq. (2.66), and in B (right) they are contracted in the '$+$' pairing.

2.9 Eigenstate correlators

Our attention has so far been limited to spectral statistics. However, the picture of local orbit pairing, and in particular the possibility of domain walls in the pairing of orbits, has implications for local correlations between eigenstates. We will now show that there are correlations between the diagonal matrix elements of local operators, or equivalently the reduced density matrices of eigenstates. These correlations, relative to the predictions of the ETH, grow without bound in the thermodynamic limit. For concreteness we adopt the following definition of the infinite-temperature ETH, applicable to ergodic Floquet models: for a set of eigenstates drawn from a sufficiently narrow window of quasienergies, the statistical properties of the matrix elements of local observables are as for random vectors.

2.9.1 Reduced form factor

We first introduce probes for these correlations. Restricting ourselves to a single site x, let $\tau_{j,x}$ for $j = 0 \dots (q^2-1)$ be a set of orthonormal $q \times q$ Hermitian operators acting only on this site, which for brevity we will refer to as observables. Then $\mathrm{Tr}[\tau_{i,x}\tau_{j,x}] = \delta_{ij}$, and we choose $\tau_{0,x} = \mathbb{1}/\sqrt{q}$ so $\tau_{j\neq 0,x}$ are traceless. The reduced density matrix of the eigenstate $|n\rangle$ on site x is

$$\rho_x(n) = \frac{1}{q}\mathbb{1} + \sum_{j=1}^{q^2-1} \langle n|\tau_{j,x}|n\rangle\, \tau_{j,x}. \tag{2.69}$$

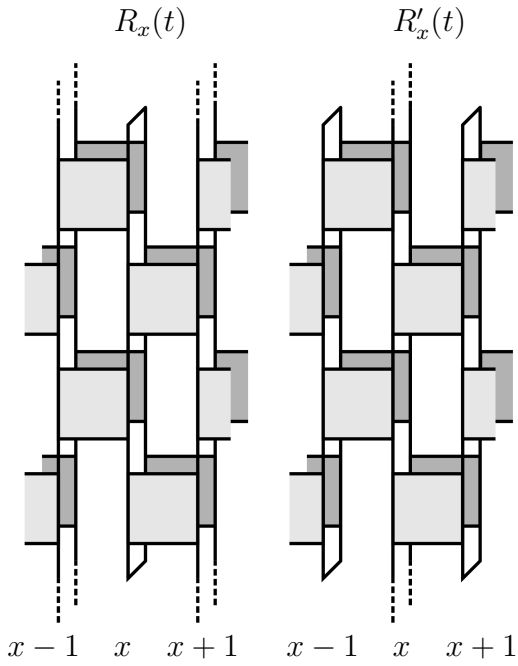

Figure 2.23: Circuit diagrams for the correlators of diagonal (left) and off-diagonal (right) matrix elements of single-site operators, $R_x(t)$ and $R'_x(t)$, respectively. Away from x, $R_x(t)$ has the same trace structure as $K(t)$, so its average is generated by the transfer matrix $\langle \mathcal{T}(t) \rangle$.

A correlator between the diagonal matrix elements of observables is then

$$\mathrm{Tr}_x[\rho_x(n)\rho_x(m)] = \frac{1}{q} + \sum_{j=1}^{q^2-1} \langle n|\tau_{j,x}|n\rangle \langle m|\tau_{j,x}|m\rangle \,, \tag{2.70}$$

where Tr_x denotes a trace over the site x. In a similar way, for the off-diagonal matrix elements, we can consider summing $|\langle n|\tau_{j,x}|m\rangle|^2$ over $\tau_{j,x}$. This gives

$$\mathrm{Tr}'_x[\rho'_x(n)\rho'_x(m)] = \frac{1}{q}\delta_{nm} + \sum_{j=1}^{q^2-1} |\langle n|\tau_{j,x}|m\rangle|^2. \tag{2.71}$$

Here $\rho'_x(n) = \mathrm{Tr}_x |n\rangle\langle n|$ is the reduced density matrix of the eigenstate $|n\rangle$ in the $(L-1)$-site complement of the site x, and Tr'_x is a trace over that region.

In the time domain the correlations between diagonal matrix elements are characterised by the reduced form factor (RFF), which we define as

$$\begin{aligned} R_x(t) &= \sum_{nm} \mathrm{Tr}_x[\rho_x(n)\rho_x(m)] e^{i(\theta_n-\theta_m)t} \\ &= \mathrm{Tr}_x[\mathrm{Tr}'_x W(t)[\mathrm{Tr}'_x W(t)]^\dagger]. \end{aligned} \tag{2.72}$$

Note that in the summand we have the correlator defined in Eq. (2.70). Spectral structure in the off-diagonal matrix elements is instead encoded in

$$\begin{aligned} R'_x(t) &= \sum_{nm} \mathrm{Tr}'_x[\rho'_x(n)\rho'_x(m)] e^{i(\theta_n-\theta_m)t} \\ &= \mathrm{Tr}'_x[\mathrm{Tr}_x W(t)[\mathrm{Tr}_x W(t)]^\dagger], \end{aligned}$$

which is the autocorrelation function of the operator $\tau_{j,x}$, averaged over choices of $\tau_{j,x}$, and is therefore accessible in principle to experimental measurements. In Fig. 2.23 we show diagrams of the correlators $R_x(t)$ and $R'_x(t)$. In light of the picture of local orbit pairing developed above we see that $R_x(t)$ and $R'_x(t)$, and therefore the diagonal and off-diagonal matrix elements, behave very differently.

In $R_x(t)$ the evolution operator appears as the product of $\mathrm{Tr}'_x W(t)$ and its Hermitian conjugate. Away from site x, $R_x(t)$ has the same trace structure as $K(t)$. This trace structure is associated with a freedom in the local orbit pairing, or more formally with the transfer matrices $\mathcal{T}_{x,x+1}$. Therefore, just as $\langle K(t)\rangle$ grows exponentially with L, so does $\langle R_x(t)\rangle$. Exact calculations are straightforward for the RPM in the large-q limit, yielding $\langle R_x(t)\rangle = (q/t)\langle K(t)\rangle$. For example, with open boundary conditions,

$$\langle R_x(t)\rangle = q\Big[1 + (L-1)(t-1)e^{-\varepsilon t} + \dots\Big]. \tag{2.73}$$

Here ellipses denote contributions from orbit-pairing configurations with more than two domains. This result is to be compared with $\langle R_x(t)\rangle = q$ within RMT. Therefore at times $t < t_{\mathrm{Th}}$, for which $\langle K(t)\rangle > t$, the average RFF $\langle R_x(t)\rangle$ may significantly exceed its RMT value. The freedom in the local orbit pairing gives rise to correlations between the diagonal matrix elements, and this effect is stronger in larger systems.

The picture of local orbit pairing does not suggest a significant modification to the ETH for the off-diagonal matrix elements of local observables, at least at the level of $R'_x(t)$. To see this, note that $R'_x(t)$ is constructed from the product of $\mathrm{Tr}_x W(t)$ and its Hermitian conjugate. Based on the trace structure, there is only a freedom in the local orbit pairing at the site x. This is demonstrated by a large-q calculation in the RPM,

$$\langle R'_x(t)\rangle = q^{L-1}[1 + (t-1)e^{-2\varepsilon t}], \tag{2.74}$$

for any x not at the end of a chain. For comparison, the RMT result is $\langle R'_x(t)\rangle = q^{L-1}$. Deviations of $\langle R'_x(t)\rangle$ from RMT do not grow with L.

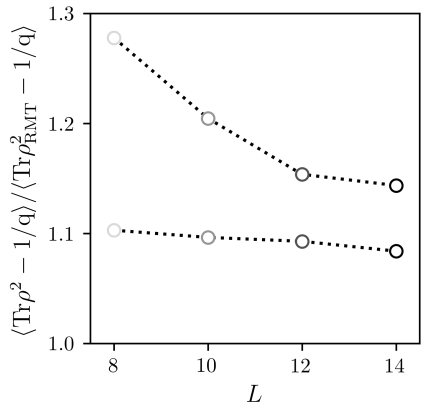

Figure 2.24: Averaged fluctuations of single-site eigenstate purities, $\langle \mathrm{Tr}\rho^2 - 1/q\rangle$, in units of the RMT average, $\langle \mathrm{Tr}\rho^2_{\mathrm{RMT}} - 1/q\rangle$, versus L for periodic (lower points) and open (upper points) boundary conditions. For open boundary conditions we exclude data from two sites at each of the two ends of the chain.

2.9.2 Quasienergy domain

In Haar-RFCs the correlator $\langle R_x(t)\rangle$ can be evaluated using an extension of the transfer matrix method detailed earlier in this chapter. Here we instead present numerical results, obtained in the quasienergy domain, using exact diagonalisation and Lanczos methods [see A.2], that demonstrate divergent departures from the ETH.

Note first that the completeness of eigenstates implies $\sum_n \rho_x(n) = q^{L-1}\mathbb{1}$, so we have the sum rule $\sum_m \mathrm{Tr}[\rho_x(n)\rho_x(m)] = q^{L-1}$. The RMT result for the average correlator is

$$\Big\langle \mathrm{Tr}[\rho_x(n)\rho_x(m)]\Big\rangle = \frac{1}{q} + \frac{q-q^{-1}}{q^{2L}-1}(q^L\delta_{nm} - 1), \tag{2.75}$$

To arrive at this expression we start by encoding the eigenstates in the columns of a $q^L \times q^L$ random unitary matrix, as this ensures that they are orthonormal. Eq. (2.75) then follows from an average of this unitary matrix over the Haar distribution, which involves evaluation of the non-zero fourth moment [see A.1.4]. On the right-hand side of Eq. (2.75), the first term arises from the non-fluctuating component $(1/q)\mathbb{1}$ of the density matrices, while the second term characterises fluctuations in the matrix elements of operators $\tau_{j,x}$ with $j \neq 0$. The $n = m$ terms in Eq. (2.75) are the eigenstate purities. We show the fluctuations of the eigenstate purities, in units of the ETH result, in Fig. 2.24. Here deviations from the ETH are small and do not grow with system size. The situation is quite different for $n \neq m$, as we now discuss.

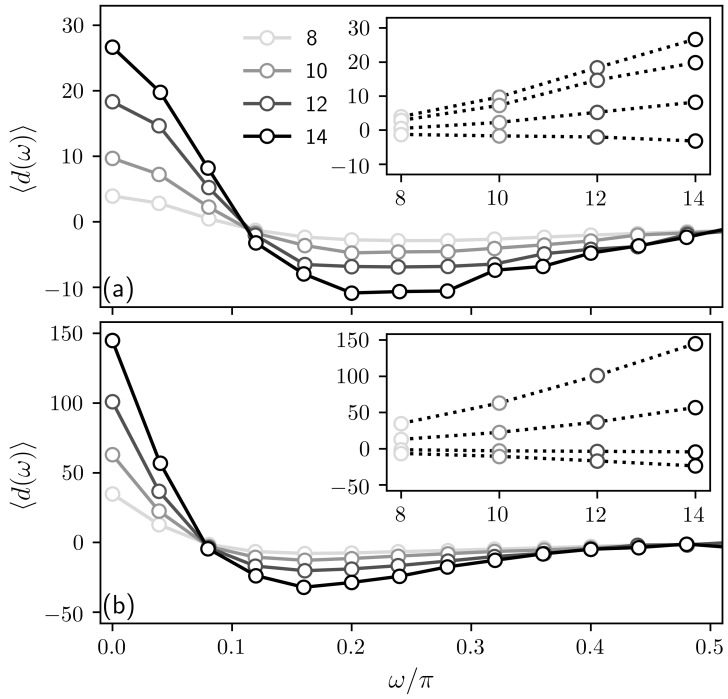

Figure 2.25: Average correlator $\langle d(\omega)\rangle$ of single-site diagonal matrix elements with (a) periodic and (b) open boundary conditions. The legend shows L, and the leftmost points correspond to an average over pairs of levels separated by $\omega/\pi \lesssim 2.5 \times 10^{-3}$. Insets: $\langle d(\omega)\rangle$ versus L for the four smallest values of ω in the main panels. The standard error in $\langle d(\omega)\rangle$ is of order unity.

It is useful to parametrise the correlator as

$$\mathrm{Tr}_x[\rho_x(n)\rho_x(m)] = \frac{1}{q} + \frac{q-q^{-1}}{q^{2L}-1}(q^L\delta_{nm} + d_{x,nm}). \tag{2.76}$$

Comparing with Eq. (2.75) we see that the ETH prediction is $\langle d_{x,nm}\rangle = -1$, but more generally the sum rule satisfied by the correlator ensures that the average of $d_{x,nm}$ over n or m is -1. It is reasonable to expect that the ensemble average is determined only by the quasienergy difference, so $\langle d_{x,nm}\rangle = \langle d_x(\omega = |\theta_n - \theta_m|)\rangle$. We define also the average of $\langle d_x(\omega)\rangle$ over x, $\langle d(\omega)\rangle$, and for open boundary conditions exclude the two sites at each of the two ends of the chain from this average. $\langle d(\omega)\rangle$ is a correlation function for the diagonal matrix elements of local observables, averaged over position and summed over an orthonormal set of observables at each site.

In Fig. 2.25 we show $\langle d(\omega)\rangle$ for both open and periodic boundary conditions. The deviations from the ETH are striking, and they are most prominent at the smallest quasienergy separations, where the ETH is conventionally thought to be applicable. The observed low-frequency peak has its origin in the late-time decay of the leading transfer-matrix eigenvalues toward unity [see Fig. 2.14]. From this we conclude that at large L the height of the peak grows exponentially with

L while its width is given by the inverse of the Thouless time, which decreases with increasing L. With open boundary conditions and for only $L = 14$ sites we find already a relative enhancement of the correlator $\langle d(\omega)\rangle$ by over two orders of magnitude. This result constitutes a substantial correction to the ETH in the ergodic phase of one-dimensional Floquet systems.

In closing, we note that objects analogous to $R_x(t)$ and $R'_x(t)$ can also be defined for operators with arbitrary spatial support. From Eqs. (2.72) and (2.73), as well as Fig. 2.23, we see that $R_x(t)$ and $R'_x(t)$ are complementary. Considering operators with support on ℓ sites, where $\ell = 1$ in the above, there is a freedom in the local orbit pairing over $(L - \ell)$ sites in the analogue of $R_x(t)$, and over ℓ sites in the analogue of $R'_x(t)$. The substitution $\ell \leftrightarrow (L - \ell)$ converts between the analogues of $R_x(t)$ and $R'_x(t)$. Whereas the spectral structure in the diagonal matrix elements grows with $(L - \ell)$, the spectral structure in the off-diagonal matrix elements grows with ℓ.

2.10 Conclusion

The spectral statistics of many-body quantum systems in the ergodic phase coincide with the predictions of RMT below a certain (quasi)energy scale, the inverse of our Thouless time t_{Th}. On timescales much greater than t_{Th}, but much shorter than the Heisenberg time t_{H}, this result can be understood through the diagonal approximation to the SFF. In this chapter we have determined the regime of validity of the diagonal approximation, and the form of the corrections to it, in systems having local interactions and no conserved densities. One of our main results is to reveal a generic mechanism setting the Thouless time in this context.

Our approach has been to develop a theory of local orbit pairing, centred on the properties of a transfer matrix that acts on pairs of local orbits and generates the average SFF. In large systems the average SFF is controlled by the leading eigenvalues of the average transfer matrix. We have calculated these eigenvalues and shown that there is a connection between the corresponding eigenvectors and the diagonal approximation to sums over pairs of many-body orbits. At fixed time and in the limit of large systems the dominant contributions to the SFF come

from orbits that are locally paired as in the diagonal approximation, but with distinct diagonal pairings in neighbouring spatial domains. This domain structure is associated with the exponential growth of the SFF with system size at fixed time, and the corresponding divergence of the Thouless time. Conversely, in a system of fixed large size there is a wide window of time $t_{\mathrm{Th}} \ll t \ll t_{\mathrm{H}}$ in which the pairing for the whole system forms a single domain, so the diagonal approximation is accurate.

We believe the structures we have uncovered are in a sense universal, with our results applying quite generally to lattice Floquet models with local interactions, and with the form of the deviations of the SFF from RMT governed by the cost of domain walls in the orbit pairing. On timescales much greater than the Floquet period we expect that systems in the same symmetry class which share a domain-wall cost, but which are different in microscopic detail, have similar spectral statistics. This kind of universality is familiar from studies of single-particle disordered conductors [see Sec. 1.2.2.2]. In that case the form of the departure of the spectral statistics from RMT on timescales $t < t_{\mathrm{Th}}$ is set by the diffusion constant, a coarse-grained quantity [62].

Our results should be compared against calculations within the diagonal approximation, in which the contributing many-body orbits are globally paired. In that approximation Haar-RFCs behave like Haar-random matrices, and the non-RMT behaviour we have observed in Haar-RFCs cannot be understood. There is, however, a separate mechanism, additional to the one involving pairing domains, that leads to non-RMT behaviour even from global pairing. To illustrate this we have introduced a generalised class of RFCs with gates which can be tuned from Haar-random to the identity. Away from the Haar case, these circuits generate within the diagonal approximation a Thouless time growing logarithmically with system size L. The mechanism behind this, observed in Ref. [90], is distinct from the domain wall contributions we have investigated here, and the effects are sub-dominant for ensembles in the vicinity of Haar randomness.

In interacting self-dual models, however, the diagonal approximation to the average SFF is exact. This is because the transfer matrix that generates it has

leading eigenvalues identically equal to unity, even at finite t [115, 117, 132]. Within our framework this implies an infinite domain wall tension, and therefore a vanishing contribution to the SFF from pairs of many-body orbits involving domain walls. Additionally, the diagonal propagator in the Ising basis has subleading eigenvalues that vanish at the self-dual point [90]. The vanishing of both the domain wall tension and the subleading eigenvalues of the diagonal propagator conspire to give an SFF equal to the RMT result. Perturbing away from the self-dual point causes the leading eigenvalues of the transfer matrix to deviate from unity [115], giving rise to behaviour similar to that observed here in Haar-RFCs, for example the exponential growth of the SFF with system size at fixed time.

Moving beyond the average SFF, we have initiated a similar investigation into the higher moments [see also Refs. [131] and [117]]. Our discussion highlights another source of deviations from RMT, associated with a freedom in the local pairing of the multiple copies of orbits which appear. The presence of domain walls in the pairing of copies of orbits enhances these higher moments, and consequently gives rise to non-Gaussian statistics of the SFF. We have discussed the connection between these domain walls and the entanglement membrane [20, 106–108]. Although our transfer matrix approach was here restricted to the first moment of the SFF, it is clear that one can construct analogous transfer matrices to generate the higher moments in generic Floquet models. Such an investigation would connect with recent work on rare-region effects. Weak links, for example, have been shown to play an important role in entanglement growth [83]. For the average transfer matrix generating the first moment of the SFF, the possibility of weak links would be captured by the decrease of the effective domain wall tension at late times.

The picture of local orbit pairing has also revealed strong correlations between the diagonal matrix elements of local observables. We have shown that, relative to the predictions of the ETH, these correlations grow exponentially with increasing system size. Our results represent a prominent correction to the ETH for Floquet models with local interactions. In the same way, we have argued that deviations from the

ETH arise in the off-diagonal matrix elements of non-local operators. These features grow exponentially with the support of the operator, as opposed to the system size.

Our focus has here been on Haar-RFCs, and so on strong coupling between the local degrees of freedom. Reducing the strength of the coupling, it is natural to expect larger deviations from RMT and ETH behaviour. In the ergodic phase, and for large L, there is nevertheless a wide window of time over which $\langle K(t) \rangle \simeq t$, corresponding to a single domain in the orbit pairing. There may, however, come a point when the diagonal approximation breaks down over all time and length scales. In that case the spectral statistics on the finest scales do not resemble those of random matrices. This is a known feature of the MBL phase, and in the next chapter we discuss this phenomenon in terms of paired paths.

3
Symmetry breaking

Broken symmetry has been a useful concept in the description of many phase transitions [5, 133, 134], extending even to the Anderson localisation of single-particle wavefunctions. In that context, it was a consideration of disorder-averaged Green's functions that showed how the corresponding delocalisation transition could be understood as symmetry breaking in a field theory [68]. There has since been substantial progress in the study of many-body localisation, the analogue of Anderson localisation in the presence of interactions [22–24, 26–28, 91]. The many-body localisation transition, however, has not so far been described in the language of symmetry breaking, nor has a local order parameter been identified.

The MBL phase is characterised by its failure to equilibrate, so falls outside the paradigm of statistical mechanics [27, 28]. It is to be contrasted with the ergodic phase, where in the thermodynamic limit local observables approach their equilibrium values under unitary dynamics [7, 8, 10, 11, 80]. This fundamental difference in dynamics is reflected in the spectral properties, and because the dynamics is in question it is natural to adopt a space-time description of the transition between the two phases. Such an approach has been central to recent advances in our understanding of the measurement transition [135–138] in many-body systems.

Focusing on the SFF, here we show how the transition from a MBL phase to an ergodic one can be viewed as symmetry breaking. The basic difference in behaviour of the SFF in the ergodic and MBL phases is as follows. For a chain of L sites with local Hilbert space dimension q, and without time-reversal symmetry, $\langle K(t)\rangle \simeq t$ in the ergodic phase for sufficiently large $t < q^L \equiv t_{\mathrm{H}}$. On the other hand, in the MBL phase $\langle K(t)\rangle \simeq q^L$ for $t \gtrsim q$. As in the previous chapter, our approach is to express $\langle K(t)\rangle$ in terms of an averaged transfer matrix that acts in the space direction. The average SFF is determined by the leading eigenvalues of this transfer matrix, and to draw connections with statistical mechanics it is useful to view it as a partition function for the orbit pairing degrees of freedom [see, for example, Eq. (2.13)]. In the MBL phase the leading transfer-matrix eigenvalue is unique, as in a symmetry-unbroken phase, while in the ergodic phase and at late times the leading eigenvalues are asymptotically degenerate, as in a system with degenerate symmetry-breaking phases. We identify the broken symmetry of the transfer matrix, introduce a local order parameter for the transition, and show that the associated correlation functions are long-ranged only in the ergodic phase.

This chapter is organised as follows. In Sec. 3.1 we introduce and characterise the RFCs used for numerical calculations. Following this, in Sec. 3.2 we investigate the spectral properties of the transfer matrix generating the average SFF. In Sec. 3.3 we define the order parameter, extract the correlation length, and connect the behaviour to known properties of the two phases. Then, in Sec. 3.4, we discuss the effect of applying a symmetry-breaking field. We present our conclusions in Sec. 3.5.

3.1 Model

As in Chapter 2 our focus is on brickwork RFCs constructed from unitary matrices $U_{x,x+1}$ that act on neighbouring pairs of sites $(x, x+1)$ [see Eq. (2.1)]. There, however, $U_{x,x+1}$ were chosen to be Haar random. So that we can tune across a many-body localisation transition, here we instead choose

$$U_{x,x+1} = [v_x \otimes v_{x+1}] \exp\left[i\pi J \Sigma_{x,x+1}\right] [u_x \otimes u_{x+1}], \tag{3.1}$$

where u_x and v_x are independent Haar-random $q \times q$ matrices which act on site x, $\Sigma_{x,x+1}$ is the two-site swap operator, and J is the coupling strength. From here on we restrict to $q = 2$. Our model is then a (Floquet) random-field spin-1/2 Heisenberg chain. It has no conserved densities, and does not have time-reversal symmetry. Furthermore, all points in the spectrum of the Floquet operator are statistically equivalent, precluding a mobility edge and removing the need for any unfolding procedure.

In this chapter we are concerned only with $0 \leq J \leq 0.3$. Note, however, that for $J = 1/2$ our model is dual unitary, falling into the non-interacting class of Refs. [132, 139]. In Secs. 3.1.1 and 3.1.2, using standard techniques, we present evidence for a many-body localisation transition in our model.

3.1.1 Spectral statistics

A useful probe of the short-range level statistics, aside from the SFF at large t, is the r-statistic [24], defined as follows. Writing $\Delta\theta_n = |\theta_{n+1} - \theta_n|$ with θ_n the ordered quasienergies of the Floquet operator, $r \equiv \min(\Delta\theta_n, \Delta\theta_{n+1}) / \max(\Delta\theta_n, \Delta\theta_{n+1})$. In the ergodic phase we expect the average $\langle r \rangle \simeq 0.60$, as for the CUE, whereas in the MBL phase we expect $\langle r \rangle = (2 \ln 2 - 1) \simeq 0.39$, the result when θ_n are uncorrelated random numbers. In Fig. 3.1(a) we show $\langle r \rangle$ for various L, computed from averages over the entire spectrum and over disorder, and in Fig. 3.1(b) we show $\langle K(t) \rangle$ for various J. In each case we find the expected crossover in behaviour.

3.1.2 Entanglement entropy

The difference between the ergodic and MBL phases is also evident in the entanglement structure of eigenstates [26, 33]. There is an additional difference in the growth of entanglement with time starting from unentangled states [25, 95–97]. We focus on the half-chain von-Neumann entanglement entropy $S_{L/2} = -\mathrm{Tr}[\rho_{L/2} \ln \rho_{L/2}]$ and in particular its disorder average $\langle S_{L/2} \rangle$, where $\rho_{L/2}$ is the reduced density matrix over half of a chain with periodic boundary conditions.

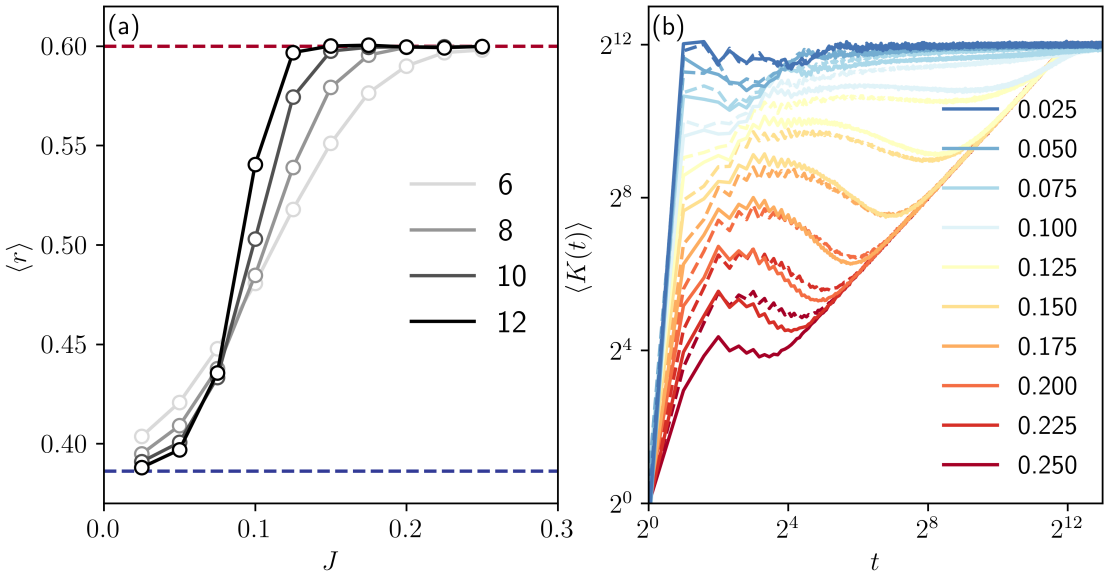

Figure 3.1: Spectral statistics with gates as in Eq. (3.1). (a) r-statistic versus J, for various L (legend) with periodic boundary conditions, compared with the result for the CUE (≈ 0.60, red dashed) and uncorrelated levels ($2\ln 2 - 1 \approx 0.39$, blue dashed). (b) Average SFF $\langle K(t) \rangle$ for $L = 12$ and various J (legend). Solid lines correspond to periodic boundary conditions, and dashed to open.

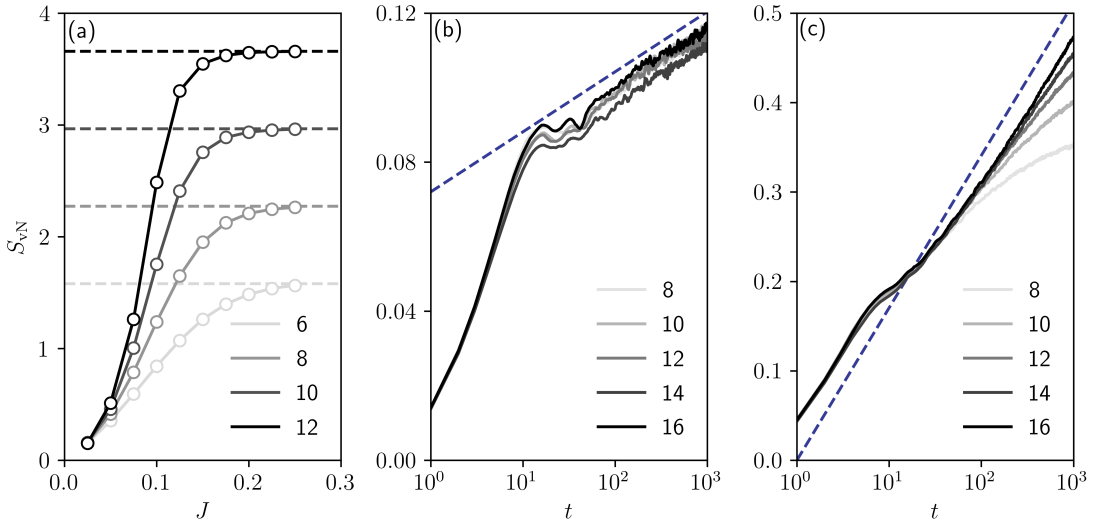

Figure 3.2: Disorder-averaged half-chain von Neumann entanglement entropy $\langle S_{L/2} \rangle$ for various L (legend). (a) $\langle S_{L/2} \rangle$ for eigenstates of W as a function of J, and for various L (legend). The Page value $(1/2)(L\ln 2 - 1)$ for random matrices, neglecting corrections of order $1/2^L$, is shown dashed. To the right we show the growth of $\langle S_{L/2} \rangle$ with time for (b) $J = 0.025$ and (c) $J = 0.05$, starting from $J = 0$ eigenstates. Dashed lines indicate logarithmic growth.

In Fig. 3.2(a) we show $\langle S_{L/2}\rangle$ for eigenstates of W, with an average over the spectrum and over disorder. At large J in the ergodic phase our results approach the Page value for random states $(1/2)(L\ln 2-1)+O(2^{-L/2})$, corresponding to volume-law entanglement [17]. For small J on the other hand we find an L-independent $S_{L/2}$, which in one dimension corresponds to area-law entanglement [33]. In Figs. 3.2(b) and (c) we then calculate $\langle S_{L/2}\rangle$ as a function of time t, starting from eigenstates of the decoupled system ($J=0$). In the MBL phase it is expected that $S_{L/2}$ increases logarithmically with t [25, 95–97], and in Figs. 3.2(b) and (c) we show that this is the behaviour for small J.

The results in this section indicate that our model is MBL for $J<J_c$ and ergodic for $J_c<J(<1/2)$, with the critical point $J_c\approx 0.07$. From here on we focus on behaviour deep within each of the two phases.

3.2 Transfer matrix

The transfer-matrix technique developed through the previous chapter can be summarised as follows. The spectrum of W is encoded in $\mathrm{Tr}W(t)$, and this trace can be expressed as a sum over closed paths, or many-body orbits, in the space of spin configurations. Spectral correlations, through the SFF $K(t)=|\mathrm{Tr}W(t)|^2$, are then determined by sums over pairs of such many-body orbits. We refer to those coming from $\mathrm{Tr}W(t)$ as forward orbits, and those coming from the conjugate as backward orbits. For Floquet systems with local interactions, this sum over pairs of forward and backward orbits can be generated by transfer matrices acting in the space direction. For randomness which is independently and identically distributed for different sites, $\langle K(t)\rangle$ is then determined by powers of a single averaged transfer matrix $\langle\mathcal{T}(t)\rangle$.

As before, in the regimes we consider only t leading eigenvalues of $\langle\mathcal{T}(t)\rangle$, $\lambda(\nu,t)$ for $\nu=0\ldots(t-1)$, control $\langle K(t)\rangle$. In the ergodic phase all $\lambda(\nu,t)$ are asymptotically degenerate at large t [see Fig. 2.14]. The corresponding eigenvectors break the symmetry of the transfer matrix under relative time-translation of orbits within a pair. This is because eigenvectors in sectors with $\nu\neq 0$ are not invariant under

$S^2 \otimes \mathbb{1}$ and $\mathbb{1} \otimes S^2$ [see Eqs. (2.16) and (2.23)]. In the MBL phase $\lambda(0,t)$ is the unique leading eigenvalue, and the corresponding eigenvector is invariant under relative translation of forward and backward orbits.

This behaviour of the eigenvalues can be related to the dependence of $\langle K(t)\rangle$ on t and L in the two phases as follows. First, note that in the limit of decoupled sites ($J = 0$) we have $\langle K(t)\rangle = \langle k(t)\rangle^L$, where $\langle k(t)\rangle$ is the average SFF for 2×2 Haar-random unitary matrices: $\langle k(1)\rangle = 1$ and $\langle k(t \geq 2)\rangle = 2$. The average SFF therefore saturates at 2^L for $t \geq 2$, and in the language of the transfer matrix there is one nonzero eigenvalue $\lambda(0,t) = \langle k(t)\rangle$. For small $J < J_c$ the other eigenvalues are nonzero, but $\lambda(0,t)$ remains dominant. By contrast, in the ergodic phase $\langle K(t)\rangle \simeq t$ for $t_{\rm Th} < t < t_{\rm H}$, where $t_{\rm Th}$ (a function of L) is the Thouless time. This arises from having t eigenvalues $\lambda(\nu,t) \simeq 1$ for all ν, as discussed in Chapter 2. To provide evidence for this behaviour of $\lambda(\nu,t)$ we use a variety of numerical approaches, as we now discuss.

3.2.1 Small t

At very short times we can construct the matrix $\langle \mathcal{T}(t)\rangle = \mathcal{S}\langle \mathcal{R}(t)\rangle$ and then probe it directly. Note that $\langle \mathcal{R}(t)\rangle$ has a different structure to its analogue for Haar-RFCs. Here it involves the $(2t)^{\rm th}$ moments of each of the four Haar-random 2×2 unitary matrices in Eq. (3.1), as well as tensor products of the operator $\exp[i\pi J\Sigma]$ and its conjugate.

To arrive at an explicit expression for $\langle \mathcal{R}(t)\rangle$, it is convenient to define a matrix $\mathcal{J}(t)$ with the same tensor-product structure as $\mathcal{R}_{x,x+1}(t)$ but without the single-site Haar-random matrices in Eq. (3.1). To find $\mathcal{J}(t)$ one first reshapes $\exp[i\pi J\Sigma]$ into an operator that acts on the space of paths in exactly the same way that U was reshaped into $\tilde{U}$ in Fig. 2.7. One then takes a tensor product of t copies of this operator, arriving at an object analogous to $\tilde{U}^{\otimes t}$, and finally computes the tensor product of this object with its conjugate. The result is $\mathcal{J}(t)$.

The individual matrices $\mathcal{R}_{x,x+1}(t)$ are products of (i) $\mathcal{J}(t)$ and (ii) tensor products of the single-site Haar-random matrices in Eq. (3.1). The average $\langle \mathcal{R}(t)\rangle$

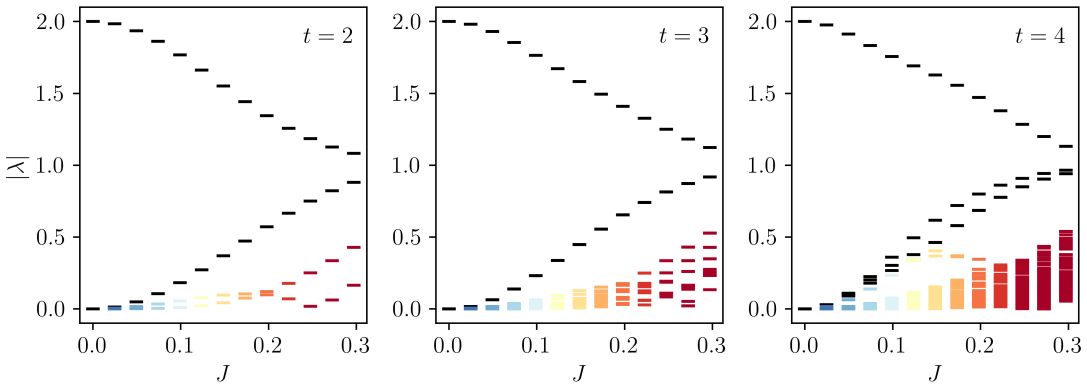

Figure 3.3: Absolute values of all nonzero eigenvalues λ of the transfer matrix $\langle \mathcal{T}(t) \rangle$ at times (a) $t = 2$ (b) $t = 3$ and (c) $t = 4$, with $J = 0.025m$ and $m = 0, 1 \ldots 12$. The t leading eigenvalues at each J, some of which are degenerate, are shown black. For these times the largest is unique and in the $\nu = 0$ sector.

is then a linear operator acting in the space spanned by the permutation states $|\sigma, \tau\rangle$, as in Sec. 2.6. Explicitly, we have

$$\langle \mathcal{R}(t) \rangle = \sum_{\substack{\sigma_u \tau_u \sigma_v \tau_v \\ \sigma'_u \tau'_u \sigma'_v \tau'_v}} \mathrm{Wg}(\sigma_u \tau_u^{-1}) \mathrm{Wg}(\sigma_v \tau_v^{-1}) \mathrm{Wg}(\sigma'_u \tau'^{-1}_u) \mathrm{Wg}(\sigma'_v \tau'^{-1}_v) \times |\sigma_u, \sigma_v\rangle \langle \tau_u, \tau_v | \mathcal{J}(t) | \tau'_u, \tau'_v \rangle \langle \sigma'_u, \sigma'_v | \,. \tag{3.2}$$

Evaluating the sum in Eq. (3.2) requires us to calculate the matrix elements $\langle \tau_u, \tau_v | \mathcal{J}(t) | \tau'_u, \tau'_v \rangle$, which depend on J. Because the operator $\mathcal{J}(t)$ is constructed from $\exp[i\pi J \Sigma] = \cos(\pi J)\mathbb{1} + i \sin(\pi J)\Sigma$, we can organise the various contributions to each matrix element $\langle \tau_u, \tau_v | \mathcal{J}(t) | \tau'_u, \tau'_v \rangle$ by the number of appearances of the Σ operator. For example, the contribution without any Σ operators is

$$\cos^{2t}(\pi J) \sum_{\substack{a_r b_r a'_r b'_r \\ a^*_r b^*_r a'^*_r b'^*_r}} \prod_{r=0}^{t-1} \delta_{a_r a^*_{\tau_u(r)}} \delta_{b_r b^*_{\tau_v(r)}} \delta_{a'_r a'^*_{\tau'_u(r)}} \delta_{b'_r b'^*_{\tau'_v(r)}} \delta_{a_r b_r} \delta_{a'_r b'_r} \delta_{a^*_r b^*_r} \delta_{a'^*_r b'^*_r}, \tag{3.3}$$

where the first four Kronecker δs come from the permutation states, and the others come from the reshaped identity operators in $\mathcal{J}(t)$. Summing over all indices in Eq. (3.3) we find a power of q, and this can be determined graphically via loop counting. For example, with $\tau_u = \tau_v = \tau'_u = \tau'_v = \mathbb{1}$, the contribution in Eq. (3.3) is $q^{2t} \cos^{2t}(\pi J)$. Repeating the above procedure for all possible locations of the Σ operators, we determine the matrix elements $\langle \tau_u, \tau_v | \mathcal{J}(t) | \tau'_u, \tau'_v \rangle$, and in this way compute $\langle \mathcal{R}(t) \rangle$ in Eq. (3.2).

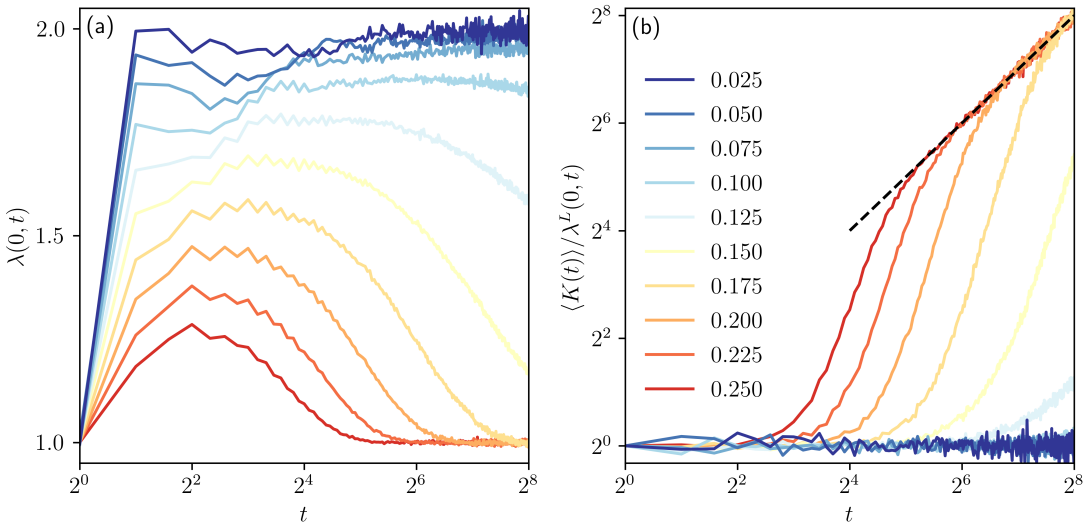

Figure 3.4: (a) $\lambda(0,t)$ from L-scaling of $\langle K(t)\rangle$ with open boundary conditions [see Eq. (2.32)]. (b) Ratio of $\langle K(t)\rangle$ with periodic boundary conditions, and with $L = 12$, to the contribution of only the $\nu = 0$ sector, $\lambda^L(0,t)$, from (a). The black dashed line shows t, and J is on the legend.

To determine $\langle \mathcal{T}(t)\rangle$ we require the action of $\mathcal{S}$ on the permutation states, and this was given in Sec. 2.6. After rewriting $\langle \mathcal{T}(t)\rangle$ in an orthonormal basis, we diagonalise it using standard numerical routines. In Fig. 3.3 we show the magnitudes of all of the nonzero eigenvalues of $\langle \mathcal{T}(t)\rangle$ for $0 \leq J \leq 0.3$ and $t = 2, 3, 4$. Even for these small values of t, increasing J causes the separation between the $\lambda(\nu, t)$ to decrease, and the gap between them and all other eigenvalues to increase. For these times $\lambda(0,t) > 1$, whereas $\lambda(\nu \neq 0, t) < 1$, with $\lambda(0,t) \gg \lambda(\nu \neq 0, t)$ at small J.

3.2.2 Large t

The asymptotic behaviour becomes clear only at much larger t, where diagonalisation of $\langle \mathcal{T}(t)\rangle$ is computationally too demanding. Instead, we compare $\langle K(t)\rangle$ with open and periodic boundary conditions. As discussed in connection with Eq. (2.28), with open boundary conditions $\langle K(t)\rangle$ has contributions from only the $\nu = 0$ sector. With periodic boundary conditions all sectors contribute.

In particular, for open boundaries and for large L we have

$$\langle K(t)\rangle = \lambda^{L-1}(0,t)\,\langle \mathcal{B}_L|0,t;R\rangle\,\langle 0,t;L|\mathcal{B}_R\rangle + \ldots$$

from Eq. (2.32). The scaling of $\langle K(t)\rangle$ with L at fixed t gives $\lambda(0,t)$, and the results are shown in Fig. 3.4(a) for various J and for $t \leq 2^8$ [c.f. results for Haar-RFCs in Fig. 2.9(a)]. At large t and for small J, $\lambda(0,t) \simeq 2$, while for large J, $\lambda(0,t) \simeq 1$. With periodic boundary conditions we have

$$\langle K(t)\rangle = \sum_{\nu=0}^{t-1} \lambda^L(\nu,t) + \dots$$

from Eq. (2.41) [see also Fig. 2.15]. For a transfer matrix $\langle \mathcal{T}(t)\rangle$ with t degenerate leading eigenvalues $\lambda(\nu,t) = 1$, and all others negligible, we expect $\langle K(t)\rangle/\lambda^L(0,t) = t$. If only one eigenvalue dominates, and it is in the symmetric $\nu = 0$ sector, $\langle K(t)\rangle/\lambda^L(0,t) = 1$. This behaviour, in the ergodic and MBL phases, respectively, is shown in Fig. 3.4(b). The results in Fig. 3.4 indicate that the transition from the MBL to the ergodic phase can be viewed as symmetry breaking. We also see that, decreasing J in the ergodic phase, RMT behaviour sets in at ever later times: the Thouless time $t_{\rm Th}$ diverges as J_c is approached.

3.3 Local order parameter

To probe symmetry breaking more directly, we introduce a local order parameter. The starting point is an expression for the SFF $K(t) = |{\rm Tr}W(t)|^2$ as a sum over pairs of many-body orbits, expressed in a local basis such as the eigenstates of the Pauli operators σ_x^z for sites $x = 0 \dots (L-1)$. We can then write ${\rm Tr}W(t) = \sum_P A_P$, where P are closed paths of t steps in the space of σ^z eigenstates. The complex amplitudes A_P are then products of t matrix elements of W in this basis, and the SFF is

$$K(t) = \sum_{PQ} A_P A_Q^*. \tag{3.4}$$

The weights $A_P A_Q^*$ associated with each orbit pair P, Q are complex, although $K(t)$ is real and non-negative. We are interested in averaged properties of the sum over orbit pairs in Eq. (3.4).

In Sec. 3.3.1 we introduce the order parameter, and contrast it with the quantity studied in Sec. 2.5.3. In Sec. 3.3.2 we show how to compute the two-point function, and relate it to spectral properties of the Floquet operator. In Sec. 3.3.3 we relate

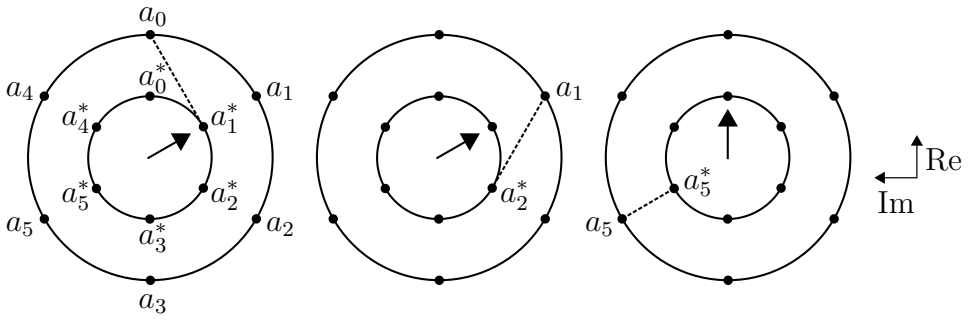

Figure 3.5: Contributions to the clock order parameter for a single orbit pair. Here $t = 6$ and we show just 3 out of the $t^2 = 36$ terms in Eq. (3.5). The states in the respective forward and backward orbits at (integer) time r are a_r and a_r^*. Dashed lines represent Kronecker δs, and the central arrows represent the phasor $e^{-2\pi i s/t}$ for integer s, with the real axis vertical. The left and central diagrams show contributions proportional to $e^{-2\pi i/t}$, and the right diagram shows a contribution along the real axis.

the correlation length $\xi(t)$ to the spectrum of $\langle \mathcal{T}(t) \rangle$ and extract it numerically. We will see that, in both phases and at large distances, the two-point function decays exponentially at finite t, and also that $\xi(t)$ increases with t for all J. Sec. 3.3.4 discusses how the behaviour of the two-point function in the MBL phase can be understood in terms of resonances between LIOM configurations.

3.3.1 Clock operator

The relevant symmetry, time-translation of backward orbits with respect to forward orbits, is at time t the symmetry of a t-state clock model. We can therefore represent the order parameter by a complex number. For example, in a standard clock model with states $s = 0 \ldots (t-1)$, the order parameter is $e^{-2\pi i s/t}$. Here we are concerned with the pairing of single-site orbits, so we define a diagonal operator $\mathcal{C}$ acting in the space of single-site orbit pairs

$$\mathcal{C}|a_0 b_0 \ldots\rangle \otimes |a_0^* b_0^* \ldots\rangle = \frac{2}{t} \sum_{p,r=0}^{t-1} \delta_{a_p a_r^*} e^{2\pi i (p-r)/t} |a_0 b_0 \ldots\rangle \otimes |a_0^* b_0^* \ldots\rangle. \tag{3.5}$$

The diagonal matrix elements of $\mathcal{C}$ in this basis are the values of the order parameter for each orbit pair, and three of the terms in the sum on the right-hand side of Eq. (3.5) are illustrated in Fig. 3.5. More generally we should replace the prefactor 2 by the local Hilbert space dimension q, so that when $\mathcal{C}$ acts on paired states $|s\rangle$ it returns $e^{-2\pi i s/t}$.

Using $\mathcal{C}$ we can assign the many-body orbit pairs in Eq. (3.4) values of the order parameter at each site x. For orbits P, Q we write these numbers as $\mathcal{C}_{P,Q}(x)$. The one-point function is naturally defined as

$$\mathcal{O}_1(x,t) = \frac{\langle \sum_{PQ} A_P A_Q^* \mathcal{C}_{P,Q}(x) \rangle}{\langle \sum_{PQ} A_P A_Q^* \rangle}, \tag{3.6}$$

where we have averaged the numerator and denominator separately so that $\mathcal{O}_1(x,t)$ probes the same average of the sum over orbit pairs as $\langle K(t) \rangle$ [see also Eq. (2.47)].

To write $\mathcal{O}_1(x,t)$ in terms of the evolution operator we use $2\delta_{a_p a_r^*} = (\sigma^z_{a_p a_p} \sigma^z_{a_r^* a_r^*} + 1)$ and find

$$\mathcal{O}_1(x,t) \times \langle K(t) \rangle = \frac{1}{t} \sum_{p,r} e^{2\pi i (p-r)/t} \langle \mathrm{Tr}[W(t-p)\sigma_x^z W(p)] \mathrm{Tr}[W(t-r)\sigma_x^z W(r)]^* \rangle.$$

Since $W(p)W(t-p) = W(t)$ for p integer, the sum over p ensures that the one-point function $\mathcal{O}_1(x,t) = 0$. This is to be expected, since our model has no symmetry-breaking fields or boundary conditions.

The discussion in this section should be contrasted with that in Sec. 2.5.3. There we defined a real scalar quantity as a probe for a particular pairing domain in the ergodic phase. Our focus was on the behaviour of that quantity in systems subjected to a variety of symmetry-breaking boundary conditions. Here we are instead concerned with correlations of the complex scalar order parameter defined by Eq. (3.5).

3.3.2 Two-point function

To study correlations of $\mathcal{C}$ in the averaged sum over orbit pairs that generates the SFF we require a two-point function $\mathcal{O}_2(x,y,t)$. This comes from inserting the operators $\mathcal{C}^*$ and $\mathcal{C}$ at the sites x and y, respectively. We expect $\mathcal{O}_2(x,y,t)$ to show long-range correlations in a symmetry-broken phase. Schematically,

$$\mathcal{O}_2(x,y,t) = \frac{\langle \sum_{PQ} A_P A_Q^* \mathcal{C}^*_{P,Q}(x) \mathcal{C}_{P,Q}(y) \rangle}{\langle \sum_{PQ} A_P A_Q^* \rangle}. \tag{3.7}$$

To find an expression in terms of $W(t)$ we must sum over p, r [see Eq. (3.5)] at each of the sites x and y. The result has the form

$$\mathcal{O}_2(x,y,t) \times \langle K(t) \rangle = \frac{1}{t^2} \sum_{p_x, r_x, p_y, r_y = 0}^{t-1} e^{-2\pi i (p_x - r_x - p_y + r_y)} M(p_x, p_y) M^*(r_x, r_y), \tag{3.8}$$

where $M(p_x, p_y)$ is related to a trace over $\mathrm{Tr}W(t)$ but with an insertion of σ_x^z at time step p_x, and σ_y^z at time step p_y. For example, with $p_x > p_y$ we have $M(p_x, p_y) = \mathrm{Tr}[W(t - p_x + p_y)\sigma_x^z W(p_x - p_y)\sigma_y^z]$. This gives

$$\mathcal{O}_2(x, y, t) \times \langle K(t) \rangle = \Big\langle \Big| \sum_{r=0}^{t-1} \mathrm{Tr}[W(t - r)\sigma_x^z W(r)\sigma_y^z] e^{2\pi i r/t} \Big|^2 \Big\rangle. \tag{3.9}$$

Writing $W(t) = \sum_n e^{i\theta_n t}|n\rangle\langle n|$ and evaluating the sum over r in Eq. (3.9), we find

$$\mathcal{O}_2(x, y, t) \times \langle K(t) \rangle = \Big\langle \Big| \sum_{mn} G_{mn}(t) \langle n|\sigma_x^z|m\rangle\langle m|\sigma_y^z|n\rangle \Big|^2 \Big\rangle, \tag{3.10}$$

where $G_{mn}(t) = e^{i\theta_n t} \sum_{r=0}^{t-1} e^{i(\theta_m - \theta_n + 2\pi/t)r}$ selects for pairs of levels separated in quasienergy by $(\theta_n - \theta_m) \sim 2\pi/t$.

From the perspective offered by Eq. (3.10), in the MBL phase we expect $\mathcal{O}_2(x, y, t)$ to be small for large $|x - y|$. This is because pairs of eigenstates $|n\rangle$ and $|m\rangle$ for which $\langle n|\sigma_x^z|m\rangle$ and $\langle m|\sigma_y^z|n\rangle$ are both large are rare [see also Sec. 3.3.4]. Conversely, modelling these matrix elements using the ETH, expected to be applicable in the ergodic phase for $t \gg t_{\mathrm{Th}}$, we find $\mathcal{O}_2(x, y, t) = 1$ for $x \neq y$ and $t \ll t_{\mathrm{H}}$. A simple way to see this is to replace W with a $2^L \times 2^L$ Haar-random unitary matrix. Then for $t \ll 2^L$ the right-hand side of Eq. (3.9) can be calculated using standard techniques [46]. Expanding the modulus-squared sum in the average in Eq. (3.9) we have t^2 terms. Averaging using Eq. (1.3), only the t diagonal terms contribute in the limit of large 2^L [see above Eq. (1.7)]. Each of these gives unity, and because $\langle K(t) \rangle = t$, we find $\mathcal{O}_2(x, y, t) = 1$.

In Fig. 3.6 we test these suggestions for the behaviour of $\mathcal{O}_2(x, y, t)$ against numerics. There is a rapid decay with $|x - y|$ in the MBL phase ($J = 0.05$) for all values of t shown, whereas $\mathcal{O}_2(x, y, t)$ is approximately independent of $|x - y|$ in the ergodic phase ($J = 0.25$). It is also clear that at fixed $|x - y|$ the two-point function increases with t in the MBL phase. We elaborate on this in Sec. 3.3.4.

3.3.3 Correlation length

As discussed in Sec. 3.2, symmetry breaking is manifest in the spectrum of $\langle \mathcal{T}(t) \rangle$, so we must ask which aspects are probed by the two-point function. With periodic

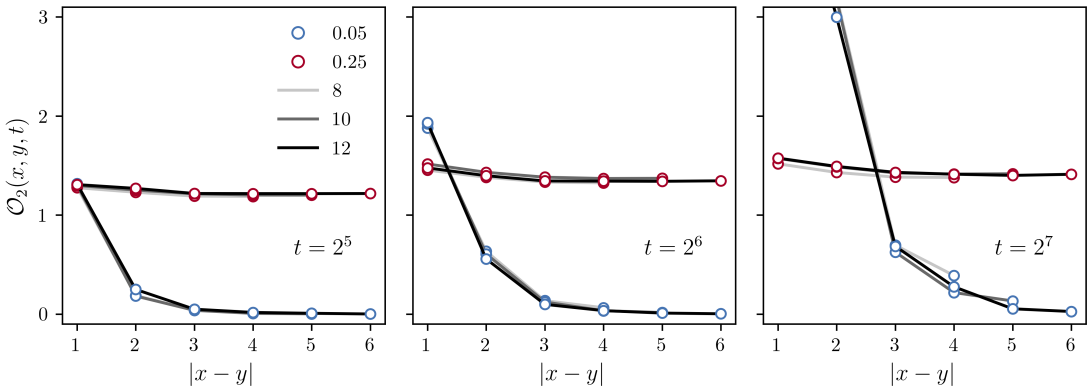

Figure 3.6: Two-point function for the pairing of orbits, $\mathcal{O}_2(x,y,t)$ [Eq. (3.9)], in the MBL ($J = 0.05$, blue circles) and ergodic ($J = 0.25$, red circles) phases. Different panels show different t, and line shades indicate L (legend).

boundary conditions, and $|x-y|$ even, we have

$$\mathcal{O}_2(x,y,t) = \frac{\mathrm{tr}\left[\mathcal{S}^{-L}(\mathcal{S}\langle\mathcal{R}\rangle)^{L-|x-y|}\mathcal{C}^*(\mathcal{S}\langle\mathcal{R}\rangle)^{|x-y|}\mathcal{C}\right]}{\mathrm{tr}\left[\mathcal{S}^{-L}(\mathcal{S}\langle\mathcal{R}\rangle)^{L}\right]}, \tag{3.11}$$

where $|x-y|$ is defined modulo L. This expression is simplified considerably using (i) the spectral decomposition of the transfer matrix and (ii) a selection rule on the matrix elements of $\mathcal{C}$ in the space of orbit pairs, which comes from

$$(S^2 \otimes 1)\mathcal{C}(S^{-2} \otimes 1) = e^{2\pi i/t}\mathcal{C}. \tag{3.12}$$

Also, at any finite t we have $\lambda(0,t) > \lambda(\nu \neq 0, t)$, so taking the thermodynamic limit $L \to \infty$ with t and $|x-y|$ fixed we find

$$\mathcal{O}_2(x,y,t) = [\lambda(1,t)/\lambda(0,t)]^{|x-y|}F(t) + \ldots, \tag{3.13}$$

where the ellipses denote the contributions of subleading eigenvalues, which are suppressed for large $|x-y|$. Here $F(t)$ is a (real) product of matrix elements that depends only on the parity of $|x-y|$. With $|x-y|$ even $F(t) = \langle 0,t;L|\mathcal{C}^*|1,t;R\rangle\langle 1,t;L|\mathcal{C}|0,t;R\rangle$, whereas with $|x-y|$ odd $F(t) = |\langle 1,t;L|\mathcal{C}|0,t;R\rangle|^2$. Eqs. (3.10) and (3.13) provide another relation (in addition to e.g. Eq. (2.41)) between the spectral properties of the transfer matrix and of the Floquet operators.

From Eq. (3.13) it is clear that the two-point function decays over a lengthscale

$$\xi(t) = \left[\ln[\lambda(0,t)/\lambda(1,t)]\right]^{-1}. \tag{3.14}$$

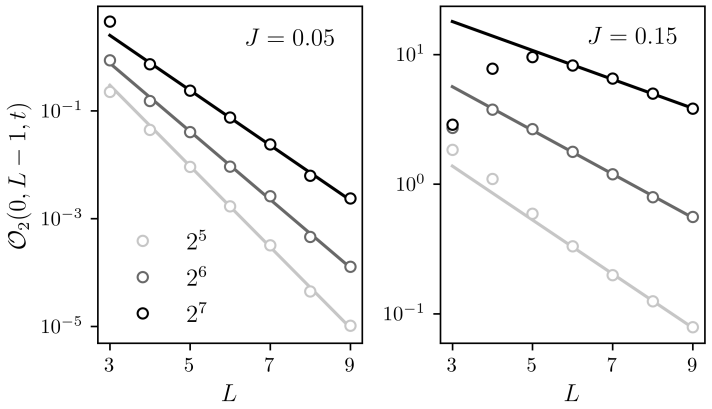

Figure 3.7: Extracting $\xi(t)$ from $\mathcal{O}_2(0, L-1, t)$ with open boundary conditions [see Eq. (3.15)]. Here we show $J = 0.05$ (left) and $J = 0.15$ (right), for various t (legend).

This is the correlation length for the pairing of local orbits in the sum generating the average SFF. To extract $\xi(t)$ it is convenient to consider a system with open boundary conditions, and with $x = 0$ and $y = (L-1)$ the two end sites. In this setup we have

$$\mathcal{O}_2(0, L-1, t) = [\lambda(1,t)/\lambda(0,t)]^{L-1} \frac{\langle \mathcal{B}_L|\mathcal{C}^*|1,t;R\rangle\langle 1,t;L|\mathcal{C}|\mathcal{B}_R\rangle}{\langle \mathcal{B}_L|0,t;R\rangle\langle 0,t;L|\mathcal{B}_R\rangle} + \dots \tag{3.15}$$

for large L. Although the factor multiplying $e^{-(L-1)/\xi(t)}$ in Eq. (3.15) is not equal to $F(t)$, by following the scaling of $\mathcal{O}_2(0, L-1, t)$ with L at fixed t we can extract $\xi(t)$, as shown in Fig. 3.7. The behaviour of $\xi(t)$ is shown for various J in Fig. 3.8. In the ergodic phase we find a rapid divergence of $\xi(t)$ with t. This leads to order in the orbit pairing across a finite system at times $t_{\rm Th} < t < t_{\rm H} = 2^L$, and so to RMT spectral statistics $\langle K(t)\rangle \simeq t$ within this window.

On the other hand, in the MBL phase $\xi(t)$ increases much more slowly. As we discuss in the next section, there we anticipate logarithmic growth $\xi(t) \sim \zeta \ln t$ with $\zeta < 1/\ln 2$. From this we see that the correlation length $\xi(t)$ remains smaller than the system size L up to at least the Heisenberg time; order in the orbit pairing is not established even at $t = 2^L$.

3.3.4 Resonances

Here we connect the observed behaviour of $\mathcal{O}_2(x, y, t)$ to known features of the MBL phase. Expanding the modulus square in Eq. (3.10) we find a sum over all sets of four eigenstates, so there are several quasienergy differences to keep track

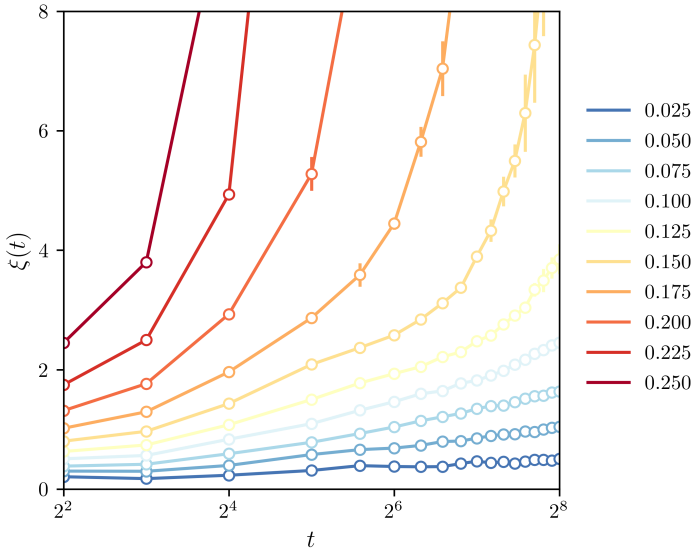

Figure 3.8: Correlation length $\xi(t)$ [Eq. (3.14)] extracted from L-scaling as in Fig. 3.7, here for various J (legend). $\xi(t)$ increases for all J [see also Fig. 3.9], but deep in the MBL phase $\xi(t) \ll L$ for $t < 2^L$. In the ergodic phase $\xi(t) \gg L$ for $t_{\rm Th} \ll t < 2^L$.

of. A considerable simplification comes from neglecting all but the 'diagonal' terms in the multiple sum over eigenstates. In this approximation

$$\mathcal{O}_2(x,y,t) \times \langle K(t)\rangle \simeq \Big\langle \sum_{mn} |G_{mn}(t)|^2 |\langle n|\sigma_x^z|m\rangle|^2 |\langle n|\sigma_y^z|m\rangle|^2 \Big\rangle, \tag{3.16}$$

which is a sum over non-negative terms. In a Floquet system we expect each term to depend only on one quasienergy difference $|\theta_n - \theta_m|$. We test the accuracy of this approximation in Fig. 3.9, and find excellent agreement between Eqs. (3.10) and (3.16). Note that at late times (not shown in Fig. 3.6) the dependence of $\mathcal{O}_2(x,y,t)$ on separation $|x-y|$ is much weaker, as expected for a correlation length $\xi(t)$ increasing with t.

From Fig. 3.9, at late times in the MBL phase $\mathcal{O}_2(x,y,t) \sim t^\alpha$ with $\alpha < 2$. This is most easily understood in the quasienergy domain, so it is convenient to define

$$A(x,y,\omega) \equiv \sum_{nm} \delta(\omega - \theta_n + \theta_m) |\langle n|\sigma_x^z|m\rangle|^2 |\langle n|\sigma_y^z|m\rangle|^2, \tag{3.17}$$

which is related to our approximate form for $\mathcal{O}_2(x,y,t)$ in Eq. (3.16) via

$$\mathcal{O}_2(x,y,t) \times \langle K(t)\rangle \simeq \int d\omega g(\omega,t) \langle A(x,y,\omega)\rangle, \tag{3.18}$$

where $g(\omega,t) = |\sum_{r=0}^{t-1} e^{i(\omega - 2\pi/t)r}|^2$. At late times $t \gg 1$ and low frequencies $\omega \ll 1$ we have $g(\omega,t) \simeq t^2 \mathrm{sinc}^2\big[\omega t/2 - \pi\big]$. Therefore, the two-point function at time t

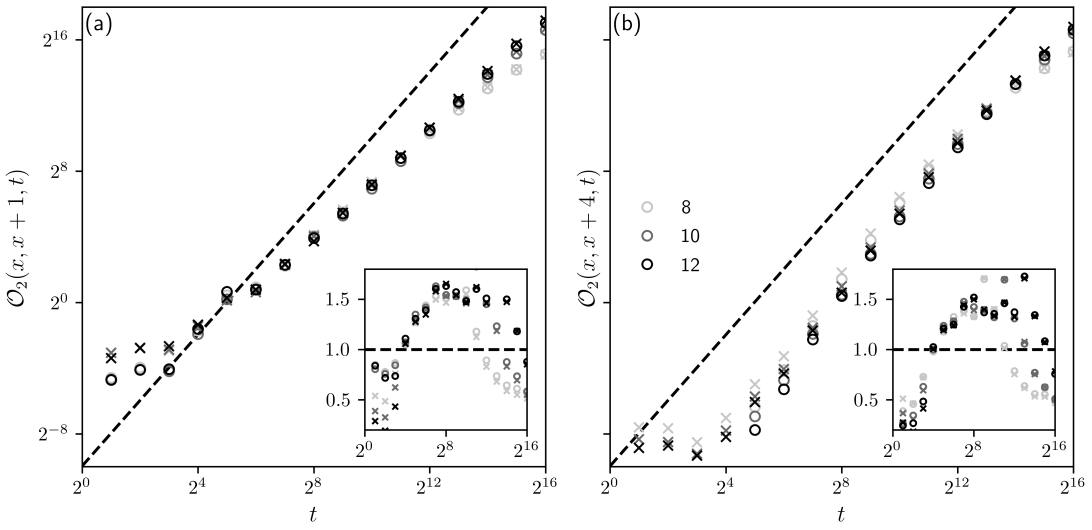

Figure 3.9: Time-dependence of the two-point function $\mathcal{O}_2(x, y, t)$ [open circles] compared with the approximation in Eq. (3.16) [crosses]. Main panels show behaviour in the MBL phase ($J = 0.05$) and insets behaviour in the ergodic phase ($J = 0.25$). In (a) $|x - y| = 1$, and in (b) $|x - y| = 4$. The legend shows L, and we use periodic boundary conditions. Dashed lines indicate power-law growth $\sim t^2$ (main panels), and unity (insets).

is dominated by $\langle A(x, y, \omega)\rangle$ at $\omega \simeq 2\pi/t$. Based on the behaviour of $\mathcal{O}_2(x, y, t)$ we expect $\langle A(x, y, \omega)\rangle$ to behave as $\omega^{-\gamma}$ at low frequencies, with $\gamma = \alpha - 1 < 1$. This is verified by numerical calculations in Fig. 3.10.

The low-frequency power-law growth of matrix elements of local operators is a known feature of the MBL phase [126, 140–143], having its origin in rare resonances between LIOM configurations. Resonances over lengthscales ℓ are expected to occur on energy scales $\omega \sim e^{-\ell/\zeta}$, where the decay length $\zeta < 1/\ln 2$[1]. Additionally, resonances are associated with matrix elements of local operators $\langle n|\sigma_x^z|m\rangle$ which can be of order unity when x is in the resonant region.

Certain quantities, including $\langle A(x, y, \omega)\rangle$ [143], are dominated by contributions from resonant pairs of LIOM configurations. On energy scale ω these occur over lengthscales $\ell \sim \zeta \ln(1/\omega)$, while the number of possible resonances on this lengthscale grows as $2^\ell \sim \omega^{-\zeta \ln 2}$. From Eq. (3.16) we therefore expect $\langle A(x, y, \omega)\rangle \sim \omega^{-\zeta \ln 2}$ provided $\zeta \ln(1/\omega) > |x - y|$. Note that this suggests $\xi(t) \sim \zeta \ln t$, the typical lengthscale of resonances at frequency $\omega \simeq 2\pi/t$. We

[1]This condition on ζ is associated with the avalanche instability of the MBL phase [144]

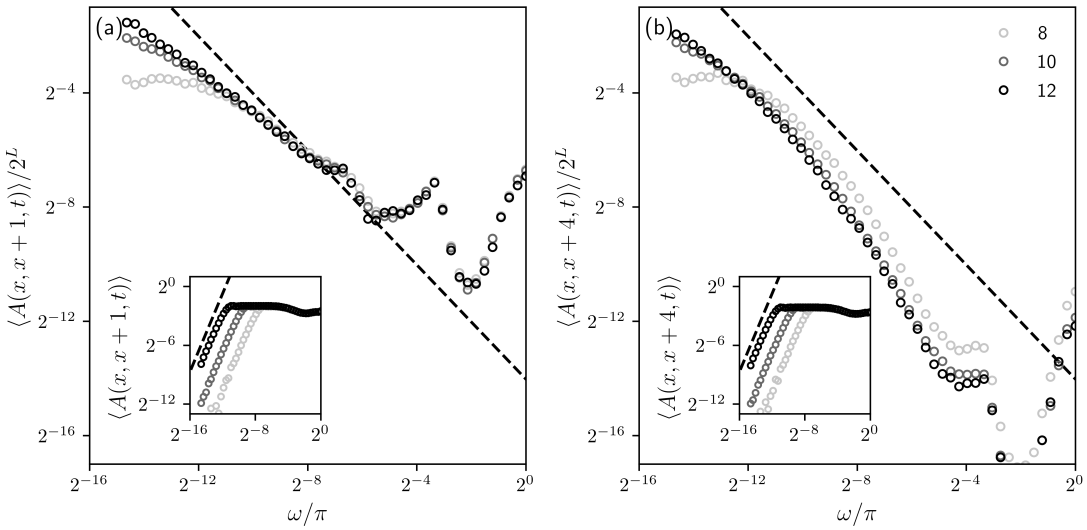

Figure 3.10: $\langle A(x,y,\omega)\rangle$ [Eq. (3.17)]; figure organisation as in Fig. 3.9. Dashed lines indicate $\sim 1/\omega$ (main panels, $J = 0.05$), and the ω^2 level repulsion expected for $\omega \lesssim (2\pi)/2^L$ in the ergodic phase (insets, $J = 0.25$). The legend shows L.

also see that the exponent $\gamma = \zeta \ln 2$. In this way the power-law increase of the two-point function $\mathcal{O}_2(x,y,t) \sim t^\alpha$ (with $\alpha = \gamma + 1 < 2$) observed in Fig. 3.9 can be understood as arising from low-frequency resonances in the MBL phase.

3.4 Symmetry-breaking fields

The previous section focused on correlations of the clock order parameter. In the ergodic phase there are long-range correlations relative to L at times $t < t_{\rm H}$, whereas in the MBL phase the correlations are short ranged. Another way to investigate the sum over many-body orbit pairs generating the SFF is to consider the response to a symmetry-breaking field. For example at time t, and with t/b and b both integers, a natural choice is to break the symmetry locally from t-fold to t/b-fold. In the symmetry-broken phase of a classical clock model, one expects this to reduce the partition function by a factor b. In the symmetric phase one expects a much weaker response.

Locally breaking the symmetry from t-fold to t/b-fold can be achieved in practice by locally punctuating the time evolution with 2×2 Haar-random unitary matrices which repeat only after b time steps. For example, breaking the symmetry with $b = 2$

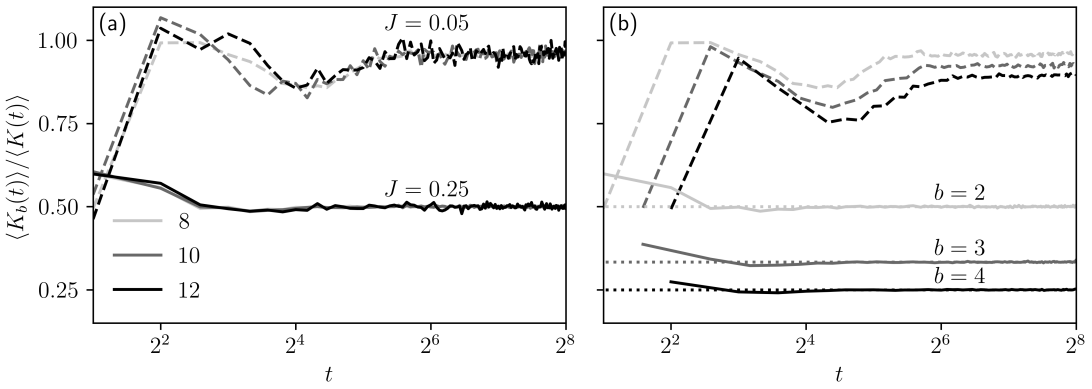

Figure 3.11: Response of the average SFF to local symmetry-breaking fields in the MBL ($J = 0.05$, dashed) and ergodic ($J = 0.25$, solid) phases. (a) $\langle K_2(t)\rangle/\langle K(t)\rangle$ [Eq. (3.19)] for various L (legend). (b) $\langle K_b(t)\rangle/\langle K(t)\rangle$ for $L = 8$ and $b = 2, 3, 4$ as indicated. Horizontal dotted lines show $1/b$, the value expected in the symmetry-broken phase. $\langle K_b(t)\rangle$ is defined only for t an integer multiple of b, and here we use periodic boundary conditions.

at just one site x, the evolution operator for t even is changed from $W(t) = W^t$ to $(W^{(2)}W^{(1)})^{t/2}$, where $W^{(1)}$ differs from $W^{(2)}$ only in the realisation of the randomness at x. Since $W^{(2)}W^{(1)}$ is simply another Floquet operator, but now for evolution with period 2, it is natural to expect that in the ergodic phase the new SFF at time t (corresponding to $t/2$ Floquet periods) is $t/2$. More generally, we expect

$$\langle K_b(t)\rangle = \left\langle \left| \mathrm{Tr}[(W^{(b)} \dots W^{(2)}W^{(1)})^{t/b}] \right|^2 \right\rangle \simeq t/b \tag{3.19}$$

in the ergodic phase and for large $t < 2^L$. In the limit of decoupled sites ($J = 0$) one instead finds, for $t \geq 2b$, that $\langle K_b(t)\rangle = \langle K(t)\rangle$. For small $J < J_c$ in the MBL phase we therefore expect $\langle K_b(t)\rangle \simeq \langle K(t)\rangle$. In Fig. 3.11 we show $\langle K_b(t)\rangle/\langle K(t)\rangle$ as a function of t for various b and L, and find excellent agreement with the above predictions. There is a clear difference in response between the ergodic and MBL phases, demonstrating a form of long-range rigidity in the former which arises from the broken symmetry.

3.5 Conclusion

In many-body quantum systems with local interactions there are generically two phases of unitary dynamics: ergodic and, in the presence of disorder, MBL. The

transition between them has sharp signatures in the spectrum of the evolution operator, both in the traditional Hamiltonian setting, and also in the Floquet models we consider. Here our focus has been on differences in the spectral statistics between the two phases, using the perspective offered by the transfer-matrix framework developed in Chapter 2. This framework emphasises the role of locality and provides a controlled way to treat disorder.

Our main result is to show how the transition from a MBL phase to an ergodic one can be viewed as symmetry breaking in an effective clock model. In the ergodic phase, the transfer matrix generating the average SFF has t leading eigenvalues which are asymptotically degenerate at large t, and these are associated with symmetry-breaking eigenvectors. The MBL phase on the other hand is characterised by a transfer matrix with one dominant eigenvalue, and the corresponding eigenvector breaks no symmetries of the transfer matrix. We have defined a local order parameter for the transition, and have shown that the behaviour of the SFF in the ergodic phase is associated with long-range correlations of this order parameter.

The identification of order and disorder is subtle in this setting. In classical statistical mechanics there is no true long-range order in one dimension and at finite temperature. In the models we consider there is no notion of temperature, but we have a correlation length $\xi(t)$ that diverges only for $t \to \infty$. This means that if we first take the thermodynamic limit $L \to \infty$, long-range order is not established at any finite t. Equivalently, in the thermodynamic limit and for general values of J, we do not find $\langle K(t) \rangle \simeq t$ for any finite t. It is important to recognise, however, that for finite L a given Floquet operator W has only 2^L quasienergies. Although $\mathrm{Tr}W(t)$ is defined for all integer t there are at most 2^L degrees of freedom, so no more than 2^L of the traces $\mathrm{Tr}W(t)$ are linearly independent. On physical grounds we restrict ourselves to those with $t \leq t_{\mathrm{H}} \equiv 2^L$ since this is set by the inverse level spacing. Whether the phase is ordered or disordered therefore requires consideration of both t and L. For finite L, order is established over the entire system at a time $t < 2^L$ only for large J, when the correlation length $\xi(t)$ grows quickly. Then, taking the limit $t, L \to \infty$ with $t = f2^L$ and $0 < f < 1$, we find

$\langle K(t)\rangle = t$ over a wide window of time. This is the ergodic phase, and $\langle K(t)\rangle = t$ corresponds to a sum over t ground states of the clock model.

At this point it is useful to review the systems we have encountered, and in particular the dependence of $t_{\rm Th}$ on L. From the above we see that $t_{\rm Th}$ is essentially the time at which $\xi(t)$ reaches L. In the RPM [Eq. (2.3)] with large q the eigenvalues $\lambda(\nu, t)$ approach unity as $e^{-\varepsilon t}$, where ε is time-independent [109]. In a finite system we therefore find order in the orbit pairing beyond $t_{\rm Th} \sim \ln L/\varepsilon$. For Haar-RFCs we have shown in Fig. 2.9(c) that the effective ε decreases with time. The increase of $t_{\rm Th}$ with L is nevertheless slower than that of $t_{\rm H}$. We find similar behaviour in the model considered in this chapter provided J is sufficiently large. For small J, we instead have $\lambda^L(0, t) \gg \lambda^L(\nu \neq 0, t)$ for $t < t_{\rm H}$ [see Fig. 3.4].

In the MBL phase, we have argued that correlations in the pairing of orbits provide information on resonances between LIOM configurations. These resonances are understood to be closely related to the rare-region effects that control behaviour near the transition [140, 144, 145]. In contrast, here we have focused only on an averaged quantity, $\langle K(t)\rangle$, which nevertheless captures the distinction between the MBL and ergodic phases. In the ergodic phase information on rare regions is contained in the form of the approach of $\lambda(\nu, t)$ to unity at late times, as we have discussed in connection with Fig. 2.9(c). To understand rare-region effects in more detail, a natural next step is to consider higher moments of the SFF. For example, in Sec. 2.8 we have shown that $\langle K^2(t)\rangle$ exceeds $2\langle K(t)\rangle^2$ at early times in the ergodic phase. For decoupled sites, one instead finds $\langle K^2(t)\rangle = 2^L\langle K(t)\rangle^2$. Alternatively, one can study products of unaveraged transfer matrices [131].

We have also introduced the notion of a symmetry-breaking field as a tool for the numerical study of sums over pairs of Fock-space paths. The paths contributing to ${\rm Tr}W(t)$ have amplitudes with time-translation symmetry simply because the evolution operator is the same for each step. Our approach was to apply the symmetry-breaking field locally. One expects this to affect degrees of freedom within a correlation length of the field, so the response of $\langle K(t)\rangle$ is a natural probe of symmetry breaking.

In closing we discuss a parallel with work preceding the scaling theory of the Anderson localisation transition [75]. As we have pointed out in the previous chapter, in the ergodic phase deviations of the SFF from RMT are larger with open boundaries, consistent with the picture of domains in the orbit pairing. By contrast, in the MBL phase $\langle K(t) \rangle$ is largely insensitive to changes at the boundary. This difference in sensitivities of spectra arises also for single-particle systems [77], although the mechanism is not the same.

4
Summary and outlook

Classical statistical mechanics is rooted in ergodicity, and therefore in chaos. Efforts to unify these ideas with quantum mechanics led first to a connection between classical chaos and RMT spectral statistics [49, 50, 53], and later to the formulation of the ETH [7, 8]. In this way, the emergence of statistical mechanics from unitary quantum dynamics is associated with universal spectral correlations. The failure of statistical mechanics, in the MBL phase, is associated with their loss [24].

A physical feature, conspicuously missing in a random matrix, is locality. Since the modern understanding of thermalisation is based on ideas such as entanglement growth and operator spreading, we are led to ask, for example, which degrees of freedom are entangled. To answer this question it is natural to consider minimal models with local interactions, such as RUCs [12, 13, 20]. To answer questions about spectral statistics, on the other hand, a fixed evolution operator is required. For this reason we have focused on dynamics under RFCs [34–36, 90, 109].

The emergence of RMT spectral statistics in semiclassical and in mesoscopic systems can be understood through the diagonal approximation to sums over paired paths [53, 61]. Moving to the many-body setting the paths of interest are in Fock space (or, in the semiclassical limit, in the many-body phase space [116, 146, 147]). Locality is manifest in correlations between the amplitudes of these paths, and to study these correlations our approach has been to average physical

quantities over an ensemble of random systems. The central quantity we have considered is the SFF, which is a sensitive probe of the spectral statistics. The SFF is expressible as a sum over pairs of closed paths, or many-body orbits, and in RFCs the average of this sum can be generated by powers of an averaged transfer matrix that acts in the space direction [35, 115].

In Chapter 2 we have developed this framework in the setting of many-body Floquet models with local interactions, thereby showing how the diagonal approximation must be modified. We have revealed domains in the pairing of orbits, whose characteristic spatial extent is an increasing function of time t [see also Ref. [109]]. Due to the entropy of these domain walls the Thouless time t_{Th}, beyond which the SFF matches RMT, grows with system size L. Furthermore, our results show that there are deviations of the SFF from RMT which grow exponentially on increasing L at fixed t. The existence of pairing domains also implies divergent departures from the ETH.

In the ergodic phase and for large L there is nevertheless a wide window of time $t_{\mathrm{Th}} \ll t \ll t_{\mathrm{H}}$ where the dominant contributions to the SFF correspond to a single domain in the orbit pairing, so where the diagonal approximation is appropriate. Decreasing the strength of the coupling between the different degrees of freedom, in Chapter 3 we have shown how many-body localisation can be understood as the breakdown of the diagonal approximation over all time and length scales. Furthermore, we have shown how the transition from a MBL phase to an ergodic one can be viewed as symmetry breaking. We have also introduced a local order parameter for the transition. In the ergodic phase its correlation length reflects the spatial extent of pairing domains, and grows rapidly with increasing t. In the MBL phase correlations are short-ranged relative to the system size L for all $t < t_{\mathrm{H}}$.

The work in this thesis suggests a number of promising directions. To appreciate the generality of our picture of locally-paired paths, it is useful to first contrast it with that arising in studies of entanglement growth and scrambling. We then indicate features expected to arise in the presence of time-reversal symmetry, and also how our

approach can be extended to higher moments of physical quantities. We close with a discussion of broader classes of models, including those with Hamiltonian dynamics.

Entanglement entropies are nonlinear in the density matrix. In studies of entanglement growth, it is therefore natural to consider sums over multiple pairs of Fock-space paths. Averaging over ensembles of random systems, nontrivial structures arise from the freedom to pair up different copies of paths in the average [148]. The entanglement membrane, for example, is a domain wall in the pairing of copies [20, 106–108]. Working with RUCs, from a d-dimensional quantum model one arrives at a classical description in $(d+1)$ dimensions. The space-time-local degrees of freedom in the classical description take values in the permutation group.

In our case there are two important departures from the above. First, in studying the SFF of a fixed unitary operator, the contributing Fock-space paths have amplitudes that are invariant under translation in time. Second, because the SFF is a sum over only pairs of paths, involving only one 'copy' of the evolution operator and its conjugate, there is no permutation symmetry. Nontrivial structures instead arise from the freedom to pair up paths modulo a time-translation. Then, from a d-dimensional quantum model, averaging the SFF yields an approximate classical description in just d dimensions.

Unlike in many studies of the entanglement membrane [see Ref. [107] in particular], the connection to classical statistical mechanics is here limited due to the appearance of negative weights. However, these weights are related to powers of eigenvalues of the average transfer matrix, and we have seen that the leading eigenvalues are real and positive. These dominate the behaviour over large lengthscales. The space-local degrees of freedom of our emergent classical model take values in the symmetry group of individual paths, which for the SFF is that of discrete time translations. At (integer) time t this is the symmetry group of a t-state clock model.

Such a connection, between d-dimensional quantum systems and d-dimensional classical models describing the pairing degrees of freedom, is not limited to the SFF. We have additionally shown how it can be used to understand structure beyond

the ETH in the matrix elements of local observables. A natural way to expand the symmetry group of the Fock-space paths, thereby enhancing the pairing freedom, is to introduce TRS. Restricting to the SFF, we then anticipate an approximate classical description with $2t$ site-local degrees of freedom at time t [35, 115]. This suggests larger deviations from RMT and the ETH in the ergodic phase.

A detailed extension of our approach to systems with TRS would be worthwhile. Note that, in that case, one also has contributions from the class of interference effects discussed by Sieber and Richter [149]. Deep in the ergodic phase these effects are likely to appear in a different time regime ($t \sim t_{\mathrm{H}}$) to the pairing domains we have considered ($t < t_{\mathrm{Th}}$). However, near the transition to a MBL phase, these timescales may be comparable. One question is whether Sieber-Richter pairings have clear signatures in the transfer matrix generating the SFF.

Another possible direction is to consider higher moments of the SFF. These are naturally expressed in terms of multiple pairs of Fock-space paths, so one finds a permutation symmetry as in studies of entanglement growth. The transfer matrices generating these higher moments inherit this permutation symmetry, and the approaches we have outlined in Secs. 2.5 and 3.3.1 can be adapted [see also Sec. 2.8]. This would provide a more complete characterisation of spectral statistics, a programme already initiated in certain exactly-solvable models in Refs. [117, 131]. The fluctuations are, however, most extreme in the MBL phase and within its vicinity, where numerical approaches are required.

Moving beyond systems with finite-range interactions, and generalising even to Hamiltonian systems, physical quantities remain expressible as sums over Fock-space paths. Of course, with a Hamiltonian, one has the additional freedom to take the limit where these sums become path integrals. In any case, one can ask questions about the nature of the dominant pairs of paths [see Refs. [113, 116, 146, 150, 151] for related work in semiclassical systems]. Numerical tools, such as symmetry-breaking boundary conditions [Sec. 2.5.2], local order parameters [Sec. 2.5.3] and fields [Sec. 3.4] can in principle be developed even where no transfer-matrix approach

is possible. Moreover, where a local-pairing description is appropriate, this may be indicated in the scaling of certain physical quantities with system size.

However, one feature arising in local Hamiltonians, absent in the Floquet models we have considered, is a locally conserved energy density. Introducing a conservation law leads to prominent deviations of the SFF from RMT even within the diagonal approximation [123, 125, 152]. With a conserved scalar charge, for example, one finds deviations that persist up to a Thouless time that scales diffusively $t_{\mathrm{Th}} \sim L^2$. An immediate question is how conserved charges affect our picture of local pairing. Another feature of Hamiltonian dynamics, crucial for our discussion, is that closed paths in Fock space have amplitudes that are invariant under continuous, as opposed to discrete, time translations. With regards to the MBL transition, this implies that the broken symmetry in the ergodic phase would be continuous one.

Appendices

A.1 Haar-random unitary matrices

In this appendix we discuss various aspects of the Haar distribution on the unitary group. In A.1.1 we define the Haar measure, and then in A.1.2 and A.1.3 discuss spectral statistics. Following this, in A.1.4 we compute the nonzero fourth moment of the distribution. We close with a discussion of numerical sampling in A.1.5.

A.1.1 Basic properties

The invariant Haar measure is defined as follows [44]. For the $N \times N$ unitary matrix W, we consider an infinitesimal change

$$W + dW = (1 + idH)W, \tag{A.1}$$

where dH is Hermitian. It is useful to write dH in terms of real and imaginary parts, $dH = dH^R + idH^I$. A volume element in the unitary group, in the vicinity of W, can then be defined by

$$d\mu(W) = \prod_{j \leq k} dH^R_{jk} \prod_{j<k} dH^I_{jk}. \tag{A.2}$$

The measure $d\mu(W)$ has the invariance property $d\mu(W) = d\mu(UWV)$, where U and V are unitary matrices that are independent of W. To show this, consider $W' = UWV$ and the infinitesimal change $W' + dW' = (1 + idH')W'$. The infinitesimal Hermitian matrices we need are given by $idH = dWW^{-1}$ and $idH' = dW'W'^{-1}$. We also have $dW' = UdWV$ and therefore

$$dH' = UdHU^{-1}. \tag{A.3}$$

To relate $d\mu(W)$ and $d\mu(W')$ we need the Jacobian J of the transform from dH to dH'. This is a $N^2 \times N^2$ matrix with elements

$$J_{ij,kl} = \partial H'_{ij}/\partial H_{kl} = U_{ik}U^{-1}_{lj}, \tag{A.4}$$

so J is the tensor product $U \otimes U^*$, which is unitary. Therefore the determinant $\det(J) = 1$, and $d\mu(W) = d\mu(W')$. Setting $W = V = \mathbb{1}$ we have $d\mu(\mathbb{1}) = d\mu(U)$ for any unitary U.

Note also that $d\mu(W)$ is the unique measure with this invariance property. To see this suppose first that there exists another, $d\mu'(W)$. Then the ratio

$$\varphi(W) = \frac{d\mu'(W)}{d\mu(W)} = \frac{d\mu'(\mathbb{1})}{d\mu(\mathbb{1})}, \tag{A.5}$$

where we have used the invariance properties of our two measures. $\varphi(W)$ is therefore a constant. If we impose the normalisation condition $\int d\mu(W) = 1$ on both measures, we have $d\mu(W) = d\mu'(W)$.

A.1.2 Distribution of eigenvalues

Here we discuss the distribution of eigenvalues $e^{i\theta_n}$, with $n = 0 \ldots (N-1)$, for Haar-random unitary matrices W. We start from the spectral decomposition

$$W = Ve^{i\theta}V^\dagger, \tag{A.6}$$

where θ, with no subscript, is an $N \times N$ diagonal matrix with entries θ_n. The columns of V are the eigenvectors. A small change in W can be expressed as

$$dW = dVe^{i\theta}V^\dagger + iVd\theta e^{i\theta}V^\dagger + Ve^{i\theta}dV^\dagger, \tag{A.7}$$

or alternatively using Eq. (A.1). The changes in the eigenvectors take the form $dV = idMV$ for dM Hermitian. Our aim is to write the Haar measure $d\mu(W)$ in terms of $d\theta$ and dM. From the Jacobian of the transform from dH coordinates to $d\theta$ and dM, we can determine the probability distribution of θ.

The Jacobian of interest, which in an abuse of notation we again denote J, appears in

$$\prod_{i\leq j} dH_{ij}^R \prod_{i<j} dH_{ij}^I = \det(J) \prod_m d\theta_m \prod_{m<n} dM_{mn}^R dM_{mn}^I, \tag{A.8}$$

where $dM = dM^R + i dM^I$. In fact, because $d\mu(W) = d\mu(e^{i\theta})$, we can determine J by considering $V = \mathbb{1}$; importantly $dV \neq 0$. The relation between dH, $d\theta$ and dM can then be written

$$dH = dM e^{i\theta} - e^{i\theta} dM + e^{i\theta} d\theta. \tag{A.9}$$

From this we find

$$\begin{aligned} dH_{mn}^R &= dM_{mn}^R [1 - \cos(\theta_m - \theta_n)] + dM_{mn}^I \sin(\theta_m - \theta_n) + \delta_{mn} d\theta_m \\ dH_{mn}^I &= dM_{mn}^I [1 - \cos(\theta_m - \theta_n)] - dM_{mn}^R \sin(\theta_m - \theta_n). \end{aligned} \tag{A.10}$$

The Jacobian matrix is sparse: dH_{mn} is independent of dM_{pq} unless $m = p$ and $n = q$. This means that

$$\det(J) = \prod_{m<n} |J_{mn}| \prod_p |J_{pp}| \tag{A.11}$$

where $|J_{pp}| = 1$ because $dH_{pp}^R = d\theta_p$. For $m < n$ we have

$$|J_{mn}| = \begin{vmatrix} \partial H_{mn}^R / \partial M_{mn}^R & \partial H_{mn}^I / \partial M_{mn}^R \\ \partial H_{mn}^R / \partial M_{mn}^I & \partial H_{mn}^I / \partial M_{mn}^I \end{vmatrix} = |e^{i\theta_m} - e^{i\theta_n}|^2. \tag{A.12}$$

From this we find

$$d\mu(W) = \prod_{m<n} |e^{i\theta_n} - e^{i\theta_m}|^2 \prod_m d\theta_m \prod_{m<n} dM_{mn}^R dM_{mn}^I. \tag{A.13}$$

Integrating over the variations in the eigenvectors dM we find the joint probability distribution of eigenvalues in the CUE

$$p(\theta_0 \ldots \theta_{N-1}) = \frac{1}{A} \prod_{m<n} |e^{i\theta_n} - e^{i\theta_m}|^2, \tag{A.14}$$

where A is a normalisation constant.

A.1.3 Spectral form factor

The distribution Eq. (A.14) is the modulus square of a Slater determinant, corresponding to the wavefunction for a N-particle Fermi sea. To see this, consider N fermions $n = 0 \dots (N-1)$ on the unit circle $0 \leq \theta < 2\pi$ with momenta $k = 0 \dots (N-1)$. The single particle wavefunctions

$$\langle \theta | k \rangle = \frac{1}{\sqrt{2\pi}} e^{ik\theta}, \tag{A.15}$$

so that the many-body wavefunction for the Fermi sea is $\langle \theta_1 \dots \theta_N | \Psi \rangle = \det(F)$, where the $N \times N$ matrix F has components $F_{nk} = \langle \theta_n | k \rangle$, and

$$\langle \theta_1 \dots \theta_N | \Psi \rangle = \frac{1}{(2\pi)^{N/2}} \prod_{m<n} \left(e^{i\theta_n} - e^{i\theta_m} \right). \tag{A.16}$$

The probability density $| \langle \theta_1 \dots \theta_N | \Psi \rangle |^2$ is precisely Eq. (A.14). We can also identify the constant $A = (2\pi)^N$.

This interpretation allows for an efficient calculation of the average SFF $\langle K(t) \rangle$ for all integer t and N,

$$\begin{aligned} \langle K(t) \rangle &= \sum_{mn} \left\langle e^{i(\theta_m - \theta_n)t} \right\rangle \\ &= N + \sum_{m \neq n} \int d\theta_1 \dots d\theta_N e^{i(\theta_m - \theta_n)^t} p(\theta_1 \dots \theta_N) \\ &= N + \sum_{m \neq n} \langle \Psi | e^{i(\theta_m - \theta_n)t} | \Psi \rangle \,. \end{aligned} \tag{A.17}$$

Now $e^{i\theta_m t}$ can be interpreted as a boost operator, increasing the momentum of particle m by t, because $\langle k+q | e^{i\theta_m t} | k \rangle = \delta_{qt}$. In this way we see that $e^{i(\theta_m - \theta_n)t}$ is the exchange operator for fermions with momenta differing by t. The state $|\Psi\rangle$ involves fermions with momenta $k = 0 \dots (N-1)$, so for $t < N$ we find

$$\sum_{m \neq n} \langle \Psi | e^{i(\theta_m - \theta_n)t} | \Psi \rangle = -(N-t), \tag{A.18}$$

this is because there are $(N-t)$ pairs of occupied k-states with momenta differing by t. The minus sign comes from the exchange statistics of the fermions. From this we find the ramp $\langle K(t) \rangle = t$.

On the other hand, for $t \geq N$ the quantity $\langle \Psi | e^{i(\theta_m - \theta_n)t} | \Psi \rangle = 0$. This gives the plateau $\langle K(t) \rangle = N$. Within this framework the abrupt crossover from ramp to plateau in the SFF is due to the sharp edge of the Fermi sea in momentum space.

A.1.4 Fourth moment

Here we show how to calculate the nonzero fourth moment of the Haar distribution, used in Eq. (2.75). The approach here follows Ref. [12]. Consider

$$O(U) = U\left|a\right\rangle \left\langle b\right| U^\dagger \otimes U\left|c\right\rangle \left\langle d\right| U^\dagger, \tag{A.19}$$

for U a $N \times N$ Haar-random unitary matrix, and the Haar average $\langle O\rangle \equiv \langle O(U)\rangle$. Using the invariance property of the Haar distribution,

$$\langle O(U)\rangle \equiv \int d\mu(U) O(U) = \int d\mu(U) O(VU), \tag{A.20}$$

so that $\langle O(U)\rangle = \langle O(VU)\rangle$ for any unitary V, and similar for right-multiplication. This means that $\langle O\rangle$ commutes with $V\otimes V$ for all V. Using this and the permutation symmetry of $V \otimes V$, we can determine $\langle O\rangle$.

Defining the swap operator Σ, acting as $\Sigma\left|a\right\rangle \otimes \left|b\right\rangle = \left|b\right\rangle \otimes \left|a\right\rangle$, it is clear that $[V \otimes V, \Sigma] = 0$. The swap has two distinct eigenvalues ± 1 corresponding to symmetric and antisymmetric sectors, with respective dimensions $\frac{1}{2}N(N \pm 1)$. We can therefore write

$$V \otimes V = V_+ \oplus V_-, \tag{A.21}$$

where V_+ acts within the symmetric sector, and V_- within the antisymmetric sector. Now because $\langle O\rangle$ commutes with $V_+ \oplus V_-$ for all V, its action must be proportional to the identity within each of the symmetric and antisymmetric sectors,

$$\langle O\rangle = \langle O_+\rangle \oplus \langle O_-\rangle. \tag{A.22}$$

Here $\langle O_\pm\rangle = C_\pm \mathbb{1}_\pm$, where $\mathbb{1}_\pm$ are identity operators acting in each of the two sectors, and $C_\pm$ are scalars. It is convenient to introduce projectors $P_\pm = \frac{1}{2}(1 \pm \Sigma)$ so that, if we extend the action of $\langle O_\pm\rangle$ to the full space, we can write $\langle O_\pm\rangle = P_\pm \langle O\rangle P_\pm$. Then $C_\pm \mathrm{Tr}[\mathbb{1}_\pm] = \mathrm{Tr}[\langle O_\pm\rangle]$ gives

$$C_\pm = \frac{\mathrm{Tr}[P_\pm \langle O\rangle P_\pm]}{\frac{1}{2}N(N \pm 1)} = \frac{\delta_{ab}\delta_{cd} \pm \delta_{cb}\delta_{ad}}{N(N \pm 1)}, \tag{A.23}$$

where we have used the cyclic property of the trace.

The resulting expression for $\langle O \rangle$ implies

$$\langle U_{a'a} U^*_{b'b} U_{c'c} U^*_{d'd} \rangle = \sum_{s=\pm 1} \frac{1}{2N(N+s)} \Big(\delta_{ab}\delta_{cd} + s\delta_{cb}\delta_{ad} \Big) \Big(\delta_{a'b'}\delta_{c'd'} + s\delta_{a'd'}\delta_{b'c'} \Big), \tag{A.24}$$

from Eq. (A.19). Eq. (A.24) is a sum over all possible contractions of the first and second indices. When the first and second indices are contracted in the same way we have the Weingarten function $\mathrm{Wg}(\mathbb{1})$, and otherwise we have $\mathrm{Wg}(12)$, with

$$\mathrm{Wg}(\mathbb{1}) = \frac{1}{N^2 - 1}, \quad \mathrm{Wg}(12) = -\frac{1}{N(N^2-1)}. \tag{A.25}$$

A.1.5 Numerical sampling

Generating Haar-random unitary matrices is non-trivial because their entries are not statistically independent: a $N \times N$ complex unitary matrix has only N^2 real degrees of freedom. Following Mezzadri [153], we start by sampling a distribution of complex matrices M that are not constrained to be unitary, and use this to induce Haar measure on a distribution of unitary matrices.

We draw M from the Ginibre ensemble of $N \times N$ complex matrices. Different elements $M_{jk} = M^R_{jk} + iM^I_{jk}$, and indeed their real M^R_{jk} and imaginary M^I_{jk} parts, are drawn independently from unit-normal distributions. In this way the probability density $p_G(M)$ on the space of complex matrices is

$$p_G(M) = \frac{1}{\pi^{N^2}} e^{-\mathrm{Tr}[MM^\dagger]}, \tag{A.26}$$

which is normalised. When integrating over the space of $N \times N$ complex matrices, the weight assigned to the volume element in the vicinity of M is

$$d\mu_G(M) = p_G(M) \prod_{jk} dM^R_{jk} dM^I_{jk}, \tag{A.27}$$

which defines the measure for the Ginibre ensemble. From Eq. (A.26), $p_G(UMV) = p_G(M)$ for U and V two $N \times N$ unitary matrices. To show that the measure $d\mu_G(M)$ is invariant we must consider the Jacobian J for the transformation $dM \to UdMV$. This is a $N^2 \times N^2$ complex matrix with entries

$$J_{ij,kl} = \partial [UMV]_{ij} / \partial M_{kl} = U_{ik} V_{lj}, \tag{A.28}$$

or $J = U \otimes V^T$, so $\det(J) = 1$. From this we have $d\mu_G(UMV) = d\mu_G(M)$. This invariance property is shared with the Haar measure on unitary matrices.

A useful map from complex matrices to unitary ones is provided by the QR decomposition: any $N \times N$ complex matrix M can be written as $M = QR$ with Q unitary and R upper triangular. We write this as $M \to (Q, R)$. Unfortunately, this decomposition is not unique. To see this suppose that $M \to (Q, R)$ and $M \to (Q', R')$. Rearranging $QR = Q'R'$ we find

$$Q'^{-1}Q = R'R^{-1} \equiv D. \tag{A.29}$$

Because Q and Q' are unitary, so is D. Similarly, the inverse of an upper triangular matrix is upper triangular, as is the product of two upper triangular matrices. Therefore D is both upper triangular and unitary. This implies that its inverse $D^\dagger$ is also upper triangular. For D and $D^\dagger$ to both be upper triangular, they must in fact be diagonal, so we are free to choose $Q = Q'D$ and $R = D^*R'$ for any diagonal unitary matrix D.

To remove this freedom we define a modified QR decomposition $M \rightsquigarrow (Q, R)$ where Q and R are uniquely determined by M, and where $UMV \rightsquigarrow (UQV, R)$. Drawing M from the Ginibre ensemble we induce measures on the spaces of unitary matrices Q, and of upper triangular matrices R, via $d\mu_G(M) = d\mu_Q(Q)d\mu_R(R)$. Then, because $d\mu_G(M) = d\mu_G(UMV)$, we have $d\mu_Q(Q) = d\mu_Q(UQV)$. As we have shown in Eq. (A.5), the Haar measure on the unitary group is the unique measure with this invariance property. Therefore, $d\mu_Q(Q)$ is Haar measure.

In practice, the freedom associated with D can be removed by restricting R generated by $M \rightsquigarrow (Q, R)$ to have real positive entries. To do this we use a standard QR decomposition $M \to (Q', R')$ and define a diagonal unitary matrix D via $D_{jj} = R'_{jj}/|R'_{jj}|$. Setting $R = D^*R'$ and $Q = Q'D$, we have Haar-random Q for M distributed according to Eq. (A.26).

A.2 Numerical methods

Here we outline the numerical methods used throughout Chapters 2 and 3. For all numerics we use a local Hilbert space dimension $q = 2$, except where stated explicitly, and for all averages over the Haar distribution we use Monte Carlo. We sample this distribution using the approach set out in A.1.5.

In Fig. 2.3(b) we have averaged the SFF over 10^4 realisations of one gate, and in (c) over 10^6 realisations of the Floquet operator. Calculations of the average SFF $\langle K(t)\rangle$ in Fig. 2.4 are based on ED of the Floquet operator, using 10^6 realisations for $L \leq 8$ and 10^5 for $L \geq 9$. These calculations were used for the analysis in Figs. 2.9. Calculations of $\langle Z(s,t)\rangle$ [Eq. (2.37)] leading to Figs. 2.12, 2.13, 2.14 and 2.15 used $L \leq 8$ and 10^6 realisations, with a simultaneous Monte Carlo over Floquet operators and boundary conditions [see Fig. 2.11].

In Figs. 2.24 and 2.25 we have carried out calculations in the quasienergy domain using ED in system sizes $8 \leq L \leq 12$, and using a Lanczos method for $L = 14$. Standard Lanczos algorithms require Hermitian operators, and so instead of working with W we first determine a set of eigenvectors $|n\rangle$ of $\frac{1}{2}(W + W^\dagger)$, with eigenvalues $\cos\theta_n$. There are no symmetries or degeneracies, so this approach unambiguously determines the eigenstates of W. The sign of θ_n is then determined by acting on the eigenvectors with $\frac{1}{2i}(W - W^\dagger)$. In all system sizes we sample eigenstates of W whose quasienergies reside in bins of fixed width $20(2\pi)/(2^{14})$ centred on $\theta = 2\pi k/50$ for $k = 0 \ldots 49$. For each eigenvector $|n\rangle$ we only store its eigenphase θ_n and the diagonal matrix elements of a complete set of local Hermitian operators $\tau_{x,j}$ (with $x = 0 \ldots (L-1)$ and $j = 0 \ldots (q^2-1)$), $\langle n|\tau_{x,j}|n\rangle$. Square bins for the sampling of quasienergies implies triangular bins for the sampling of quasienergy differences $\omega = |\theta_n - \theta_m|$. Having fixed the bin widths, the number of circuit realisations we use varies with L in such a way that we have over 10^7 contributions to each $\mathrm{Tr}[\rho_x(n)\rho_x(m)]$ data point in Fig. 2.25. This number is based on using 10^3 realisations of the Floquet operator for $L = 14$.

In Chapter 2, calculations of the r-statistic and $\langle K(t)\rangle$ in Figs. 3.1(a) and (b), respectively, are again based on ED of Floquet operators. There we use 10^4

disorder realisations for each L and J. Calculations of the half-chain von Neumann entanglement entropy $S_{L/2}$ in Fig. 3.2(a) use ED with $10^4, 10^4, 10^3$ and 10^2 disorder realisations for $L = 6, 8, 10$ and 12, respectively. To study the growth of $S_{L/2}$ with time in Figs. 3.2(b) and (c) we did not need to store the Floquet operator. In this way we were able to access relatively large system sizes. For each realisation of random local fields we initialised the system in an eigenstate of the decoupled system ($J = 0$), and followed the time evolution for $J \neq 0$ by acting on this state one 4×4 unitary matrix at a time.

The calculations in Fig. 3.4 are based on length-scaling of $\langle K(t) \rangle$, itself determined via ED. Averages were over 10^6 disorder realisations for system sizes $3 \leq L \leq 8$, 2×10^5 for $L = 9, 10$, and 2×10^4 for $L = 11, 12$. The two-point functions in Figs. 3.6 and 3.7 were also calculated via ED. There for $L \leq 9$ we average over 10^5 disorder realisations, and for $L \geq 10$ over 10^4. Data in Fig. 3.8 comes from calculations performed in the same way as shown in Fig. 3.7, for additional values of J [not shown]. Results in Figs. 3.9 and 3.10 are based on ED with averages over $10^5, 10^3$ and 5×10^2 disorder realisations for $L = 8, 10$ and 12, respectively. In Fig. 3.10 we use square bins for quasienergy separations. Finally, in Fig. 3.11, for $L = 8, 10$ we average over $N = 10^5$ disorder realisations, and for $L = 12$ over $N = 10^4$.

A.3 L-scaling

In this appendix we describe the methods used to determine the leading eigenvalues of the transfer matrix, as well as the overlaps of the associated eigenvectors with the boundary states $\langle \mathcal{B}_L|$, $|\mathcal{B}_R\rangle$ and the local diagonal states $|\nu\rangle$.

In Fig. 2.9 we have shown that with open boundary conditions and large L the behaviour of the leading eigenvalue of $\langle \mathcal{T}(t) \rangle$ in the $\nu = 0$ sector, $\lambda(0, t)$, controls the behaviour of the average SFF. Taking the logarithm of Eq. (2.32) we have

$$\ln\langle K(t) \rangle \simeq (L-1) \ln \lambda(0,t) + \ln \langle \mathcal{B}_L|\nu, t; R\rangle \langle \nu, t; L|\mathcal{B}_R\rangle \,, \tag{A.30}$$

where we have neglected contributions from subleading eigenvalues. In practice, for a given t we fit only to data with sufficiently large L that $t < \frac{1}{2} t_{\rm H} \equiv \frac{1}{2} q^L$. By

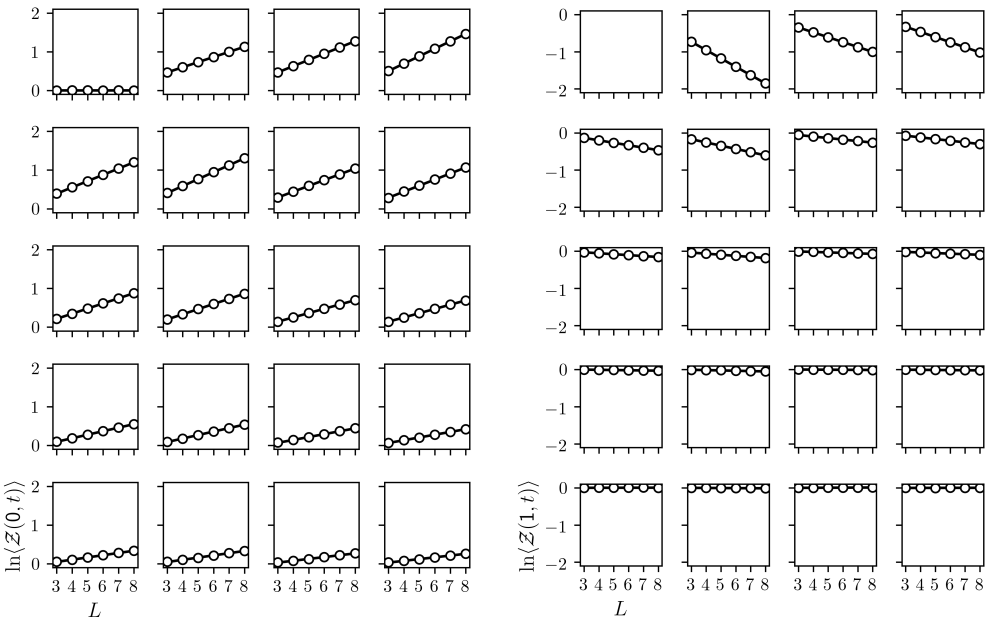

Figure A.1: $\ln\langle\mathcal{Z}(\nu,t)\rangle$ in sector $\nu=0$ (left array) and $\nu=1$ (right array). Individual panels correspond to times $t=1\ldots20$ in reading order for each ν. L-scaling gives the leading eigenvalue $\lambda(\nu,t)$ of $\langle\mathcal{T}(t)\rangle$, as well as the overlaps $\langle\nu|\nu,t;R\rangle\,\langle\nu,t;L|\nu\rangle$ between the corresponding eigenvectors and the diagonally-paired states $|\nu\rangle$.

restricting to L such that t is well below the Heisenberg time, we avoid contributions to $\langle K(t)\rangle$ from subleading eigenvalues of $\langle\mathcal{T}(t)\rangle$.

To determine the leading eigenvalues in the $\nu\neq0$ sectors we follow the behaviour of $\langle\mathcal{Z}(\nu,t)\rangle$ [Eq. (2.39)] as L is varied. For sufficiently large L, Eq. (2.40) gives

$$\ln\langle\mathcal{Z}(\nu,t)\rangle\simeq(L-1)\ln\lambda(\nu,t)+\ln\langle\nu|\nu,t;R\rangle\,\langle\nu,t;L|\nu\rangle\,. \tag{A.31}$$

In Fig. A.1 we show $\ln\langle\mathcal{Z}(\nu,t)\rangle$ versus L in Haar-RFCs for sectors $\nu=0$ and $\nu=1$, and for times $1\leq t\leq20$. The linear relationship suggested by Eq. (A.31) holds very well even for systems of only $L=3$ sites (and so only two gates). From the fits we can read off $\lambda(0,t)$ and $\langle\nu|\nu,t;R\rangle\,\langle\nu,t;L|\nu\rangle$. The results are shown in Fig. 2.14. Fits for other values of ν are of similar quality.

As discussed through Secs. 2.5.2 and 2.5.3, the local diagonal pairings $|\nu\rangle$ are closely related to the leading eigenvectors of $\langle\mathcal{T}(t)\rangle$. Consequently we expect that the contributions of subleading eigenvalues to Eq. (A.31) are suppressed. Moreover, while there is an abrupt change in the behaviour of $\langle K(t)\rangle$ at $t=t_{\mathrm{H}}$, this is not

the case for $\langle \mathcal{Z}(\nu, t)\rangle$. For these reasons, in contrast with Fig. 2.9(b), we include all available data ($3 \leq L \leq 8$) in the fits in Fig. A.1. The quality of these fits is evidence that the subleading eigenvalues are playing only a minor role.

A.4 Large-q transfer matrix

Here we discuss the large-q limit of the average transfer matrix $\langle \mathcal{T}(t)\rangle$ for Haar-RFCs. In Eq. (2.25) we have given an expression for $\langle \mathcal{T}(t)\rangle$ in terms of Weingarten functions $\mathrm{Wg}(\sigma\tau^{-1})$ and unnormalised permutation states $|\sigma, \tau\rangle$.

The Weingarten functions are maximised for $\sigma = \tau$, taking the value $\mathrm{Wg}(\mathbb{1}) = q^{-2t}$ in the large-q limit [45, 46]. Furthermore, the states $|\sigma, \tau\rangle$ that maximise $\langle \sigma, \tau|\mathcal{S}|\sigma, \tau\rangle$ are those with $\sigma = \tau$ cyclic permutations, mapping $r \to r + s$ modulo t. Normalising these states we find $|s\rangle$ defined in Eq. (2.24). This motivates the large-q approximation to the average transfer matrix

$$\langle \mathcal{T}(t)\rangle = \sum_{s=0}^{t-1} |s\rangle \langle s| . \tag{A.32}$$

The different states $|s\rangle$ correspond to the different local diagonal orbit pairings. Note, however, that the states $|s\rangle$ are not orthogonal. Approximating $\langle \mathcal{T}(t)\rangle$ by Eq. (A.32) at general values of q, it is straightforward to calculate the SFF. This approach reveals a number of interesting features.

Note that Eq. (A.32) is the transfer matrix for a clock model: $\langle s|s'\rangle$ depends only on $|s - s'|$. We first diagonalise $\langle \mathcal{T}(t)\rangle$ by writing it in terms of the orthogonal (but not normalised) states $|\nu\rangle = (1/\sqrt{t}) \sum_{s=0}^{t-1} e^{-2\pi i\nu s} |s\rangle$. The result is

$$\langle \mathcal{T}(t)\rangle = \sum_{\nu=0}^{t-1} |\nu\rangle \langle \nu| . \tag{A.33}$$

Within this approximation the norms of the states $|\nu\rangle$ are the eigenvalues of $\langle \mathcal{T}(t)\rangle$

$$\langle \nu|\nu\rangle = \frac{1}{t} \sum_{s,s'} e^{2\pi i\nu(s-s')/t} \langle s|s'\rangle . \tag{A.34}$$

We will see below that the inner products $\langle s|s'\rangle$ for $s \neq s'$ decay at least as quickly as q^{-t}, so $\langle \nu|\nu\rangle$ approaches unity at late times. Also, since $\langle s|s'\rangle > 0$, the largest eigenvalue of $\langle \mathcal{T}(t)\rangle$ is in the $\nu = 0$ sector just as at small q [see for example Fig. 2.14].

From the eigenvalues $\langle\nu|\nu\rangle$ we can calculate the average SFF with periodic boundary conditions

$$\langle K(t)\rangle = \sum_{\nu=0}^{t-1} \langle\nu|\nu\rangle^L . \tag{A.35}$$

With open boundary conditions on the other hand,

$$\langle K(t)\rangle = t\,\langle\nu=0|\nu=0\rangle^L . \tag{A.36}$$

The eigenvalues $\langle\nu|\nu\rangle$ approach unity at large t so we recover the RMT result $\langle K(t)\rangle = t$.

The eigenvalues $\langle\nu|\nu\rangle$ are given by the inner products $\langle s|s'\rangle$ through Eq. (A.34), and these are

$$\langle s|s'\rangle = \frac{1}{q^{2t}} \sum_{\substack{a_r b_r \\ a_r^* b_r^*}} \prod_{r=0}^{t-1} \delta_{a_r a^*_{r+s}} \delta_{b_r b^*_{r+s}} \delta_{a_r a^*_{r+s'}} \delta_{b_r b^*_{r+s'}} . \tag{A.37}$$

Evaluating the sums on the right-hand side we see that $\langle s|s'\rangle$ is determined by the number of cycles in the permutation mapping $r \to r + |s - s'| \bmod t$. Denoting this cycle number $N_{t,|s-s'|}$,

$$\langle 0|s\rangle = q^{2(N_{t,s}-t)}. \tag{A.38}$$

There is clear s dependence in this expression, and therefore in the domain wall tension and $\langle Z(s,t)\rangle$ [Eq. (2.37)], as observed for $q = 2$ in Fig. 2.13(a). This is to be contrasted with the s-independent domain wall tension found in the large-q limit in the RPM [see Eq. (2.13)].

Note that there is a distinct difference between the SFF at odd and even times. For an even value of t, the largest inner product $\langle 0|s\rangle$ for $s \neq 0$ is $\langle 0|t/2\rangle = q^{-t}$. On the other hand, for t an odd multiple of 3, the largest are $\langle 0|t/3\rangle = \langle 0|2t/3\rangle = q^{-4t/3}$. The deviations of $\langle\nu|\nu\rangle$ from unity can therefore be significantly larger for t even than for t odd. From Eqs. (A.35) and (A.36) we see that this implies larger deviations of the SFF from RMT at even times. We have observed the same behaviour at small q in Fig. 2.4.

Bibliography

[1] S. J. Garratt and J. T. Chalker, "Local pairing of Feynman histories in many-body Floquet models," Physical Review X, vol. 11, p. 021 051, 2021.

[2] S. J. Garratt and J. T. Chalker, "Many-body delocalization as symmetry breaking," Physical Review Letters, vol. 127, p. 026 802, 2021.

[3] H. Murakami, Hard-boiled Wonderland and the End of the World. Kodansha International, 1985.

[4] J. J. Sakurai and S. F. Tuan, Modern Quantum Mechanics. Addison-Wesley, 1994.

[5] L. D. Landau and E. M. Lifshitz, Statistical Physics. Pergamon Press, 1980.

[6] M. C. Gutzwiller, Chaos in Classical and Quantum Mechanics. Springer, New York, 1990.

[7] J. M. Deutsch, "Quantum statistical mechanics in a closed system," Physical Review A, vol. 43, p. 2046, 1991.

[8] M. Srednicki, "Chaos and quantum thermalization," Physical Review E, vol. 50, p. 888, 1994.

[9] A. Polkovnikov, K. Sengupta, A. Silva, and M. Vengalattore, "Colloquium: Nonequilibrium dynamics of closed interacting quantum systems," Reviews of Modern Physics, vol. 83, p. 863, 2011.

[10] L. D'Alessio, Y. Kafri, A. Polkovnikov, and M. Rigol, "From quantum chaos and eigenstate thermalization to statistical mechanics and thermodynamics," Advances in Physics, vol. 65, p. 239, 2016.

[11] J. M. Deutsch, "Eigenstate thermalization hypothesis," Reports on Progress in Physics, vol. 81, p. 082 001, 2018.

[12] A. Nahum, S. Vijay, and J. Haah, "Operator spreading in random unitary circuits," Physical Review X, vol. 8, p. 021 014, 2018.

[13] C. W. von Keyserlingk, T. Rakovszky, F. Pollmann, and S. L. Sondhi, "Operator hydrodynamics, OTOCs, and entanglement growth in systems without conservation laws," Physical Review X, vol. 8, p. 021 013, 2018.

[14] Y. Sekino and L. Susskind, "Fast scramblers," Journal of High Energy Physics, vol. 2008, p. 065, 2008.

[15] S. H. Shenker and D. Stanford, "Black holes and the butterfly effect," Journal of High Energy Physics, vol. 2014, p. 67, 2014.

[16] J. Maldacena, S. H. Shenker, and D. Stanford, "A bound on chaos," Journal of High Energy Physics, vol. 2016, p. 1, 2016.

[17] D. N. Page, "Average entropy of a subsystem," Physical Review Letters, vol. 71, p. 1291, 1993.

[18] H. Kim and D. A. Huse, "Ballistic spreading of entanglement in a diffusive nonintegrable system," Physical Review Letters, vol. 111, p. 127 205, 2013.

[19] W. W. Ho and D. A. Abanin, "Entanglement dynamics in quantum many-body systems," Physical Review B, vol. 95, p. 094 302, 2017.

[20] A. Nahum, J. Ruhman, S. Vijay, and J. Haah, "Quantum entanglement growth under random unitary dynamics," Physical Review X, vol. 7, p. 031 016, 2017.

[21] T. Kinoshita, T. Wenger, and D. S. Weiss, "A quantum Newton's cradle," Nature (London), vol. 440, p. 900, 2006.

[22] I. V. Gornyi, A. D. Mirlin, and D. G. Polyakov, "Interacting electrons in disordered wires: Anderson localization and low-T transport," Physical Review Letters, vol. 95, p. 206 603, 2005.

[23] D. Basko, I. Aleiner, and B. Altshuler, "Metal–insulator transition in a weakly interacting many-electron system with localized single-particle states," Annals of Physics, vol. 321, p. 1126, 2006.

[24] V. Oganesyan and D. A. Huse, "Localization of interacting fermions at high temperature," Physical Review B, vol. 75, p. 155 111, 2007.

[25] M. Znidaric, T. Prosen, and P. Prelovsek, "Many-body localization in the Heisenberg XXZ magnet in a random field," Physical Review B, vol. 77, p. 064 426, 2008.

[26] A. Pal and D. A. Huse, "Many-body localization phase transition," Physical Review B, vol. 82, p. 174 411, 2010.

[27] R. Nandkishore and D. A. Huse, "Many-body localization and thermalization in quantum statistical mechanics," Annual Review of Condensed Matter Physics, vol. 6, p. 15, 2015.

[28] D. A. Abanin, E. Altman, I. Bloch, and M. Serbyn, "Colloquium: Many-body localization, thermalization, and entanglement," Reviews of Modern Physics, vol. 91, p. 021 001, 2019.

[29] M. Serbyn, Z. Papic, and D. A. Abanin, "Local conservation laws and the structure of the many-body localized states," Physical Review Letters, vol. 111, p. 127 201, 2013.

[30] D. A. Huse, R. Nandkishore, and V. Oganesyan, "Phenomenology of fully many-body-localized systems," Physical Review B, vol. 90, p. 174 202, 2014.

[31] A. Chandran, I. H. Kim, G. Vidal, and D. A. Abanin, "Constructing local integrals of motion in the many-body localized phase," Physical Review B, vol. 91, p. 085 425, 2015.

[32] V. Ros, M. Müller, and A. Scardicchio, "Integrals of motion in the many-body localized phase," Nuclear Physics B, vol. 891, p. 420, 2015.

[33] B. Bauer and C. Nayak, "Area laws in a many-body localized state and its implications for topological order," Journal of Statistical Mechanics: Theory and Experiment, vol. 2013, p. 09 005, 2013.

[34] A. Chan, A. De Luca, and J. T. Chalker, "Solution of a minimal model for many-body quantum chaos," Physical Review X, vol. 8, p. 041 019, 2018.

[35] B. Bertini, P. Kos, and T. Prosen, "Exact spectral form factor in a minimal model of many-body quantum chaos," Physical Review Letters, vol. 121, p. 264 101, 2018.

[36] H. Gharibyan, M. Hanada, S. H. Shenker, and M. Tezuka, "Onset of random matrix behavior in scrambling systems," Journal of High Energy Physics, vol. 2018, p. 124, 2018.

[37] A. A. Abrikosov, L. P. Gorkov, and I. E. Dzyaloshinkii, Methods of Quantum Field Theory in Statistical Physics. Courier Corporation, 2012.

[38] M. L. Mehta, Random matrices. Academic Press, San Diego, 2004.

[39] E. P. Wigner, "On the statistical distribution of the widths and spacings of nuclear resonance levels," Mathematical Proceedings of the Cambridge Philosophical Society, vol. 47, p. 790, 1951.

[40] R. U. Haq, A. Pandey, and O. Bohigas, "Fluctuation properties of nuclear energy levels: Do theory and experiment agree?" Physical Review Letters, vol. 48, pp. 1086–1089, 1982.

[41] F. Haake, Quantum Signatures of Chaos. Springer, New York, 1991.

[42] L. A. Ponomarenko *et al.*, "Chaotic Dirac billiard in graphene quantum dots," Science, vol. 320, p. 356, 2008.

[43] M. Aßmann, J. Thewes, D. Fröhlich, and M. Bayer, "Quantum chaos and breaking of all anti-unitary symmetries in Rydberg excitons," Nature materials, vol. 15, p. 741, 2016.

[44] F. J. Dyson, "Statistical theory of the energy levels of complex systems. I," Journal of Mathematical Physics, vol. 3, p. 140, 1962.

[45] S. Samuel, "$U(N)$ Integrals, $1/N$, and the De Wit–'t Hooft anomalies," Journal of Mathematical Physics, vol. 21, p. 2695, 1980.

[46] P. W. Brouwer and C. W. J. Beenakker, "Diagrammatic method of integration over the unitary group, with applications to quantum transport in mesoscopic systems," Journal of Mathematical Physics, vol. 37, p. 4904, 1996.

[47] M. V. Berry, "Quantum chaology," Proceedings of the Royal Society of London A, vol. 413, p. 183, 1987.

[48] M. V. Berry and M. Tabor, "Level clustering in the regular spectrum," Proceedings of the Royal Society of London A, vol. 356, p. 375, 1977.

[49] G. Casati, F. Valz-Gris, and I. Guarnieri, "On the connection between quantization of nonintegrable systems and statistical theory of spectra," Lettere al Nuovo Cimento, vol. 28, p. 279, 1980.

[50] O. Bohigas, M. J. Giannoni, and C. Schmit, "Characterization of chaotic quantum spectra and universality of level fluctuation laws," Physical Review Letters, vol. 52, p. 1, 1984.

[51] M. V. Berry and M. Robnik, "Statistics of energy levels without time-reversal symmetry: Aharonov-Bohm chaotic billiards," Journal of Physics A: Mathematical and General, vol. 19, p. 649, 1986.

[52] M. Robnik and M. V. Berry, "False time-reversal violation and energy level statistics: The role of anti-unitary symmetry," Journal of Physics A: Mathematical and General, vol. 19, p. 669, 1986.

[53] M. V. Berry, "Semiclassical theory of spectral rigidity," Proceedings of the Royal Society of London A, vol. 400, p. 229, 1985.

[54] J. H. Hannay and A. M. O. De Almeida, "Periodic orbits and a correlation function for the semiclassical density of states," Journal of Physics A: Mathematical and General, vol. 17, p. 3429, 1984.

[55] B. L. Altshuler and A. G. Aronov, Electron-electron interactions in disordered systems. North-Holland, Amsterdam, 1985.

[56] P. A. Lee and T. V. Ramakrishnan, "Disordered electronic systems," Reviews of Modern Physics, vol. 57, p. 287, 1985.

[57] B. L. Altshuler, P. A. Lee, and W. R. Webb, Mesoscopic phenomena in solids. North-Holland, Amsterdam, 1991.

[58] P. W. Anderson, "Absence of diffusion in certain random lattices," Physical Review, vol. 109, p. 1492, 1958.

[59] B. Kramer and A. MacKinnon, "Localization: Theory and experiment," Reports on Progress in Physics, vol. 56, p. 1469, 1993.

[60] F. Evers and A. D. Mirlin, "Anderson transitions," Reviews of Modern Physics, vol. 80, 2008.

[61] K. B. Efetov, "Statistics of the levels in small metallic particles," Journal of Experimental and Theoretical Physics, vol. 56, p. 467, 1982.

[62] B. L. Altshuler and B. I. Shklovskii, "Repulsion of energy levels and conductivity of small metal samples," Journal of Experimental and Theoretical Physics, vol. 64, p. 127, 1986.

[63] N. Argaman *et al.*, "Correlations in the actions of periodic orbits derived from quantum chaos," Physical Review Letters, vol. 71, p. 4326, 1993.

[64] A. I. Larkin and D. E. Khmel'nitskii, "Anderson localization and anomalous magnetoresistance at low temperatures," Soviet Physics Uspekhi, vol. 25, p. 185, 1982.

[65] D. Khmel'nitskii, "Localization and coherent scattering of electrons," Physica B+C, vol. 126, p. 235, 1984.

[66] B. L. Altshuler, A. G. Aronov, and B. Z. Spivak, "The Aharonov-Bohm effect in disordered conductors," Journal of Experimental and Theoretical Physics Letters, vol. 33, p. 94, 1981.

[67] D. Y. Sharvin and Y. V. Sharvin, "Magnetic flux quantization in a cylindrical film," Journal of Experimental and Theoretical Physics Letters, vol. 34, 1981.

[68] F. J. Wegner, "The mobility edge problem: Continuous symmetry and a conjecture," Zeitschrift für Physik B: Condensed Matter, vol. 35, p. 207, 1979.

[69] L. P. Gor'Kov and G. M. Eliashberg, "Minute metallic particles in an electromagnetic field," Journal of Experimental and Theoretical Physics, vol. 21, 1965.

[70] D. J. Thouless, "Maximum metallic resistance in thin wires," Physical Review Letters, vol. 39, p. 1167, 1977.

[71] F. J. Dyson and M. L. Mehta, "Statistical theory of the energy levels of complex systems. IV," Journal of Mathematical Physics, vol. 4, p. 701, 1963.

[72] N. F. Mott, "Conduction in non-crystalline systems," The Philosophical Magazine: A Journal of Theoretical Experimental and Applied Physics, vol. 17, p. 1259, 1968.

[73] V. Ambegaokar, B. I. Halperin, and J. S. Langer, "Hopping conductivity in disordered systems," Physical Review B, vol. 4, p. 2612, 1971.

[74] M. Morgan and P. A. Walley, "Localized conduction processes in amorphous germanium," The Philosophical Magazine: A Journal of Theoretical Experimental and Applied Physics, vol. 23, p. 661, 1971.

[75] E. Abrahams, P. W. Anderson, D. C. Licciardello, and T. V. Ramakrishnan, "Scaling theory of localization: Absence of quantum diffusion in two dimensions," Physical Review Letters, vol. 42, p. 673, 1979.

[76] D. C. Licciardello and D. J. Thouless, "Constancy of minimum metallic conductivity in two dimensions," Physical Review Letters, vol. 35, p. 1475, 1975.

[77] J. T. Edwards and D. J. Thouless, "Numerical studies of localization in disordered systems," Journal of Physics C: Solid State Physics, vol. 5, p. 807, 1972.

[78] F. J. Wegner, "Electrons in disordered systems. scaling near the mobility edge," Zeitschrift für Physik B: Condensed Matter, vol. 25, p. 327, 1976.

[79] M. V. Berry, "Regular and irregular semiclassical wavefunctions," Journal of Physics A: Mathematical and General, vol. 10, p. 2083, 1977.

[80] M. Rigol, V. Dunjko, and M. Olshanii, "Thermalization and its mechanism for generic isolated quantum systems," Nature, vol. 452, p. 854, 2008.

[81] M. Srednicki, "The approach to thermal equilibrium in quantized chaotic systems," Journal of Physics A: Mathematical and General, vol. 32, p. 1163, 1999.

[82] E. H. Lieb and D. W. Robinson, "The finite group velocity of quantum spin systems," Communications in Mathematical Physics, vol. 28, p. 251, 1972.

[83] A. Nahum, J. Ruhman, and D. A. Huse, "Dynamics of entanglement and transport in one-dimensional systems with quenched randomness," Physical Review B, vol. 98, p. 035 118, 2018.

[84] M. K. Joshi *et al.*, "Quantum information scrambling in a trapped-ion quantum simulator with tunable range interactions," Physical Review Letters, vol. 124, p. 240 505, 2020.

[85] B. Vermersch, A. Elben, L. M. Sieberer, N. Y. Yao, and P. Zoller, "Probing scrambling using statistical correlations between randomized measurements," Physical Review X, vol. 9, p. 021 061, 2019.

[86] R. Islam *et al.*, "Measuring entanglement entropy in a quantum many-body system," Nature, vol. 528, p. 77, 2015.

[87] A. M. Kaufman *et al.*, "Quantum thermalization through entanglement in an isolated many-body system," Science, vol. 353, p. 794, 2016.

[88] T. Brydges *et al.*, "Probing Rényi entanglement entropy via randomized measurements," Science, vol. 364, p. 260, 2019.

[89] C. Pineda and T. Prosen, "Universal and nonuniversal level statistics in a chaotic quantum spin chain," Physical Review E, vol. 76, p. 061 127, 2007.

[90] P. Kos, M. Ljubotina, and T. Prosen, "Many-body quantum chaos: Analytic connection to random matrix theory," Physical Review X, vol. 8, p. 021 062, 2018.

[91] L. Fleishman and P. W. Anderson, "Interactions and the Anderson transition," Physical Review B, vol. 21, p. 2366, 1980.

[92] W. De Roeck, F. Huveneers, M. Müller, and M. Schiulaz, "Absence of many-body mobility edges," Physical Review B, vol. 93, p. 014 203, 2016.

[93] M. Schreiber *et al.*, "Observation of many-body localization of interacting fermions in a quasirandom optical lattice," Science, vol. 349, p. 842, 2015.

[94] J. Smith *et al.*, "Many-body localization in a quantum simulator with programmable random disorder," Nature Physics, vol. 12, p. 907, 2016.

[95] G. De Chiara, S. Montangero, P. Calabrese, and R. Fazio, "Entanglement entropy dynamics of Heisenberg chains," Journal of Statistical Mechanics: Theory and Experiment, vol. 2006, p. 03 001, 2006.

[96] J. H. Bardarson, F. Pollmann, and J. E. Moore, "Unbounded growth of entanglement in models of many-body localization," Physical Review Letters, vol. 109, p. 017 202, 2012.

[97] R. Vosk and E. Altman, "Many-body localization in one dimension as a dynamical renormalization group fixed point," Physical Review Letters, vol. 110, p. 067 204, 2013.

[98] A. Lukin *et al.*, "Probing entanglement in a many-body–localized system," Science, vol. 364, p. 256, 2019.

[99] R. Oliveira, O. C. O. Dahlsten, and M. B. Plenio, "Generic entanglement can be generated efficiently," Physical Review Letters, vol. 98, 2007.

[100] M. Znidaric, "Exact convergence times for generation of random bipartite entanglement," Physical Review A, vol. 78, 2008.

[101] A. Hamma, S. Santra, and P. Zanardi, "Quantum entanglement in random physical states," Physical Review Letters, vol. 109, p. 040 502, 2012.

[102] F. G. S. L. Brandao, A. W. Harrow, and M. Horodecki, "Local random quantum circuits are approximate polynomial-designs," Communications in Mathematical Physics, vol. 346, 2016.

[103] P. Hosur, X.-L. Qi, D. A. Roberts, and B. Yoshida, "Chaos in quantum channels," Journal of High Energy Physics, vol. 2016, 2016.

[104] V. Khemani, A. Vishwanath, and D. A. Huse, "Operator spreading and the emergence of dissipative hydrodynamics under unitary evolution with conservation laws," Physical Review X, vol. 8, p. 031 057, 2018.

[105] T. Rakovszky, F. Pollmann, and C. W. von Keyserlingk, "Diffusive hydrodynamics of out-of-time-ordered correlators with charge conservation," Physical Review X, vol. 8, p. 031 058, 2018.

[106] C. Jonay, D. A. Huse, and A. Nahum, "Coarse-grained dynamics of operator and state entanglement," arXiv:1803.00089, 2018.

[107] T. Zhou and A. Nahum, "Emergent statistical mechanics of entanglement in random unitary circuits," Physical Review B, vol. 99, p. 174 205, 2019.

[108] T. Zhou and A. Nahum, "Entanglement membrane in chaotic many-body systems," Physical Review X, vol. 10, p. 031 066, 2020.

[109] A. Chan, A. De Luca, and J. T. Chalker, "Spectral statistics in spatially extended chaotic quantum many-body systems," Physical Review Letters, vol. 121, p. 060 601, 2018.

[110] T. Prosen, "Time evolution of a quantum many-body system: Transition from integrability to ergodicity in the thermodynamic limit," Physical Review Letters, vol. 80, p. 1808, 1998.

[111] T. Prosen, "Ergodic properties of a generic nonintegrable quantum many-body system in the thermodynamic limit," Physical Review E, vol. 60, p. 3949, 1999.

[112] M. Akila, D. Waltner, B. Gutkin, and T. Guhr, "Particle-time duality in the kicked Ising spin chain," Journal of Physics A: Mathematical and Theoretical, vol. 49, p. 375 101, 2016.

[113] M. Akila, D. Waltner, B. Gutkin, P. Braun, and T. Guhr, "Semiclassical identification of periodic orbits in a quantum many-body system," Physical Review Letters, vol. 118, p. 164 101, 2017.

[114] M. Akila, B. Gutkin, P. Braun, D. Waltner, and T. Guhr, "Semiclassical prediction of large spectral fluctuations in interacting kicked spin chains," Annals of Physics, vol. 389, p. 250, 2018.

[115] P. Braun, D. Waltner, M. Akila, B. Gutkin, and T. Guhr, "Transition from quantum chaos to localization in spin chains," Physical Review E, vol. 101, p. 052 201, 2020.

[116] B. Gutkin and V. Osipov, "Classical foundations of many-particle quantum chaos," Nonlinearity, vol. 29, p. 325, 2016.

[117] A. Flack, B. Bertini, and T. Prosen, "Statistics of the spectral form factor in the self-dual kicked Ising model," Physical Review Research, vol. 2, p. 043 403, 2020.

[118] A. Lerose, M. Sonner, and D. A. Abanin, "Influence matrix approach to many-body Floquet dynamics," Physical Review X, vol. 11, p. 021 040, 2021.

[119] M. Sonner, A. Lerose, and D. A. Abanin, "Characterizing many-body localization via exact disorder-averaged quantum noise," arXiv:2012.00777, 2020.

[120] M. Sonner, A. Lerose, and D. A. Abanin, "Influence functional of many-body systems: Temporal entanglement and matrix-product state representation," Annals of Physics, vol. 431, p. 168 552, 2021.

[121] A. Lerose, M. Sonner, and D. A. Abanin, "Scaling of temporal entanglement in proximity to integrability," Physical Review B, vol. 104, p. 035 137, 2021.

[122] C. L. Bertrand and A. M. García-García, "Anomalous Thouless energy and critical statistics on the metallic side of the many-body localization transition," Physical Review B, vol. 94, p. 144 201, 2016.

[123] A. J. Friedman, A. Chan, A. De Luca, and J. T. Chalker, "Spectral statistics and many-body quantum chaos with conserved charge," Physical Review Letters, vol. 123, p. 210 603, 2019.

[124] P. Sierant, D. Delande, and J. Zakrzewski, "Thouless time analysis of Anderson and many-body localization transitions," Physical Review Letters, vol. 124, p. 186 601, 2020.

[125] S. Moudgalya, A. Prem, D. A. Huse, and A. Chan, "Spectral statistics in constrained many-body quantum chaotic systems," Physical Review Research, vol. 3, p. 023 176, 2021.

[126] M. Serbyn, Z. Papic, and D. A. Abanin, "Thouless energy and multifractality across the many-body localization transition," Physical Review B, vol. 96, p. 104 201, 2017.

[127] C. Monthus, "Many-body-localization transition: Sensitivity to twisted boundary conditions," Journal of Physics A: Mathematical and Theoretical, vol. 50, p. 095 002, 2017.

[128] M. Schiulaz, E. J. Torres-Herrera, and L. F. Santos, "Thouless and relaxation time scales in many-body quantum systems," Physical Review B, vol. 99, p. 174 313, 2019.

[129] R. E. Prange, "The spectral form factor is not self-averaging," Physical Review Letters, vol. 78, p. 2280, 1997.

[130] H. Kunz, "The probability distribution of the spectral form factor in random matrix theory," Journal of Physics A: Mathematical and General, vol. 32, p. 2171, 1999.

[131] A. Chan, A. De Luca, and J. T. Chalker, "Spectral Lyapunov exponents in chaotic and localized many-body quantum systems," Physical Review Research, vol. 3, p. 023 118, 2021.

[132] B. Bertini, P. Kos, and T. Prosen, "Exact correlation functions for dual-unitary lattice models in $1+1$ dimensions," Physical Review Letters, vol. 123, p. 210 601, 2019.

[133] S. Sachdev, Quantum Phase Transitions. Cambridge University Press, 2011.

[134] A. Altland and B. D. Simons, Condensed matter field theory. Cambridge university press, 2010.

[135] Y. Li, X. Chen, and M. P. A. Fisher, "Quantum Zeno effect and the many-body entanglement transition," Physical Review B, vol. 98, p. 205 136, 2018.

[136] B. Skinner, J. Ruhman, and A. Nahum, "Measurement-induced phase transitions in the dynamics of entanglement," Physical Review X, vol. 9, p. 031 009, 2019.

[137] A. Chan, R. M. Nandkishore, M. Pretko, and G. Smith, "Unitary-projective entanglement dynamics," Physical Review B, vol. 99, p. 224 307, 2019.

[138] Y. Li, X. Chen, and M. P. A. Fisher, "Measurement-driven entanglement transition in hybrid quantum circuits," Physical Review B, vol. 100, p. 134 306, 2019.

[139] P. W. Claeys and A. Lamacraft, "Ergodic and nonergodic dual-unitary quantum circuits with arbitrary local Hilbert space dimension," Physical Review Letters, vol. 126, p. 100 603, 2021.

[140] S. Gopalakrishnan, M. Müller, V. Khemani, M. Knap, E. Demler, and D. A. Huse, "Low-frequency conductivity in many-body localized systems," Physical Review B, vol. 92, p. 104 202, 2015.

[141] M. Serbyn and J. E. Moore, "Spectral statistics across the many-body localization transition," Physical Review B, vol. 93, p. 041 424, 2016.

[142] P. J. D. Crowley and A. Chandran, "A constructive theory of the numerically accessible many-body localized to thermal crossover," arXiv:2012.14393, 2021.

[143] S. J. Garratt, S. Roy, and J. T. Chalker, "Local resonances and parametric level dynamics in the many-body localised phase," arXiv:2107.12387, 2021.

[144] W. De Roeck and F. Huveneers, "Stability and instability towards delocalization in many-body localization systems," Physical Review B, vol. 95, p. 155 129, 2017.

[145] K. Agarwal, E. Altman, E. Demler, S. Gopalakrishnan, D. A. Huse, and M. Knap, "Rare-region effects and dynamics near the many-body localization transition," Annalen Der Physik, vol. 529, p. 1 600 326, 2017.

[146] T. Engl, J. Dujardin, A. Argüelles, P. Schlagheck, K. Richter, and J. D. Urbina, "Coherent backscattering in Fock space: A signature of quantum many-body interference in interacting bosonic systems," Physical Review Letters, vol. 112, p. 140 403, 2014.

[147] R. Dubertrand and S. Müller, "Spectral statistics of chaotic many-body systems," New Journal of Physics, vol. 18, p. 033 009, 2016.

[148] P. Hayden, S. Nezami, X.-L. Qi, N. Thomas, M. Walter, and Z. Yang, "Holographic duality from random tensor networks," Journal of High Energy Physics, vol. 2016, 2016.

[149] M. Sieber and K. Richter, "Correlations between periodic orbits and their role in spectral statistics," Physica Scripta, vol. T90, p. 128, 2001.

[150] J. Rammensee, J. D. Urbina, and K. Richter, "Many-body quantum interference and the saturation of out-of-time-order correlators," Physical Review Letters, vol. 121, p. 124 101, 2018.

[151] P. Schlagheck, D. Ullmo, J. D. Urbina, K. Richter, and S. Tomsovic, "Enhancement of many-body quantum interference in chaotic bosonic systems: The role of symmetry and dynamics," Physical Review Letters, vol. 123, 2019.

[152] D. Roy and T. Prosen, "Random matrix spectral form factor in kicked interacting fermionic chains," Physical Review E, vol. 102, p. 060 202, 2020.

[153] F. Mezzadri, "How to generate random matrices from the classical compact groups," Notices of the American Mathematical Society, vol. 54, p. 592, 2007.